

A thesis for the Degree of Ph.D. in Engineering

**Study of Reduced Rutile TiO₂ (110) Surfaces
based on the Density Functional Theory**

September 2015

Graduate School of Science and Technology
Keio University

Taizo Shibuya

©2015
Taizo Shibuya
All Rights Reserved

To my parents, Hiroyuki and Kumiko

Acknowledgment

Since the acknowledgement is the part that everybody who knows me will read, let me write this in a way which I think is interesting. It is a story in which a bad student who somehow enters a Ph.D. course, thanks to people he meets in that period, gradually changes his mind and finally builds up the confidence to be a scientist. “Science is cool, but it’s too tough for me”. This thought had always been in my mind until very recently.

My six-year Ph.D. journey started out of very impure motives. It was in the middle of my master’s course when I realized that I wanted to experience life in a foreign country. It was in 2008, when I found that Keio University provided an exchange program which I could exploit. Of course, there was a selection process for that program. During my preparation, I remember that one professor strongly disagreed with my idea. My idea read: I want to go and live abroad, so please give me an opportunity and money. “The exchange program is not for a person like you.”, he said. He was very right. So I had to make up a reason. For me that was DFT. “Since I did experiments in materials science in my master’s course, as my next step I would like to study theory”. Perfect. I passed the selection and was accepted by the Uppsala University, which had a big group in DFT. However, I had another issue to resolve, which was my affiliation with Keio University. Since I was supposed to finish my master’s course before the start of the exchange program, I had basically two choices, either to postpone my graduation or to start a Ph.D. course, the latter being apparently better. At that time, Professor Yasuoka kindly accepted me as a Ph.D. student in his group while knowing everything. So, here I would like to express my deepest gratitude to my supervisor, Professor Kenji Yasuoka. From then on, his continuous academical and financial support took me to this point. I cannot forget that, in this year finally he said ”Shibuya-kun, you should be a scientist”. I was so glad.

I also would like to thank my Swedish supervisors, Professor Susanne Mirbt and

Professor Biplab Sanyal, and people in Uppsala. At the time when I visited their group, I naively made a request to the head of Physics and Astronomy something like following: “I would like to do research. Please give me a topic on which a beginner like me can write a paper easily”. Fortunately or unfortunately, Susanne and Biplab were selected as good and patient teachers for this dodgy student. They guided me through the DFT calculations and greatly helped me with writing papers. Susanne was a surface expert and suggested I study the surface magnetism of reduced TiO₂. This was the start of my relationship with TiO₂. It was horrible because the topic was “hard-core” physics, at which I was not good, at all. It took almost three years for me to find an area, to which I can believe that I can make some contribution, and to publish our first paper. As I look back, at this moment I had already shifted to chemistry from physics. Perhaps in 2012, Susanne suggested I compare my results with STM, that was the start of our third TiO₂ paper. Throughout my academic work, I was always helped by Biplab’s optimistic comments.

I would also like to thank Professor Aron Walsh and people in his group at the University of Bath. Professor Walsh invited me to Bath several times, and in total I spent more than two months there. I loved being there. Through my interaction with them starting in 2013, I realized that DFT is not only for hard-core physicists but also for chemists. I thought this is the way I can, and indeed should, take.

I would also like to thank people at the NEC Corporation, Smart Energy Research Center. In what was almost the last period in this Ph.D. course, I did a three-month internship there, and crazily, I asked for a three-month extension because it was so much fun! There I tried to work as an independent and reliable researcher, and to some extent, I was successful. Particularly, Dr. Takashi Manako’s comments always encouraged me. After this experience, I finally obtained the confidence to be a scientist.

Members of Yasuoka lab and Matoba lab always helped me, but particularly Dr. Kazuaki Takahashi cannot be omitted from this acknowledgement. As a friend and a scientist, he patiently answered my basic and stupid questions. He always took my questions seriously as if they were valueable. That helped me a lot. Really a lot. If he hadn’t stopped me, I would have given up to complete the Ph.D. course.

I also wish to sincerely thank the members of my examining committee: Professor Hiroshi Kondo, Professor Jun Yamauchi, Professor Keita Ando, Professor Koji Fukagata for lending their time, interest and insight. And please let me thank Mr.

Koichiro Ohmori and Dr. Motoyasu Konoshita for greatly broadening my view of science, and Mr. Hajime Matsumoto for teaching me Linux and making me think about how to live. Last but not least, I would like to thank my parents, Hiroyuki and Kumiko, for giving a lot of their time to help me to grow up and supporting me until now.

Abstract

TiO₂ has many attractive applications such as solar water-splitting, gas sensors or dye-sensitized solar cells. Behind those functions is an electron transfer to/from molecules at the surface. Thus, it is essential to know the electronic structure of the model surface in order to systematically improve the efficiency of these applications. To date, the most studied surface is reduced rutile TiO₂ (110). Its reactivity is usually described by the so-called “oxygen-vacancy model”. In this model the surface states are associated with excess electrons introduced by surface bridging oxygen vacancies (V_O), and they are assumed to exist near V_O at the first layer. However, recently doubt has been cast on the validity of this model due to seemingly inconsistent reports of O₂ chemisorption. Although scanning tunneling microscopy (STM) can solve this problem by directly imaging those states, a unified interpretation of STM images is missing due to complexities in density functional theory (DFT) calculations for this system.

In this study it is shown that both hybrid DFT and DFT+ U give identical results if the same initial structures in surface relaxations and sufficiently big calculation cells are used. In the stable structure, an excess electron introduced by V_O localizes at the second layer Ti below the five-fold coordinated Ti (Ti_{5c-2nd}), forming Ti^{3+} . One Ti^{3+} has an extension along the (001) direction, effectively occupying three Ti_{5c-2nd} sites. Through a total energy analysis, Ti^{3+} ions are shown to be stable near the V_O rather than far from it. It is also shown when Ti_{5c-2nd} sites are effectively fully occupied shallow donor states are formed. Based on these results, STM images reported in other works can be interpreted consistently. Particularly, from the difference between a 5 K image and two 78 K images, it is concluded that at least above 78 K the contribution from Ti interstitials is non-negligible. Finally, it is shown that this view can explain the seemingly contradictory O₂ chemisorption experiments. This suggests that the oxygen-vacancy model needs to be modified at least above this temperature.

Contents

Acknowledgement		ii
Abstract		iii
Chapter 1	Introduction	1
Chapter 2	Theory	11
2.1	Density functional theory	12
2.1.1	The Kohn-Sham equations	13
2.1.2	The local density approximation	14
2.1.3	Generalized Gradient Approximation (GGA)	15
2.1.4	DFT+ U	15
2.1.5	Hybrid functionals	15
2.2	Treating periodic structures	16
2.2.1	Matrix expression for the Kohn-Sham equations	17
2.3	Pseudopotentials	19
2.4	Hellmann-Feynman forces	19
2.5	Surface slab calculation	20
Chapter 3	A systematic comparison between DFT+ U and HSE06	25
3.1	Introduction	25
3.2	Computational methods	27
3.3	Results and Discussion	30
3.3.1	Ideal surface reconstruction	30
3.3.2	Oxygen vacancy formation	31
3.3.3	Polaron formation	33
3.3.4	Polaron site	36
3.4	Summary	40

Chapter 4	Bipolaron formation near and far from the oxygen vacancy	41
4.1	Introduction	41
4.2	Methods	44
4.3	Results	46
4.3.1	Formation energy	46
4.3.2	Analysis of interactions	47
4.3.3	The stability of a negatively charged V_O	51
4.4	Summary	54
Chapter 5	Comparison with the filled state STM	55
5.1	Introduction	55
5.2	Computational details	57
5.3	Results and discussion	58
5.3.1	Ti^{3+} defects at Ti_{5c-2nd}	58
5.3.2	A typical STM image at 78 K	59
5.3.3	Formation of shallow donor states	63
5.3.4	78 K image under high-reduced condition	65
5.3.5	5 K image	68
5.3.6	Temperature dependency of V_O reactivity behind exper- imental complications	69
5.4	Summary	71
Chapter 6	Conclusion	72
References		75

List of Figures

1.1	Titanium dioxide powder. [1]	2
1.2	Crystal structure of rutile TiO_2 and its (110) surface. Red circle: oxygen, blue circle: titanium.	3
2.1	Flow-chart describing a self-consistent iterative process.	18
2.2	Schematic illustration of the pseudopotential V^{PP} , all-electron potential V^{AE} , and corresponding wavefunctions ψ^{PP} and ψ^{AE}	20
2.3	4-layer p(4×2) slab used in the calculation.	22
2.4	Work function dependence on the vacuum thickness. For 2-sided, 9-layer p(2×1) slab was used. For pseudo hydrogen, 6-layer p(2×1) slab was used. The exchange correlation functional was described within PW91.	23
2.5	Work function dependence on the slab thickness for pseudo hydrogen 4-layer p(4×2) slab.	23
2.6	Formation energy dependence on the slab thickness for pseudo hydrogen 4-layer p(4×2) slab.	24
3.1	Charge density of the lowest unoccupied state of a defect free TiO_2 (110) surface. Red circle: oxygen, blue circle: titanium.	29
3.2	Charge density of the energetically lowest polaron state of a oxygen vacancy containing TiO_2 (110) surface. Isosurface level = 0.015 $e/\text{\AA}^3$. Red circle: oxygen, blue circle: titanium.	32
3.3	Density of states of the oxygen vacancy. Solid (Red dashed) line is for HSE06 (PBE+ U) results. The conduction band edges in these two methods have been aligned.	34

3.4	Charge density of the polaron state. Isosurface level is $0.0013 \text{ e}/\text{\AA}^3$. (top panel) side-view along $[001]$ direction. Left (right) panel HSE06 (PBE+ U). (bottom panel) side-view along $[1\bar{1}0]$ direction. Left (right) panel HSE06 (PBE+ U). Readers are referred to Figure 3.2 to identify the location of oxygen vacancy.	35
3.5	Polaron charge density difference: HSE06-PBE+ U . White indicates 'negative' and green indicates 'positive'. Isosurface level is $0.0013 \text{ e}/\text{\AA}^3$. Readers are referred to Figure 3.2 to identify the location of oxygen vacancy.	38
3.6	Charge density of the polaron state for three different polaron geometries as described in the text. Isosurface level is $0.015 \text{ e}/\text{\AA}^3$	39
4.1	The calculated surface (left) and its schematic representation (right). Dark circle (red): O, light circle (blue): Ti. The charge density of the energetically lowest polaronic state is shown for the isosurface level = $0.005 \text{ e}/\text{\AA}^3$ (Yellow). The figure on the right depicts the picture of an oxygen vacancy and a bipolaron consisting of localized electrons and associated lattice distortions.	44
4.2	Schematic images of calculated 10 configurations. (a) neutral V_O surface with two polarons; (b) +2 charged V_O surface with a geometry taken from (a); (c) +1 charged V_O surface with one polaron; (d) +2 charged V_O surface with a geometry taken from (c); (e) +2 charged V_O surface with no polaron; (f) -2 charged ideal surface with two polarons; (g) neutral ideal surface with a geometry taken from (f); (h) -1 charged ideal surface with one polaron; (i) neutral ideal surface with a geometry taken from (h); (j) neutral ideal surface with no polaron.	45
4.3	Formation energies of the oxygen vacancy (denoted as V_O) and the ideal surface (denoted as Ideal) for different charge states as a function of the electron chemical potential for O-rich (left) and Ti rich (right) conditions. The formation energies are shown with respect to the one for the neutral ideal surface. The electron chemical potential at the valence band edge is set to be zero.	46

- 4.4 Top-view of neutral V_O surface. Here, only 2nd layer is shown. Stable position of polarons and its symmetrically equivalent position are indicated by solid black circle. Two of them are already occupied by polaronic states (yellow). Isosurface level = $0.01 e/\text{\AA}^3$. The dotted black circle shows the location of V_O 52
- 4.5 The conceptual image of a formation of three-polaron under V_O . (i) Three polarons are infinitely far away from V_O . (ii) One polaron is under V_O , two are infinitely far away. (iii) Two polarons are under V_O , one is infinitely far away. (iv) Three polarons are under V_O . For a definition of the schematic images, see Figure 4.1 and Figure 4.2. 53
- 5.1 Charge density and corresponding filled state STM 58
- 5.2 Filled state STM images of reduced TiO_2 (110). (a) Image reported by Minato *et al.* [2] Arrows indicate a position of Ti_{5c} species. (b) This work. In the calculation, band gap states appeared at about 1 eV below CB-edge in the density of states (Figure 5.3(a)) are imaged, and a tip-sample distance is about 3 \AA . Red sphere: Ti, blue sphere: O. Visualisations were made using VESTA. [3] (a) Reprinted with permission from ref 2. Copyright 2009, AIP Publishing LLC. 60
- 5.3 Electronic structure of -2 charged V_O in a 4-layer $p(6\times 2)$ surface. (a) density of states and (b) charge density of band gap states. (c) Side-view of a one Ti_{5c} row and (d) top-view of 2nd-layer of the charge density. Only the gap states about 1 eV below CB-edge are imaged. Fermi level is aligned at conduction band edge. Red sphere: Ti, blue sphere: O. Isosurface level = $0.0014 e/\text{\AA}^3$ 61
- 5.4 Charge density of the Ti^{3+} at Ti_{5c-2nd} sites in a 4-layer $p(4\times 2)$ surface with a neutral V_O . (a) whole view and (b) top-view of the 2nd-layer. Numbers denote localization sites of Ti^{3+} studied. Site dependence of relative total energies is found in Table 5.2. Isosurface level = $0.0014 e/\text{\AA}^3$ 63
- 5.5 One extra electron added to a defect-free 5-layer $p(3\times 2)$ surface. (a) Charge density of the extra electron localized at Ti_{5c-2nd} and (b) in delocalize form. (c) Self-consistent total energies of various configurations which are interpolated between localized (left) and delocalized (right) configuration. Isosurface level = $0.005 e/\text{\AA}^3$ 66

-
- 5.6 Three extra electron added to a defect-free 5-layer $p(3\times 2)$ surface.
(a) Charge density of the extra electrons localized at $\text{Ti}_{5\text{c-2nd}}$ and $\text{Ti}_{5\text{c-4th}}$ sites. (b) Charge density of extra electrons, two of them being localized at $\text{Ti}_{5\text{c-2nd}}$ sites and one in delocalized form. (c) Self-consistent total energies of various configurations which are interpolated between localized (left) and delocalized (right) configuration. (d) Density of states of the localized (top-panel) and delocalized (bottom-panel) configuration. Isosurface level = $0.005 \text{ e}/\text{\AA}^3$ 67
- 5.7 Electronic structure of a 4-layer $p(6\times 2)$ surface with a neutral V_O .
(a) Filled state STM image and (b) corresponding charge density of band gap states about 1 eV below CB-edge. (c) Density of states. A tip-sample distance is about 3 \AA . Isosurface level = $0.0014 \text{ e}/\text{\AA}^3$. 69

List of Tables

3.1	Ionic displacement in [\AA] within the relaxed surface relative to the ideal cleavage surface.	30
3.2	Polaron energy in (eV) for different polaron sites.	38
3.3	Energetics of magnetic structures in (eV).	40
4.1	Polaron-polaron interaction and its lattice contribution. Figure 4.2 is referred to denote the configurations in the table. The specific subsystems used to define each configuration exactly corresponds to the subfigures in Figure 4.2.	47
4.2	V_O -polaron interaction and its lattice contribution. The configurations are denoted by same convention as in Table 4.1.	48
4.3	V_O -two polaron interaction. Same convention as in Table 4.1 has been used to describe the configurations.	49
4.4	Lattice distortion contribution to V_O -two polaron interaction. Same convention as in Table 4.1 has been used to describe the configurations.	51
5.1	Ti^{3+} positions in neutral V_O $p(4 \times 2)$ 4-layer cell and its total energy.	58
5.2	Ti^{3+} positions in Ti_{5c-2nd} in neutral V_O $p(4 \times 2)$ 4-layer cell and its total energy. Another Ti^{3+} is localized at position 2 in another Ti_{5c} row	62

Chapter 1

Introduction

The white powder shown in Figure 1.1 is called titania, titanium dioxide or TiO_2 . It is used as white pigments or sunscreens in our daily life. At the same time, it draws much attention as new energy-related or electronic device materials, which are behind the general motivation of this thesis. After the big success of solid state physics and quantum chemistry represented by the invention of semiconductor transistors and solar cells in the 1950s, metal oxides including TiO_2 started to be seen as a frontier of semiconductors. As a consequence, interesting phenomena such as photo-catalytic water splitting, [4] dye-sensitized photovoltaics and recently memristive effects [5] were found in TiO_2 . Although a lot of effort was invested to understand the mechanisms of these effects in order to improve them, the applications of these effects are currently not in full-scale use. One limiting factor of these efforts lies in the previous applications of solid state physics and quantum chemistry. Since they are built upon the understanding of the bulk properties of materials, the surface effects are not incorporated in a rigorous manner. This is natural because there had been no way to access atomic-scale surface properties until the invention of the scanning tunneling microscope (STM) in the 1980s [6] and the establishment of its interpretation by Density Functional Theory (DFT) calculations in the 1990s. A combination of STM and DFT is now recognized as a standard tool for the study of surface electronic structures of metals and simple semiconductors. In contrast, however, the study of metal oxide surfaces is still in its early stages. Even the capability of DFT and STM for describing surface defects is not clear for rutile TiO_2 (110) (Figure 1.2), the model surface of metal oxides. In this thesis, the electronic properties of reduced rutile TiO_2 (110) surfaces are studied by DFT, demonstrating the power of DFT and STM for describing those defects. More explicitly, in this work, the so-called oxygen-vacancy model estab-



Figure 1.1 Titanium dioxide powder. [1]

lished in the 1970s by then state-of-art techniques such as cluster calculations and photoelectron spectroscopies is revisited using new generation tools such as DFT and STM. It is a small but necessary piece in establishing the theory of metal oxide surfaces. Through this process of theory construction, we can find many promising applications such as solar water splitting, efficient solar cells or better electronic devices. This is exactly what had occurred during the construction of solid state physics and quantum chemistry.

Hereafter, the topic of the thesis is introduced by briefly reviewing the philosophy and history behind solid state physics and quantum chemistry which are the basis of this study and of surface science itself. It is of great help to understand the possible outcomes and the goal of surface science as well as the importance of calculations and where this thesis is located in that context.

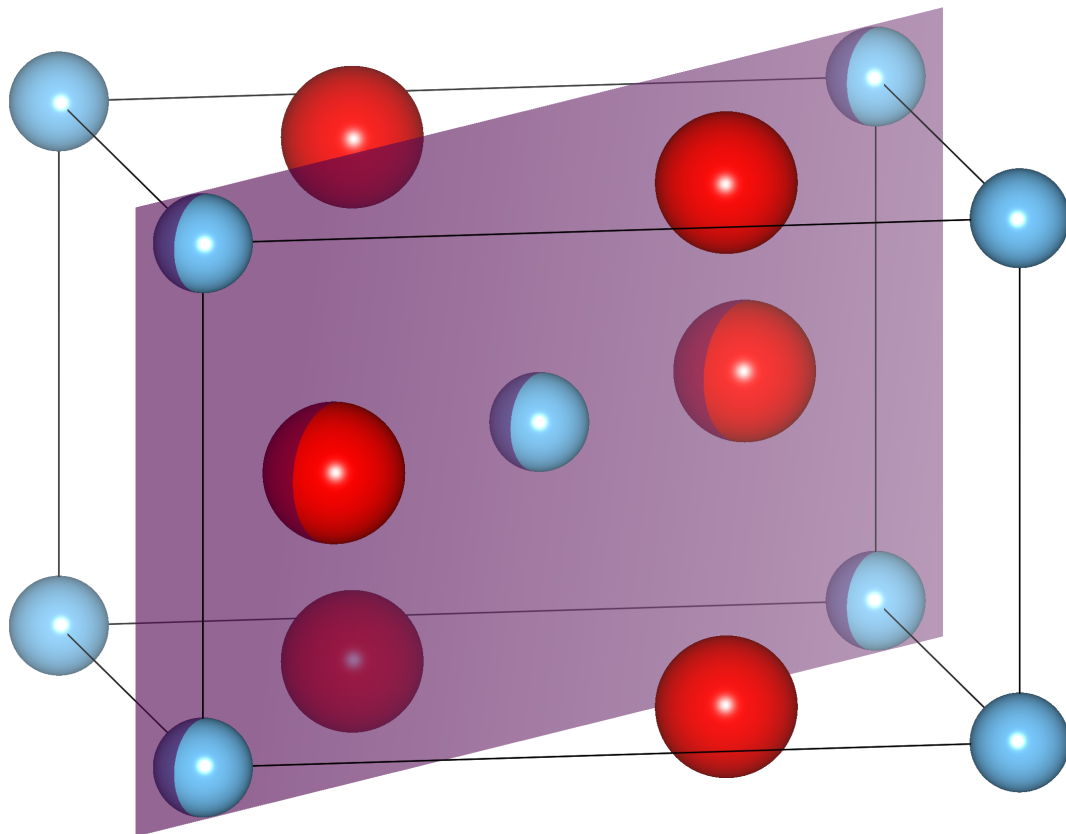


Figure 1.2 Crystal structure of rutile TiO₂ and its (110) surface. Red circle: oxygen, blue circle: titanium.

Assumptions behind materials science

Surface science, solid state physics and quantum chemistry are all reductionistic approaches to the properties of matter based on the Schrödinger equation, and share the following properties.

- Matter consist of atoms, for example 1 g of carbon has about 10^{23} C atoms
- There are only about 100 atom types in the world, as describe in the periodic table
- An atom consists of a nucleus and electrons
- A nucleus has a positive charge and an electron has a negative charge
- Electrons, especially valence electrons, which are loosely bound by a nucleus, play an important role in chemical reaction
- Electrons obey an equation which is called the Schrödinger equation

- Electrons can not be distinguished, which means that electrons follow a Fermi-Dirac distribution

It should be emphasized that none of this is obvious. Rather, it is hard to believe from our daily experiences. The reason why I believe these statements is because the approaches based upon them are very successful in describing many things about the microscopic structures of matter, and more importantly, greatly affect our life. Computers, smartphones, solar cells or fuel cells are all products of semiconductor physics and quantum chemistry. Nobody can even touch or see electrons, but we believe in them and would like to solve the Schrödinger equation to understand and improve materials properties.

To solve Schrödinger equation: approximations and numerical calculations

Since the Schrödinger equation does not have an analytical solution for a system with more than two electrons, there are three ways to solve it. The first option is to solve it numerically, the second one is to approximate the equation until it can be solved analytically, and the third one is a hybrid and popular approach, to approximate the equation until it can be solved using calculators or computers. The first option became possible only recently due to advances in parallel computing, using what is known as quantum Monte-Carlo calculations. In this case, an integration of a many-variable complex function (called the many-body wavefunction) is evaluated by the Monte-Carlo method. The results are used to check the validity of other calculation methods such as DFT. The main route of modern materials science is to take the third way. This is where the calculation comes into play in this field on top of theory and experiments. Thus the calculation resources and the way of approximating the equation are the limiting factors of this field. The advances in these areas have invoked a shift, for example, from solid state physics/chemistry to surface science. To make things more complicated, the solution of the many-body Schrödinger equation (many-body wavefunction) depends on the positions of all electrons in the system. This is very non-intuitive and difficult to interpret. In this respect, the approximation works also as a model on which one can think about what is going on in matter instead of just looking at the many-body wavefunction.

1920s-1950s: Schrödinger equation and the success of semiconductor physics

An intensive interplay between theory and experiments on the microscopic structure of matter in the early 20th century, following a reductionistic approach to nature, initiated by the success of Newton's equation of motion, catalyzed into the Fermi-Dirac distribution and Schrödinger equation in 1926. Although it was originally applied to the Hydrogen atom, a one-electron system, to explain its emission spectrum, the application to many-electron systems was of immediate interest to scientists. This was at a time when there were only mechanical calculators, so the numerical approach was very hard, and so the system should be sufficiently simple. A many-electron atom was chosen as the first target for solving the many-body Schrödinger equation numerically. This successful approximation was known as Hartree-Fock equation [7]. The solutions can be interpreted as many non-interacting electrons in a mean-field, which effectively includes many-body interactions. They are also known as "atomic orbitals" labeled by characters such as *s*, *p* and *d*. The Hartree-Fock approximation explained the shell structure of atoms in detail and the periodic table could then be more clearly understood. Since then, the view of "atomic orbitals" remains a firm basis of both solid state physics and quantum chemistry.

Other than this, scientists tried to approximate the equation and solve it analytically. It is hard to define the boundaries, but roughly speaking, physicists were interested in metals and alloys, while chemists wanted to explain chemical reactions using the Schrödinger equation. Physicists constructed what is called "band theory" while they attempted to explain transport properties such as electric conductivity and thermal conductivity or heat capacities of metals and alloys. Chemists developed valence band theory or the Hückel method to extend and modify their semi-classical notions, such as the octet rule.

During World War II, semiconductor rectifiers were intensively researched to make radar detectors. Metal-semiconductor junctions used in crystal radios or semiconductor-semiconductor junctions, which were later identified as p-n junctions, were studied. As a result, the mechanism behind them became clearly understood in the framework of band theory. Impurities in the semiconductor crystal turned out to play an important role in transport properties. These studies finally led to

the invention of semiconductor transistors, solar cells and LEDs in the 1950s, marking the remarkable success of band theory. This is one of the best examples to show that something very useful can be found from a theory construction in which a non-realistic “model” is created and compared both experimentally and theoretically. In this case, during the extension of band theory, pure silicon crystal, with a small amount of impurities, was prepared and transport properties or contact potential differences were compared using the band model of semiconductors. This surface is one of the “model” studies in surface science.

1960s-1980s: Metal oxides as a frontier and the failure of semiconductor physics

The appearance of computers made a big shift in materials science in which the many-body Schrödinger equation can be numerically solved for a realistic system. However, the weak computational power at the time required a good approximation for the equation. Of particular interest was how to incorporate electron-electron interactions into the approximation. This was the problem for physicists. The popular approach was to utilize the electron density such as Slater’s X-alpha method, but the most successful one was DFT. Proposed by Hohenberg and Kohn in 1964, [8] and completed by Kohn-Sham’s approach to exchange correlation interactions, [9] DFT was so successful in describing the properties of many body electrons in materials, such as lattice constants or bulk modulus of metals and simple semiconductors. Chemists developed what is called molecular orbital theory, with the help of group theory to reduce the number of solutions. Later chemists incorporated DFT into their theories and succeeded in predicting the formation enthalpy of several chemical reactions. This quantitative success finally resulted in the award of the Nobel Prize for Chemistry to Walter Kohn in 1998. Now DFT is accepted by the chemistry community as a standard tool.

Differences between physicists and chemists also can be seen in the treatment of electrons. In band theory, electrons are treated as plane waves with fully-periodic structures whereas they are treated as localized waves or particles with non-periodic structures in chemists’ framework.

After the invention of semiconductor-based devices, the unexplored area of metal oxides, such as TiO_2 , was explored. Interesting phenomena such as photocatalytic reactions, dye-sensitized photovoltaics are found in TiO_2 . Those phenomena were

understood using band theory as well as molecular orbital theory, and attempts such as chemical doping were made to improve those effects based on these theories. However, the improvement was not so straight-forward and the application of them is very limited, even today. Band theory and molecular orbital theory are based on fully-periodic and non-periodic structures, respectively. What is missing is a theory for partially-periodic structures, or specifically surfaces. However, at the time, there was no way to directly observe surfaces and test such theories.

Experimental techniques for electronic structure measurements also experienced significant advancements. X-ray photoelectron spectroscopy (XPS), Ultraviolet photoelectron spectroscopy (UPS) or Electron energy loss spectroscopy (EELS) appeared in this period. The results were compared with empirical molecular orbital calculations and interpreted. Reduced rutile TiO_2 was intensively studied using those techniques. These approaches were catalyzed into the so-called “oxygen-vacancy model”. [10] In this model, the surface states were associated with bridging oxygen vacancies, and they were assumed to be at the first layer. This model was in accord with the previous view of ionic crystals. This means that an oxygen atom, an electronegative element, become O^{2-} . For example, TiO_2 consists of Ti^{4+} and O^{2-} and Ti_2O_3 consists of Ti^{3+} and O^{2-} . The interesting finding was that when TiO_2 is slightly reduced, which is noted as TiO_{2-x} , it has a signature of Ti^{3+} . Since TiO_2 is usually slightly reduced and a Ti^{3+} has an extra electron compared with Ti^{4+} , it was thought that Ti^{3+} was the key to understand the properties of this oxide. At the time, however, the signature of Ti^{3+} in TiO_{2-x} could not be reproduced by calculation, and thus progress came to a halt.

1980s-1990s: The dawn of surface science and problems in metal oxide surfaces

STM was invented in 1981, and marked the dawn of modern surface science. Through a tunneling current between a tip and a material surface, it enabled the observation of atomic-scale electronic structures. Since STM only gives a two-dimensional black and white contrast, interpretation by calculation is required to obtain an electron distribution in real space. Fortunately, the interpretation by calculations had been established for metals and simple semiconductors by the 1990s. However, DFT still could not describe reduced TiO_2 properly.

In this period, although DFT was successful, both physicists and chemists recog-

nized that further improvement of the description of electron-electron interactions in DFT was required in order to expand the area of application. What was lacking was the exchange interaction, which the Hartree-Fock approximation provided perfectly. Chemists incorporated the Hartree-Fock approach into DFT and developed what is called the hybrid functional DFT. Physicists also included the exchange interaction to explain metal oxides. The method is known as DFT+ U .

1990s-early 2000s: TiO₂ as a model surface of metal oxides

TiO₂ has three major crystal structures known as rutile, anatase and brookite. Out of these, rutile is known to be thermodynamically the most stable and (110) is the most stable surface. As briefly described above, in order to exploit the functionality of metal oxides, it is recognized that the theory of materials science should be expanded so that surfaces are rigorously understood from the Schrödinger equation. In order to expand the understanding of the surface of metal oxides, rutile TiO₂ (110) has been studied as a model surface. In this period, the interpretation of empty state STM images was established. [11] In contrast, there were only a few attempts to understand filled state images [12,13] in which filled state images were interpreted, for example, by small cluster calculations based on molecular orbital theory. However, in terms of both experimental resolutions and accuracies in calculation, realistic studies had not started until the late 2000s. Also, Henderson reported the existence of Ti interstitials in the surface of reduced TiO₂. [14]

Late 2000s-present: defects behind the surface reactivity of reduced rutile TiO₂

In the late 2000s, scientists began to doubt the validity of the oxygen-vacancy model, to some extent. [15–18] At the same time, DFT+ U was applied to reduced metal oxides such as V₂O₅, MoO₃ or CeO₂ and successfully described the localized electron due to reduction. [19–21] More importantly, in 2006 Di Valentin *et al.* applied the hybrid functional to reduced rutile TiO₂ (110) and the signature of Ti³⁺ in electronic structure observed in UPS and EELS was reproduced. [22] Later, Morgan and Watson applied DFT+ U and confirmed that the localized Ti³⁺ was correctly described. [23]

After these advancements, studies of filled state STM became active, because it

is a promising tool for resolving those questions. Since the reduced surface usually has Fermi energy at the conduction band edge (CB-edge), [10] which is a basis of STM interpretation, [11] a negative bias of about -1 V images only the gap states and shallow donor states. In the literature, there are several atomic-scale images which were taken at either 78 K or 5 K, [2, 24, 25] with bias voltages varying from -2 to -1 V. Importantly, there is no agreement in the interpretations, even now. While Minato *et al.* reported that V_O -induced Ti 3d states are delocalized on the first layer, [2] Papageorgiou *et al.* concluded that they are delocalized from the first to third layer, and only a -2 charged V_O can reproduce the STM image. [24] Very recently, Setvin *et al.* interpreted their image as a weighted average of Ti 3d states localized at the first and second layer. [25] These discrepancies arose because of the nature of the gap states and the effect of having Fermi energy at the CB-edge were not properly taken into account.

Meanwhile, as a consequence of further research within DFT in 2010s, the nature of the band gap states is becoming more and more clear. The gap states are formed by introducing donor defects such as V_O and bridging hydroxyl (OH_b), or adding extra electrons to a defect-free surface. [22, 26, 27] On top of that, a Ti interstitial is reported to introduce four excess electrons in the system. [28, 29] An excess electron localizes at a Ti site occupying a Ti 3d-like orbital. Surrounding Ti-O bonds are consequently expanded which results in a formation of a polaronic Ti^{3+} . However, if it comes to the stable position of a polaron, there was no solution, which was an obstacle for the coherent understanding of the filled state images. Since the symmetry is broken at the surface, Ti sites are no longer equivalent. The polaron can be stabilized at almost any Ti site in the surface by controlling the initial structure of relaxation. In 2011, Deskins *et al.* and Chretien *et al.* conducted a systematic study in which the position of Ti^{3+} was controlled and the stability was studied using DFT+ U . [27, 30] Both of them suggested that Ti^{3+} is stable in the second layer. This contradicts the classical belief that it is located at the nearest neighbor Ti site of oxygen vacancy, as well as the previous calculations.

Also the shallow donor states, which are delocalized among Ti sites placing the Fermi energy at the CB-edge, are not well studied even though they are the basis of the STM interpretation. This is because electrons added to this system prefer to be localized in hybrid DFT or DFT+ U . Very recently, through bulk supercell calculations, Janotti *et al.* reported that the delocalized state is close in energy to

the localized state, and the coexistence of those states is possible due to an energy barrier between them. [31] However, there is currently no such study for the surface.

Objectives and the thesis outline

In order to check the validity of the oxygen-vacancy model by interpreting filled state STM images consistently, the following questions are investigated in this thesis using DFT:

- What is the stable position of the polaronic Ti^{3+} ?
- What is the stable configuration of polarons around V_{O} , especially under Fermi energy at the CB-edge?
- Under what conditions are shallow donor states formed?

In Chapter 2, theory as well as computational methodologies are introduced. In Chapter 3, it is shown that both of hybrid DFT and DFT+ U give identical results if the same initial structures in surface relaxations and sufficiently big calculation cells are given. It is also shown that Ti^{3+} is the most stable at the second layer Ti site below the five-fold coordinated Ti site ($\text{Ti}_{5\text{c-2nd}}$). It is also shown that Ti^{3+} at the $\text{Ti}_{5\text{c-2nd}}$ site covers three $\text{Ti}_{5\text{c-2nd}}$ sites, with only about 70% of an electron being at the center. In Chapter 4, Ti^{3+} is shown to be stable near the V_{O} rather than far from it, using a total energy analysis. In Chapter 5, it is shown that under Fermi energy at the CB-edge, $\text{Ti}_{5\text{c-2nd}}$ sites are effectively fully occupied regardless of V_{O} coverage, up to 16.7%. It is suggested that the shallow donor states are located deeper within the structure, not affecting the gap states image significantly. The coexistence of shallow donor states and localized states are possible when $\text{Ti}_{5\text{c-2nd}}$ sites are effectively fully occupied. Then, based on the refined view, it is demonstrated that the filled state STM images in the literature can be consistently interpreted. A key feature is a bright blob in the $\text{Ti}_{5\text{c}}$ row which is interpreted as a Ti^{3+} at the $\text{Ti}_{5\text{c-2nd}}$ site. Images taken at 78 K are interpreted as having effectively fully occupied $\text{Ti}_{5\text{c-2nd}}$ sites by Ti^{3+} , while the 5 K image is interpreted by partially occupied $\text{Ti}_{5\text{c-2nd}}$ sites. The difference is explained by an ionization of Ti interstitials, which suggests that the so-called oxygen-vacancy model needs to be modified at temperatures above at least 78 K. Finally in Chapter 6, conclusions and future perspectives are discussed.

Chapter 2

Theory

As far as the materials' electronic properties such as chemical reactivities are concerned, a guiding equation is the many-body Schrödinger equation. In particular, since only the steady state properties are dealt in this thesis, time-independent Schrödinger equation is a starting point:

$$\hat{H}\Psi_{tot}(\mathbf{r}_1, \mathbf{r}_2, \dots, \mathbf{R}_1, \mathbf{R}_2, \dots) = E\Psi_{tot} \quad (2.1)$$

where Ψ is the many-body wavefunction, \mathbf{r}_i and \mathbf{R}_i are the positions of the electrons and ions, respectively, and \hat{H} is the Hamiltonian for the system. An explicit form of the Hamiltonian can be guessed through a process called "canonical quantization" as following.

$$\begin{aligned} \hat{H} = & - \sum_i \frac{\hbar^2}{2m_e} \nabla_{\mathbf{r}_i}^2 - \sum_{i,j} \frac{e^2 Z_j}{4\pi\epsilon_0 |\mathbf{r}_i - \mathbf{R}_j|} + \frac{1}{2} \sum_{i \neq j} \frac{e^2}{4\pi\epsilon_0 |\mathbf{r}_i - \mathbf{r}_j|} \\ & + \frac{1}{2} \sum_{i \neq j} \frac{Z_i Z_j e^2}{4\pi\epsilon_0 |\mathbf{R}_i - \mathbf{R}_j|} - \sum_i \frac{\hbar^2}{2M_i} \nabla_{\mathbf{R}_i}^2, \end{aligned} \quad (2.2)$$

where M_i and Z_i are the nucleus mass and charge, respectively, m_e is the electron mass, \hbar is Planck's constant divided by 2π and e is the electron charge. Due to its complexity, the many-body Schrödinger equation can be solved exactly for small and simple system.

In order to make problem tractable, we first apply so-called the Born-Oppenheimer approximation which separates the motion of the ions and the electrons. This is justified by the fact that the mass of a nucleus is much bigger than the mass of an electron. As a consequence of this approximation, the many-body wavefunction is rewritten as a product of the electron wavefunction and the nuclear wavefunction

$$\Psi_{tot}(\mathbf{r}_1, \dots, \mathbf{R}_1, \dots) = \Psi_e(\mathbf{r}_1, \dots; \mathbf{R}_1, \dots) \cdot \Psi_{nuc}(\mathbf{R}_1, \dots). \quad (2.3)$$

The semicolon in the electron wavefunction indicates that it depends on the ionic positions as parameters but not as variables. By setting a small term such as the kinetic energy of the ions to zero, which is valid at $T = 0$ K, the many-body Schrödinger equation can be separated into two equations. The first is the Schrödinger equation for the nuclei and the second is for the electrons for a given ionic configuration. Since we focus on the electronic properties, the latter is of the interest:

$$\mathbf{H}_e \Psi_e(\mathbf{r}_1, \dots; \mathbf{R}_1, \dots) = E_e \Psi_e(\mathbf{r}_1, \dots; \mathbf{R}_1, \dots), \quad (2.4)$$

where \mathbf{H}_e consists of the first three terms of \mathbf{H} in Eq. (2.2):

$$\hat{H}_e = - \sum_i \frac{\hbar^2}{2m_e} \nabla_{\mathbf{r}_i}^2 - \sum_{i,j} \frac{e^2 Z_j}{4\pi\epsilon_0 |\mathbf{r}_i - \mathbf{R}_j|} + \frac{1}{2} \sum_{i \neq j} \frac{e^2}{4\pi\epsilon_0 |\mathbf{r}_i - \mathbf{r}_j|} \quad (2.5)$$

In the earliest days of quantum physics in 1930s, D. R. Hartree made attempts to solve this problem under the assumption that the many-body wavefunction is a product of one electron orbitals,

$$\Psi_e(\mathbf{r}_1, \mathbf{r}_2, \dots, \mathbf{r}_n) = \psi(\mathbf{r}_1)\psi(\mathbf{r}_2) \cdots \psi(\mathbf{r}_n). \quad (2.6)$$

This approach violates the Pauli's exclusion principle since the many-body wavefunction is not antisymmetric. It was improved by expressing the many-body wavefunction as a determinant of one-electron orbitals, which is known as the Slater determinant. This approach is called the Hartree-Fock approximation. In this formalism, the fact that electrons are fermions is incorporated. In other words, the exchange effects are taken into account. The Hartree-Fock approximation does not give an exact total energy for the system because it uses averaged potentials based only on one determinant, which in some cases is not a good approximation to the true all electron wavefunction. The energy difference between the Hartree-Fock energy and the true ground state energy is called the correlation energy.

2.1 Density functional theory

In density functional theory (DFT), the electron density play a central role instead of the many-body wavefunction. Following two theorems formulated by Hohenberg and Kohn in 1964 are the foundation of DFT.

Theorem 1. *For the particles interacting under an external potential, the potential can be uniquely determined by the ground state electron density $n(\mathbf{r})$.*

This theorem guarantees that the ground state electron density alone can determine the external potential thus all ground state properties of the system. Then the problem is how to find this density. The second theorem helps solve this problem:

Theorem 2. *For any external potentials, it is possible to define the energy $E[n]$ as an universal functional of the electron density. The exact ground state energy of the system is the global minimum of this functional for any external potentials, and electron density $n(\mathbf{r})$ which minimizes the functional is an exact ground state electron density.*

This means that an electron density of interest can be found by using variational principle if the exact expression for the energy functional is known. However, at this point an exact expression of energy functional to which the variational principle can be applied is not given.

2.1.1 The Kohn-Sham equations

Kohn and Sham casted a problem of n interacting electrons into a non-interacting n -electron under an effective potential. In this system, electron density is described as following:

$$n(\mathbf{r}) = 2 \sum_{i=1}^{n/2} |\psi_i(\mathbf{r})|^2, \quad (2.7)$$

where $\psi_i(\mathbf{r})$ is a non-interacting one electron orbital. By using this one electron orbital, energy functional of the system can be constructed as following:

$$\begin{aligned} E[n(\mathbf{r})] &= E_{ke}[n(\mathbf{r})] + E_{eff}[n(\mathbf{r})] + E_{II} \\ &= E_{ke}[n(\mathbf{r})] + E_{ext}[n(\mathbf{r})] + E_H[n(\mathbf{r})] + E_{XC}[n(\mathbf{r})] + E_{II} \\ &= 2 \sum_i \int \psi_i \left(-\frac{\nabla^2}{2}\right) \psi_i d\mathbf{r} + \int V_{ext}(\mathbf{r}) n(\mathbf{r}) d\mathbf{r} \\ &\quad + \frac{1}{2} \iint \frac{n(\mathbf{r}) n(\mathbf{r}')}{|\mathbf{r} - \mathbf{r}'|} d\mathbf{r} d\mathbf{r}' + E_{XC}[n(\mathbf{r})] + E_{II}, \end{aligned} \quad (2.8)$$

where the first term in the last equation is the kinetic energy of electrons, the second is the Coulomb interaction energy between the nuclei and the electrons, The third and fourth terms stem from the Coulomb interaction energy between electrons, called the Hartree and Exchange-Correlation (XC) term, respectively. The exact form of the XC term is discussed in the next section. Fifth term is the Coulomb interaction energy between ions.

Then, by applying the variational principle to this functional under the condition that the sum of the density throughout the system should be constant and equal to the number of electrons, a Schrödinger-like one particle equation, which is known as the Kohn-Sham equation, is derived:

$$\hat{\mathcal{H}}\psi_i = \left[-\frac{1}{2}\nabla^2 + V_{eff}(\mathbf{r})\right]\psi_i = \varepsilon_i\psi_i, \quad (2.9)$$

where $\hat{\mathcal{H}}$ is the one electron Hamiltonian and $V_{eff}(\mathbf{r})$ the effective potential in which the electron interacts. The effective potential can be written as a combination of potential terms that originate from the energy functional:

$$V_{eff}(\mathbf{r}) = V_{ext} + V_H + V_{XC} = V_{ext}(\mathbf{r}) + \int \frac{n(\mathbf{r}')}{|\mathbf{r} - \mathbf{r}'|} d\mathbf{r}' + \frac{\delta E_{XC}[n(\mathbf{r})]}{\delta n(\mathbf{r})} \quad (2.10)$$

The problem is now reduced to find non-interacting one-electron orbitals in the effective potential.

2.1.2 The local density approximation

In the Kohn-Sham formalism, important information of the interacting n -electron is kept in the exchange-correlation energy $E_{XC}[n(\mathbf{r})]$. In order to solve the Kohn-Sham equation, an explicit form of the exchange-correlation energy as a functional of electron density should be given by approximating the electron-electron interaction. The local density approximation (LDA) is one of the most popular approximations which was originally proposed by Kohn and Sham. In this approximation, the exchange-correlation energy is set to be equal to the exchange-correlation energy in a homogeneous electron gas of the same electron density:

$$E_{XC}^{LDA}(n) = \int n(\mathbf{r})\varepsilon_{XC}[n(\mathbf{r})]d\mathbf{r}, \quad (2.11)$$

where ε_{XC} is the exchange-correlation energy of one electron at position \mathbf{r} in a homogeneous electron gas. The exact value of ε_{XC} can be calculated from solving the many-body Schrödinger equation explicitly by, for example, Quantum Monte Carlo methods.

Since LDA is based on the assumption that the electron density is locally almost constant, it can be generalized to a spin-polarized system by explicitly dealing with the electron density of two different spin. This approach is called the *local spin density approximation* (LSDA) and defined as following.

$$E_{XC}^{LSDA}(n^\uparrow, n^\downarrow) = \int n(\mathbf{r})\varepsilon_{XC}[n^\uparrow(\mathbf{r}), n^\downarrow(\mathbf{r})]d\mathbf{r}, \quad (2.12)$$

where $n(\mathbf{r}) = n^\uparrow(\mathbf{r}) + n^\downarrow(\mathbf{r})$.

2.1.3 Generalized Gradient Approximation (GGA)

Electrons in real materials is not distributed homogeneously. In order to incorporate those non-local effects into XC energy, the first step is to use the local gradient in the electron density. This approach is called the generalised gradient approximation (GGA) and can be written in the following way:

$$E_{XC}^{GGA}[n^\uparrow, n^\downarrow] = \int n(\mathbf{r}) \varepsilon_{XC}[n^\uparrow(\mathbf{r}), n^\downarrow(\mathbf{r}), |\nabla n^\uparrow(\mathbf{r})|, |\nabla n^\downarrow(\mathbf{r})|, \dots] d\mathbf{r}. \quad (2.13)$$

There are many ways to implement the gradients of the electron density in a GGA functional. The Perdew-Wang functional (PW91) [32] and the Perdew-Burke-Ernzerhof functional (PBE) [33] are two of the most widely used functionals for solids.

2.1.4 DFT+ U

The LDA/GGA tend to over-delocalize electrons due to their intrinsic self-interaction error, and in some cases wrongly predicts a semiconductor as a metal. DFT+ U is a way to overcome this problem by using an orbital-dependent potential that adds an extra Coulomb interaction U . The electrons are separated into localized and delocalized electrons. While the Coulomb repulsion U is taken into account for the localized electrons via a Hubbard-like term in a model Hamiltonian, the delocalized electrons are described by a standard orbital-independent LDA/GGA formalism. The XC energy in this approach has the following form:

$$E_{XC}^{DFT+U}[n^\uparrow, n^\downarrow] = E_{XC}^{LDA/GGA}[n^\uparrow, n^\downarrow] + E_{Hub} - E_{dc}, \quad (2.14)$$

where $E_{LDA/GGA}[n^\uparrow, n^\downarrow]$ is the standard LDA/GGA total energy, E_{Hub} is the Hubbard-like term and E_{dc} is the double counting term.

2.1.5 Hybrid functionals

Another way to correct the errors of LDA/GGA is known as hybrid functionals. By incorporating a fraction of Hartree-Fock (HF) exact exchange into the LDA/GGA exchange, hybrid functionals often better-describe band gaps of semiconductors. In this thesis, one of the most common hybrid functionals HSE (Heyd-Scuseria-Ernzerhof) [34, 35] is used. HSE is based upon PBE functional, but the exchange

term is split into two components, a long-range and a short-range terms. Then a portion of HF exact exchange is applied to the short-range term:

$$E_{XC}^{HSE} = 0.25E_X^{HF,SR} + 0.75E_X^{PBE,SR} + E_X^{PBE,LR} + E_C^{PBE}, \quad (2.15)$$

where E_{XC}^{HSE} is the HSE exchange-correlation energy, $E_X^{HF,SR}$ is the short range term of the Hartree-Fock exchange part, $E_X^{PBE,SR}$ and $E_X^{PBE,LR}$ are short and long range terms of the PBE exchange part and E_C is the correlation part of PBE. For the screening parameter which determine the range of $E_X^{HF,SR}$, it was set to 0.2 \AA^{-1} , following the recommendation of the original paper. [35] With this value, the band gaps of semiconductors are best described.

2.2 Treating periodic structures

Solids consist of more than 10^{23} ions. One way to approximate this fact is to express a solid as an infinitely and periodically repeated unit cell. The effective potential V_{eff} in this system should be written as following:

$$V_{eff}(\mathbf{r} + \mathbf{R}) = V_{eff}(\mathbf{r}), \quad (2.16)$$

where \mathbf{R} is the real lattice vector defined by $\mathbf{R} = n_1\mathbf{a}_1 + n_2\mathbf{a}_2 + n_3\mathbf{a}_3$ (n_i : integer number, \mathbf{a}_i : unit cell vectors). According to the Bloch's theorem, the one-electron wavefunction under the periodic potential can be written as:

$$\psi_{\mathbf{k}}^j(\mathbf{r}) = u_{\mathbf{k}}^j(\mathbf{r}) \cdot e^{i\mathbf{k}\cdot\mathbf{r}}, \quad (2.17)$$

where $u_{\mathbf{k}}^j(\mathbf{r})$ has the periodicity of the lattice $u_{\mathbf{k}}^j(\mathbf{r} + \mathbf{R}) = u_{\mathbf{k}}^j(\mathbf{r})$. The wavefunction is labeled by a discrete value called band index j and a vector \mathbf{k} , and has a following property:

$$\psi_{\mathbf{k}}^j(\mathbf{r}) = \psi_{\mathbf{k}+\mathbf{K}}^j(\mathbf{r}), \quad (2.18)$$

where \mathbf{K} is defined by $\mathbf{K} = n_1\mathbf{b}_1 + n_2\mathbf{b}_2 + n_3\mathbf{b}_3$ (n_i : integer number, \mathbf{b}_i : reciprocal lattice vector satisfying $\mathbf{a}_i \cdot \mathbf{b}_j = 2\pi\delta_{ij}$), and \mathbf{k} is kept in the first Brillouin zone, which is the primitive cell of the reciprocal lattice. In this formalism, one can pose a boundary condition for the wavefunction arbitrarily, which is known as the Born-von Karman boundary condition:

$$\psi_{\mathbf{k}}^j(\mathbf{r} + N_i\mathbf{a}_i) = \psi_{\mathbf{k}}^j(\mathbf{r}), \quad i = 1, 2, 3, \quad (2.19)$$

where N_i is an arbitrary integer and equals to the number of \mathbf{k} in the first Brillouin zone. For example, when N_i is set to infinite, \mathbf{k} becomes continuous value. The

bigger it is, the more accurate the wavefunctions become. However, in an actual calculation, one has to take a finite value. It is because that the physical quantities such as the total energy per the unit cell is obtained through the average value of all states (wavefunctions) in the first Brillouin zone. One has to set N_i to finite value in order to keep the problem tractable under a finite computational resource. This procedure is called k-point sampling.

$u_{\mathbf{k}}^j(\mathbf{r})$ can be expanded by plane waves by exploiting its periodicity:

$$u_{\mathbf{k}}^j(\mathbf{r}) = \sum_{\mathbf{G}} c_{\mathbf{k},\mathbf{G}}^j e^{i\mathbf{G}\cdot\mathbf{r}}, \quad (2.20)$$

where \mathbf{G} are the reciprocal lattice vectors. Thus, the wavefunction can be expressed based on plane waves:

$$\psi_{\mathbf{k}}^j(\mathbf{r}) = \sum_{\mathbf{G}} c_{\mathbf{k},\mathbf{G}}^j e^{i(\mathbf{k}+\mathbf{G})\cdot\mathbf{r}}. \quad (2.21)$$

Although infinite number of plane waves are needed to expand an arbitrary function, in the case of our interest the number is limited since the terms, $c_{\mathbf{k},\mathbf{G}}^j$, with sufficiently high kinetic energy $\frac{\hbar^2}{2m}|\mathbf{k} + \mathbf{G}|^2$ have the negligible contribution to the total energy. This is done by truncating the sum in Eq. (2.21) at some kinetic energy, which is called the cut-off energy.

The cut-off energy and the number of k-points determine the accuracy of a discretization of the problem. Although the bigger the better, they should be adjusted according to the computational resource.

2.2.1 Matrix expression for the Kohn-Sham equations

Under the framework of the plane-wave expansion, the Kohn-Sham equations can be rewritten as a matrix eigenvalue equation at each k-point:

$$\sum_{\mathbf{G}'} \left(\frac{\hbar^2}{2m_e} |\mathbf{k} + \mathbf{G}'|^2 \delta_{\mathbf{G}\mathbf{G}'} + V_{eff}(\mathbf{G} - \mathbf{G}') \right) c_{\mathbf{k}+\mathbf{G}'}^j = \varepsilon_{\mathbf{k}}^j c_{\mathbf{k}+\mathbf{G}}^j, \quad (2.22)$$

where $V_{eff}(\mathbf{G} - \mathbf{G}')$ is given by:

$$V_{eff}(\mathbf{G} - \mathbf{G}') = \int V_{eff}(\mathbf{r}) e^{-i(\mathbf{G}-\mathbf{G}')\cdot\mathbf{r}} d\mathbf{r}. \quad (2.23)$$

Now the problem of solving a differential equation was transformed into solving a set of eigenvalue equations. Since the matrix depends on its eigenvalues, the equation should be solved by a self-consistent iterative process. First, initial V_{ext}

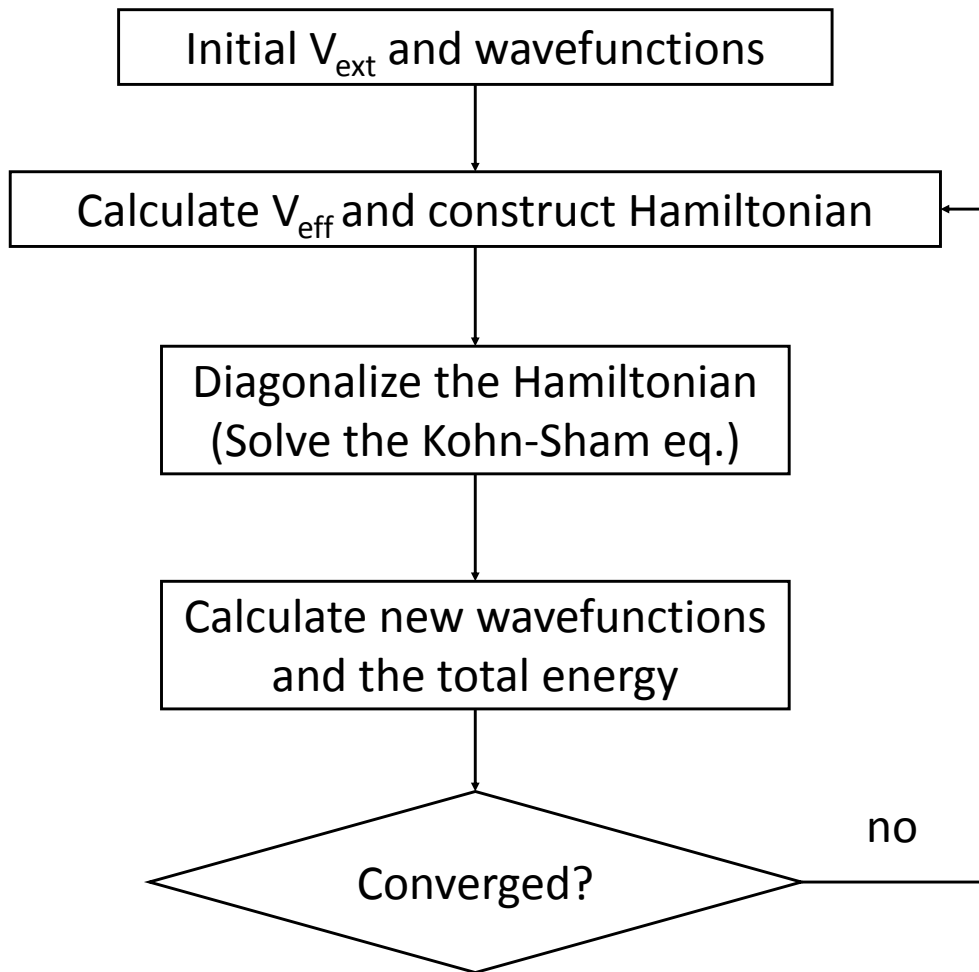


Figure 2.1 Flow-chart describing a self-consistent iterative process.

and wavefunctions are set. Then the V_H and V_{XC} are calculated from the initial electron density. After this $V_{\text{eff}} = V_{\text{ext}} + V_H + V_{XC}$ is calculated, thus the matrix is constructed. By diagonalizing this matrix for all k-vectors, one can obtain the new set of eigenvectors. Out of this eigenvectors, new wavefunctions are obtained and consequently new matrix can be constructed for the next iterative step. At this point, the total energy of the system is compared with previous value. Until the energy converges within a certain range, the iterative process continues. The process is shown in Figure 2.1.

2.3 Pseudopotentials

There is a way to reduce the number of electrons and the cut-off energy to be calculated in materials. In this approach, core and valence electrons are treated differently. When atoms get together to form a solid, the core electrons are bound to their atomic nucleus and remain unchanged. In contrast the valence electrons are actively involved in the chemical bonding, and should have different character from the atomic state. Since our interest is in describing the chemical reactivity, it is natural to approximate that the core s are frozen and dealt as a part of atomic nucleus. This approach is called as the pseudopotential approximation in which the atomic potential is replaced by a pseudopotential which includes the core electrons. The basic properties of the pseudopotential V^{PP} and the corresponding pseudo-wavefunction ψ^{PP} are compared with the all-electron (AE) potential and wavefunction in Figure 2.2.

The pseudopotential and pseudo-wavefunctions are set to be identical to the all-electron wavefunctions ψ^{AE} outside a certain radius r_c of the atom. Compared with ψ^{AE} which has many nodes in core region, ψ^{PP} is *softened* which means that the number of plane waves to expand the wavefunction is reduced. It is because the atomic-orbital-like core states, to which the valence wavefunctions should be orthogonalized, do not exist in the *pseudized* system. This method not only decreases the number of electrons in the system, but also the number of plane waves is greatly reduced.

Various pseudopotentials had been developed so far and Projector augmented wave (PAW) potential, which is used in this thesis, is one of the outcomes. Being first proposed by Blöchl [36] and implemented in plane wave calculations by Kresse and Joubert [37], PAW can calculate all-electron properties at a cost of pseudo potentials.

2.4 Hellmann-Feynman forces

Hellmann-Feynman theorem provides an efficient way to calculate forces on an atoms. The force on an atom can be written as the derivative of the total energy

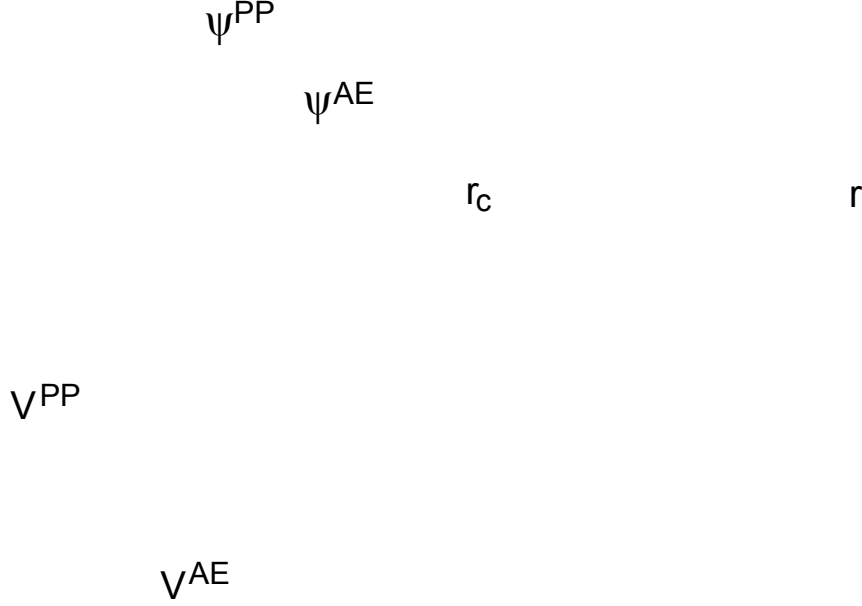


Figure 2.2 Schematic illustration of the pseudopotential V^{PP} , all-electron potential V^{AE} , and corresponding wavefunctions ψ^{PP} and ψ^{AE} .

with respect to atomic position \mathbf{R}_I :

$$F_I = -\frac{dE}{d\mathbf{R}_I} = -\sum_i \langle \psi_i | \frac{\partial \hat{H}}{\partial \mathbf{R}_I} | \psi_i \rangle = -\frac{\partial E_{II}}{\partial \mathbf{R}_I} - \int n(\mathbf{r}) \frac{\partial V_{ext}(\mathbf{r})}{\partial \mathbf{R}_I} d\mathbf{r}. \quad (2.24)$$

By minimizing these forces, an equilibrium structure can be obtained.

2.5 Surface slab calculation

Throughout this thesis, the surface is modeled by a three-dimensional periodic structure divided by a vacuum layer. This is a standard way to describe a surface within plane wave DFT calculations and called a surface slab model. The basic assumption of this model is that with a finite thickness of a vacuum layer and slab, one can extract the properties of a surface. Since each side of the slab faces vacuum, there are two ways to deal with them. One is called 2-sided in which both of the

ends are treated as a surface and in the ions in the middle of the slab are fixed at bulk positions. In the other way, which is named as “pseudo hydrogen” in this thesis, one side of the slab is treated as bulk region, ions in the bottom layer being kept at bulk positions. Electrons at that side should be stabilized so that they do not have spurious effects on the model. To do that pseudo-hydrogens, which have nucleus and electrons with non-integer charge, are placed to saturate cut bonds. The advantage of this method is that one can reduce the number of ions roughly by half compared with the 2-sided model. To reduce the computational demand posed by using HSE06 functional, pseudo hydrogen is adopted in this thesis and the surface is mainly modeled by a 4-layer slab with a 10 Å of vacuum layer as shown in Figure 2.3. The charge of pseudo hydrogens are determined as 2/3 and 4/3 for O and Ti site, respectively, following the earlier work. [38] The work function difference between 2-sided and pseudo hydrogen is compared in Figure 2.4. It can be seen that with a sufficient thickness of vacuum and slab, both model behave similarly. To check the accuracy of the model used in terms of the slab thickness, the work function and formation energy are plotted in Figure 2.5 and 2.6, respectively. They oscillate within the range of a few tens of meV. Considering that the energy of room temperature is about 25 meV, it is not completely converged. Rather, the use of this 4-layer slab with a 10 Å vacuum is required by the use of HSE06 and justified by the fact that it well-reproduce the surface reconstruction pattern as discussed in the next chapter.

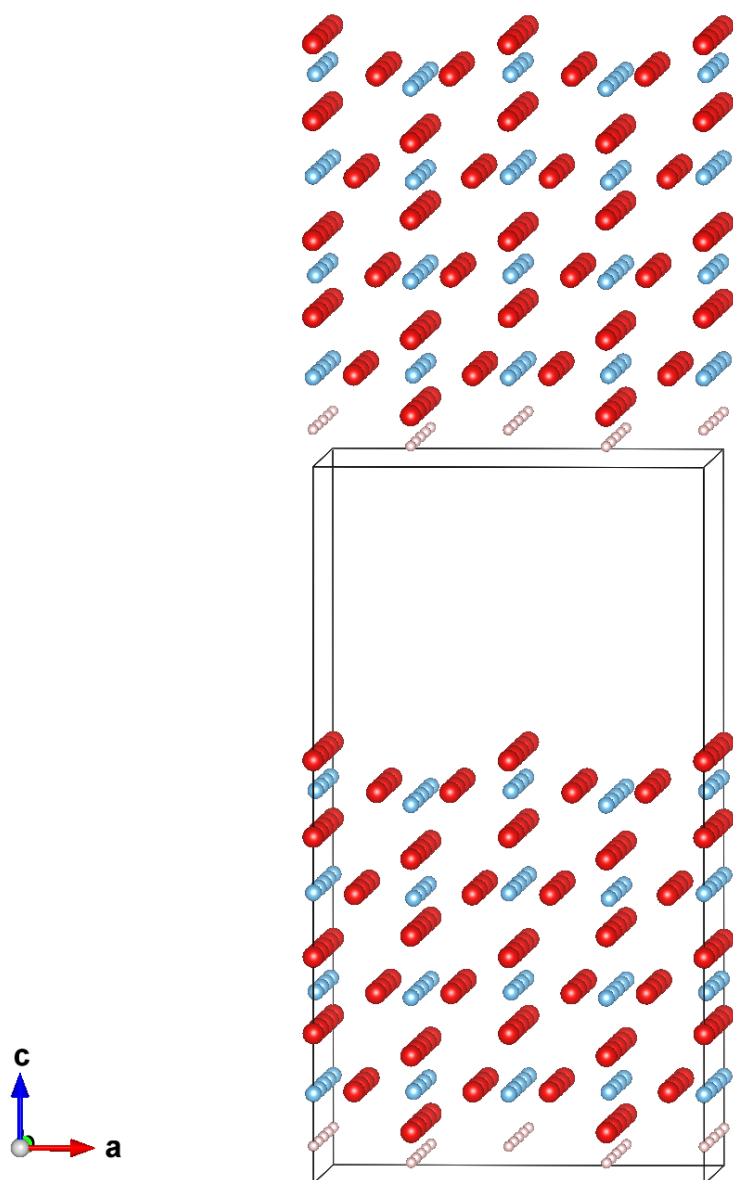


Figure 2.3 4-layer p(4x2) slab used in the calculation.

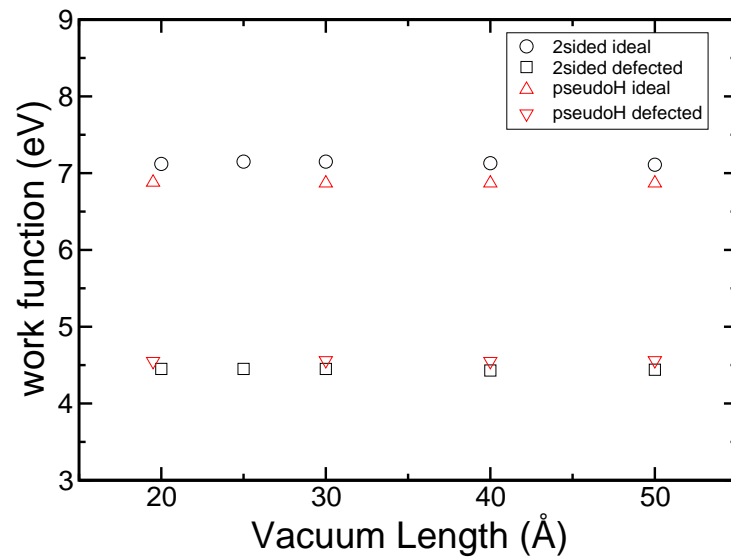


Figure 2.4 Work function dependence on the vacuum thickness. For 2-sided, 9-layer $p(2\times 1)$ slab was used. For pseudo hydrogen, 6-layer $p(2\times 1)$ slab was used. The exchange correlation functional was described within PW91.

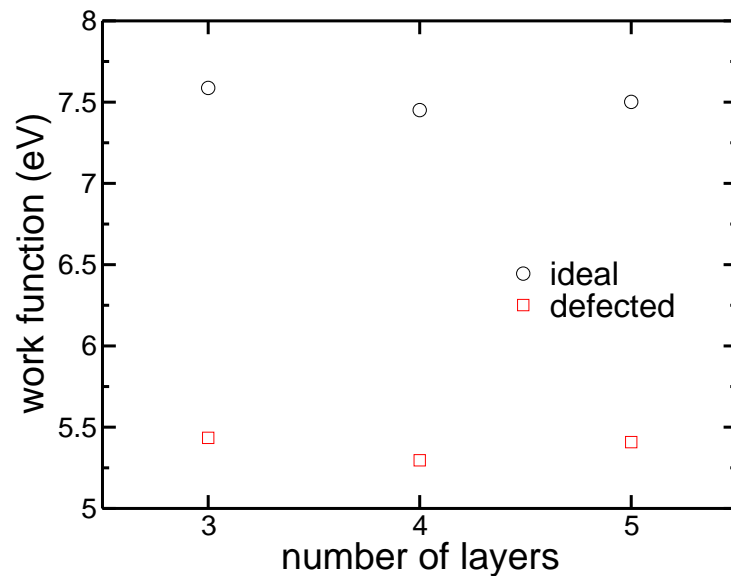


Figure 2.5 Work function dependence on the slab thickness for pseudo hydrogen 4-layer $p(4\times 2)$ slab.

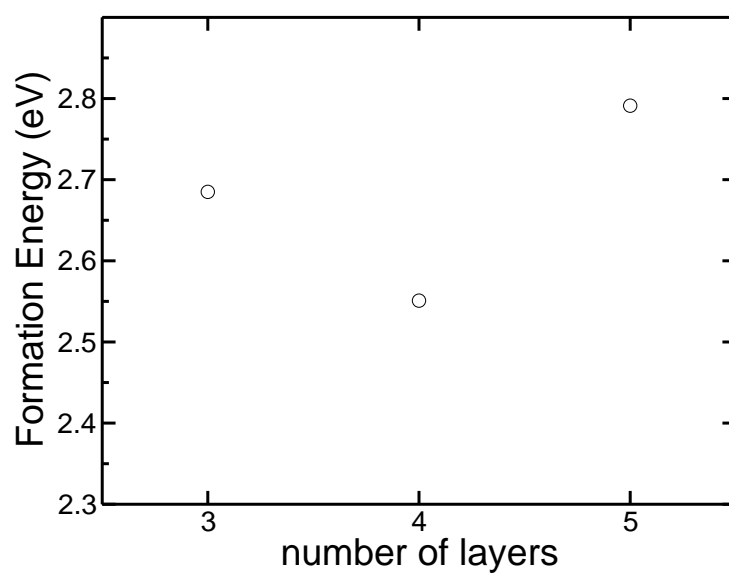


Figure 2.6 Formation energy dependence on the slab thickness for pseudo hydrogen 4-layer p(4x2) slab.

Chapter 3

A systematic comparison between DFT+U and HSE06

3.1 Introduction

TiO₂ is a functional material with widespread applications in technology [39]. Its wide band gap (3 eV) is for example, utilized in suncreening and chemical solar cells. Also it is used in photocatalytic splitting of water [40] and degradation of organic molecules in polluted air or water. TiO₂ crystallizes in three phases: anatase, rutile, and brookite. The most stable bulk phase is rutile and the most stable surface is the (110) rutile surface followed by the (101) anatase surface [41]. The geometric structure of the most stable defect free (110) rutile surface has been studied both experimentally and theoretically [42] and is generally agreed to be the (1×1) surface with bridging oxygen rows [43].

Experimentally, the broad band gap state at ~ 1 eV below the conduction band edge has been associated with the occurrence of oxygen vacancies accompanied by the presence of Ti³⁺ ions: ultraviolet photoemission spectroscopy (UPS), resonant photoemission, electron energy loss spectroscopy (EELS) and X-ray photoelectron spectroscopy (XPS) all attribute the ~ 1 eV state to Ti³⁺ ions [44]. Recently it was proposed that the band gap state at ~ 1 eV below the conduction band edge is not caused by the oxygen vacancy but by Ti interstitial defects [15], but these results are under debate [45–47].

Recent reviews of the current understanding of oxygen vacancies at the TiO₂ surface summarize both experimental [42] and theoretical results [44,48]. A substantial experimental evidence exists to show the presence of bridging oxygen vacancies on the rutile TiO₂ (110) surface. Their concentration is reported as several per cent:

8% for a surface annealed in vacuum [49], (4 ± 0.6) % [45] and ~ 15 % [50] for a surface prepared by cycles of Ar bombardment and annealing. In most experimental studies, an oxygen vacancy concentration of roughly 10 % is reported [42].

Calculations based on local density approximations (LDA) or generalized gradient approximations (GGA) to the density functional theory (DFT) are insufficient for systems with strong electron correlations. In addition, both LDA and GGA calculations are known to severely underestimate oxide band gaps due to the built-in self-interaction error. Within LDA/GGA, the band gap state corresponding to the oxygen vacancy is calculated to be at the bottom of the conduction band [44], which is in disagreement with experiment.

To overcome this problem, both GGA+ U [23, 27, 30, 51] and hybrid functional [2, 22] approaches have been conducted, where a Ti^{3+} state is reported with the presence of a gap state. This state corresponds to one localized electron, which is trapped by a local lattice distortion around a Ti ion, i.e. a polaron. But the location of the polarons varies in different calculations. Some have reported two surface polarons [22], some two equivalent polarons on subsurface sites [27, 51] and others a combination with a sub subsurface polaron and a subsurface polaron [30].

The localization of the electrons can be achieved by either employing the DFT+ U (LDA+ U /GGA+ U) method or a hybrid functional. Within the quantum chemistry community, the B3LYP hybrid functional is rather common and is used to cure the above mentioned errors of the local density approximation regarding the approximate description of the electron-electron interaction. The B3LYP consists of a weighted sum over the exact exchange according to Hartree-Fock and density functional exchange correlation, where the weights are parameters. The disadvantage is that the correlation in the limit of the homogenous electron gas is not correctly described [52] and it is often worse than HSE06 in describing ground state properties of especially inorganic solids [53]. In this work HSE06 is used as hybrid functional. It has been shown to describe the lattice and electronic properties of TiO_2 in very good agreement with experiment [54].

A computationally inexpensive way of treating the problem is by the GGA+ U method. GGA+ U consists of the GGA exchange-correlation functional plus a Hubbard U term which is weighted by the orbital and spin occupation. In addition, some part of the GGA exchange/correlation functional has to be subtracted in order to minimize the double-counting. The usage of GGA+ U on TiO_2 does not correct the

band gap: the band gap becomes 2.2 eV compared to an experimental band gap of 3 eV, but allows for the electron localization at Ti ions.

A systematic comparison between these two approaches is missing in the literature. In this chapter, a thorough comparison between DFT+ U and hybrid functional results is presented regarding the polaron formation due to the presence of oxygen vacancy on the (110) rutile TiO₂ surface. Comparing HSE06 and GGA+ U , the HSE06 functional shows overall better agreement with experimental values available for TiO₂. At the same time the HSE06 functional is computationally more expensive. By comparing HSE06 with GGA+ U one can determine if the polaron formation in TiO₂ is described sufficiently accurate by using GGA+ U . The results are analyzed in terms of local lattice distortions, charge distribution around polarons and magnetic exchange interactions between the polarons.

3.2 Computational methods

For DFT calculations, a plane wave based pseudopotential code, VASP [55, 56] was used. The exchange correlation potential was approximated within the generalized gradient approximation by the Perdew-Becke-Ernzerhof (PBE) [33] method and for some calculations with PW91 [32].

For the GGA+ U calculation, Dudarev approach was adopted following Deskins *et al.* [27] PBE and an effective value of the Coulomb parameter U ($U_{eff} = U - J = 4.2$ eV, J being intraatomic exchange parameter) were used. A value of U_{eff} was fixed since the dependence of the polaron formation on the value of U had been already investigated by Deskins *et al.* [27] They have found that the values of U_{eff} between 3.3 and 5.4 eV do not influence the relative energies among possible polaron sites, but only change the position of the polaron state within the band gap.

For the hybrid functional calculations, the screened hybrid functional of Heyd, Scuseria, and Ernzerhof (HSE06) [34, 35], where correlation is described in GGA (PBE) and the exchange is a mixture of 25% exact (HF) exchange and 75% PBE exchange, was adopted. The HSE screening parameter was set to 0.2 \AA^{-1} . The advantage of this hybrid functional is that it is numerically feasible due to its mixing of only the short-ranged interaction. Moreover the correlation is described correctly in the limit of the homogeneous electron gas. The HSE06 has successfully been tested on many materials' ground state properties including the band gap [53, 57].

Especially, the HSE06 functional has been used by Janotti *et al.* [54] for studying oxygen vacancy in bulk rutile TiO_2 , where they found the HSE06 functional to improve the agreement between the calculated ground state properties and the experimental results.

Due to the high computational cost of hybrid functionals in general, the supercell size was restricted. The surface was modeled by a $p(4 \times 2)$ geometry with a slab thickness of 4 layers separated by 10 \AA vacuum. This amounts to 128 oxygen and 64 titanium ions. The surface was modeled by a 6 layer slab with pseudo hydrogen termination and 20 \AA vacuum, a 9 layer slab with two surfaces and 20 \AA vacuum, and a 4 layer slab with 10 \AA vacuum. In terms of the qualitative description of the ideal surface reconstruction, the lattice relaxation due to the oxygen vacancy, the vacancy formation energy and the work function, the used slab models show agreement between each other.

Lattice constants of $a = 4.647 \text{ \AA}$ and $c = 2.983 \text{ \AA}$ were determined by the calculations for bulk TiO_2 . For the surface calculations, the bottom layer was fixed at bulk positions and terminated by pseudohydrogen [38] atoms. The Brillouin zone was sampled by a $2 \times 2 \times 1$ Monkhorst-Pack grid unless stated otherwise. The plane wave cut-off energy was 450 eV and the core-valence interaction was described by the Projector Augmented Wave approach (PAW).

It was found that the relaxed polaron structure strongly depends on the initial structure in agreement with earlier calculations. [23] According to need, following three schemes to localize an electron at the targeted site were adopted. The starting structure of those schemes was always the optimized surface structures by PW91. In all schemes, one O atom was removed in the beginning of the simulations. Unless otherwise stated, the calculations were performed in spin-polarized mode.

Scheme 1: First, two Ti sites were selected for an electron localization site. Then a Ti atom was substituted by a V atom and let the surface relax. After that the V site was recovered and the surface was relaxed again. This corresponds to the procedure of Deskins *et al.*.

Scheme 2: First, two Ti sites were selected and the distance to the neighboring oxygen atoms were expanded by 5 %. Then the surface was relaxed. This is according to Chretien *et al.*.

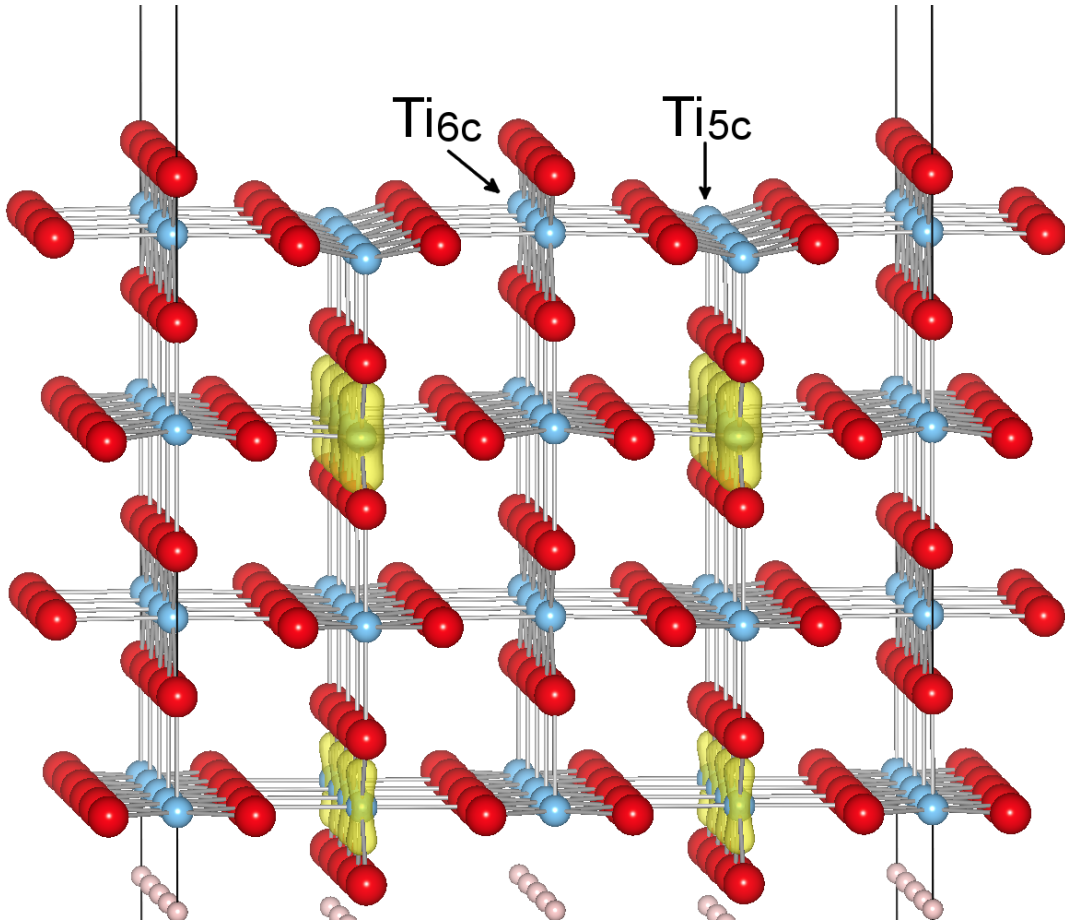


Figure 3.1 Charge density of the lowest unoccupied state of a defect free TiO_2 (110) surface. Red circle: oxygen, blue circle: titanium.

Scheme 3: First, the surface was relaxed with a restriction of non-spin polarization. Then the Scheme 2 was applied.

In order to investigate the triplet and singlet states, when needed, an extra restriction which fixed the total magnetic moment at either 0 or $2 \mu_B$ was applied. In all cases, Hellman-Feynman forces were reduced till $0.05 \text{ eV}/\text{\AA}$.

Table 3.1 Ionic displacement in [\AA] within the relaxed surface relative to the ideal cleavage surface.

	PW91 (Ref. [61])	FLAPW (Ref. [59])	PW91 (this work)	PBE+ U (this work)	HSE06 (this work)	SXRD (Ref. [62])	LEED (Ref. [63])
Ti6c	0.21	0.08	0.21	0.37	0.1	0.12 \pm 0.05	0.25 \pm 0.03
Ti5c	-0.21	-0.23	-0.18	0.03	-0.26	-0.16 \pm 0.05	-0.19 \pm 0.03
O _{bridge}	0	-0.16	0.03	0.24	-0.1	-0.27 \pm 0.08	0.10 \pm 0.05
O _{in plane}	0.14	0.09	0.16	0.36	0.05	0.05 \pm 0.05	0.27 \pm 0.08
Ti _{below Ti6c}	0.13	0.07	0.16	0.24	0.07	0.07 \pm 0.04	0.14 \pm 0.05

3.3 Results and Discussion

3.3.1 Ideal surface reconstruction

Ideal rutile TiO_2 structure has an orthorhombic D_{2h} symmetry, because not all 6 oxygen-titanium bonds are equal. [58] The (110) surface is the cleavage surface of rutile TiO_2 . The surface is charge neutral and reconstructs in a (1×1) pattern. It contains both Ti and O ions with two different coordinations: the outermost ions are two-fold coordinated oxygen ions located in a bridge position (see Figure 3.1). This oxygen row is called the bridging oxygen row. The bridging oxygen ions are located on top of six-fold coordinated Ti ions. These Ti ions form a row, further on called Ti6c row. The Ti6c ions are oriented such that the plane containing its four oxygen neighbors is perpendicular to the surface along the Ti6c row. Between two surface Ti6c rows lies a 5-fold coordinated Ti row, further on called Ti5c row. The Ti5c row is oriented such that the plane containing its four oxygen neighbors is parallel to the surface. The oxygen ($O_{in\ plane}$) in between Ti6c and Ti5c rows is three-fold coordinated.

Electron counting [59, 60] gives that every surface Ti5c ion contributes $2/3$ electrons less to its bonds than its valency. This implies that every Ti5c ion is charged with $+2/3$ electrons. At the same time the surface Ti6c ion is charged with $-2/3$ electrons. The charge transfer between Ti5c and Ti6c surface ions makes the (110) surface charge neutral. The positive charge on the surface Ti5c ion increases the ionicity of the Ti5c-O bonds due to which the surface Ti5c- $O_{in\ plane}$ bond lengths decrease by 0.6%. The opposite happens for the Ti6c- $O_{in\ plane}$ bonds: the negative charge on the surface Ti6c ions decreases the ionicity of the surface Ti6c- $O_{in\ plane}$ bonds due to which the bond lengths are increased by 2.6%.

The calculated lowest unoccupied state has a b_{2g} character (d_{xz}) for bulk TiO_2 . The lowest unoccupied state of the ideal rutile TiO_2 (110) surface is located on the Ti ions below the surface Ti5c rows (see Figure 3.1) and is a mixture of 90% d_{z^2} and 10% $d_{x^2-y^2}$ character in the global coordinate frame. The surface Ti5c states are located about 0.15 eV (0.12 eV with PBE+ U) higher up in energy. The work function was calculated to be 7.9 (6.9) eV within HSE06 (PBE).

Comparing the ideal surface reconstruction patterns, a difference between PBE+ U and HSE06 is found. Table 3.1 shows the displacement of the ions relative to the positions of the ideal cleaved surface. The buckling of the surface is reproduced independent of the exchange approximation used here. In PBE, PBE+ U and HSE06 give a buckling of 0.4 Å comparing the positions of a Ti6c and a Ti5c ion, which is in excellent agreement with experiments (see last columns in Table 3.1). But with HSE06 the overall displacement of the ions is an inward relaxation, whereas with PBE+ U it is an outward displacement. This is best reflected considering the relaxation of the bridging oxygen ion: In PBE+ U it moves 0.24 Å out of the surface, in PBE it more or less stays in the surface, whereas in HSE06 it moves into the surface. Unfortunately, the two experiments deviate in the displacement of the bridging oxygen ion: with LEED it is measured to move out of the surface whereas with SXRD it is measured to move into the surface. Overall, the LEED results agree better with the PBE+ U calculations whereas the SXRD results agree better with the HSE06 results. In summary, with HSE06 (PBE+ U) the bond between Ti6c and the bridging oxygen ion becomes stronger (weaker) in agreement with the SXRD (LEED) results. Future experiments have to clarify this issue.

3.3.2 Oxygen vacancy formation

The optimized lattice structure with an oxygen vacancy after the removal of one bridging oxygen ion at the surface is shown in Figure 3.2. In the following, the two Ti ions in the surface Ti6c row neighboring the vacancy is denoted as Ti6c*. These ions are located in the Ti6c row but have become five-fold coordinated due to the vacancy formation. An oxygen vacancy in bulk TiO_2 gives rise to an excess of two electrons because the removal of one oxygen ion leaves 3 partially filled (with 2/3 electrons each) dangling bonds on its Ti neighbors. An oxygen vacancy in the surface layer also gives rise to an excess of two electrons, because the removal of

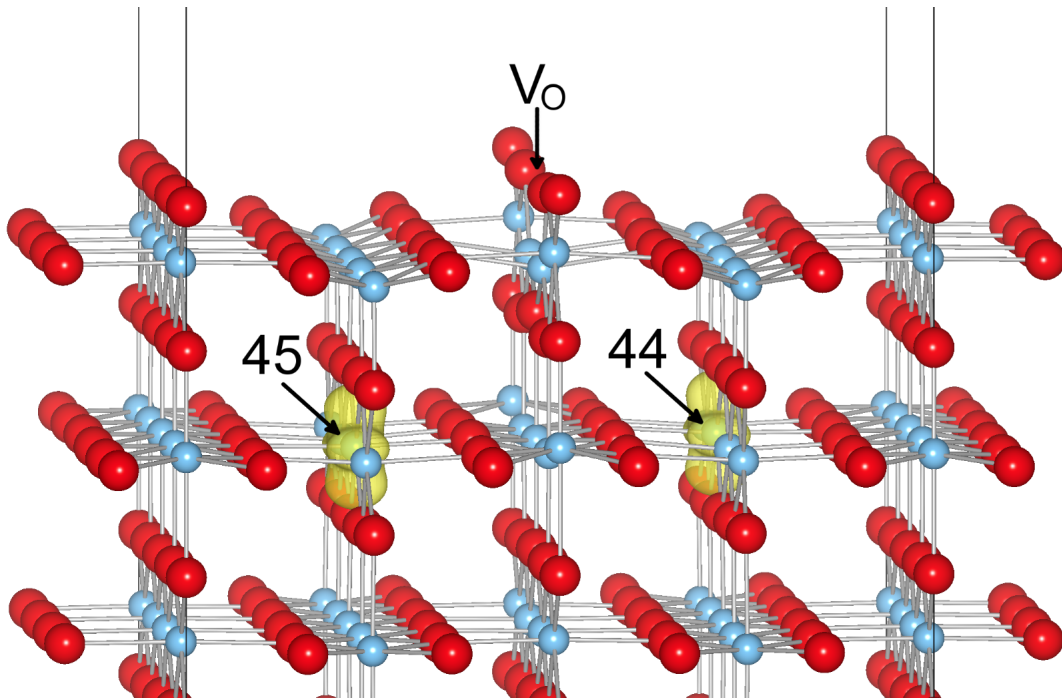


Figure 3.2 Charge density of the energetically lowest polaron state of a oxygen vacancy containing TiO_2 (110) surface. Isosurface level = $0.015 \text{ e}/\text{\AA}^3$. Red circle: oxygen, blue circle: titanium.

a twofold coordinated oxygen ion leaves two partially occupied Ti dangling bonds (with 1 electron each). Due to the missing oxygen ion, a local reconstruction of the vacancy neighbors occurs. In the following, the relaxation patterns obtained by HSE06 (PBE+ U) are provided. The oxygen ion below the two Ti6c^* ions moves up by 2.2 (1.1) % and the Ti6c^* ions move down by 2.6 (2.2) %. This gives rise to a Ti-O-Ti bond angle of 126° (116°) compared to 90° for an octahedral configuration. The bond length between Ti6c^* and the underlying oxygen ion (further on called O164) is reduced by 2.1 % compared to the bulk value whereas the bond between O164 and the underlying Ti ion (further on called Ti36) is increased by almost 22 (11) %.

Electron counting reveals that the surface can not remain semiconducting by only rearranging the electrons on the Ti-O bonds. (It would leave partially occupied dangling bonds on some Ti ions.) Instead the two excess electrons are localized on two Ti ions (see next section), which preserves the semiconducting properties of TiO_2 , because no partially occupied state arises. Since the surface is charge neutral, an excess of two electrons implies that somewhere in the surface a charge

of +2 exists. Again electron counting shows where the charge of +2 is located: One Ti ion in the Ti5c row remains holding +2/3 electrons which now is not compensated by a bridging oxygen due to the absence of one oxygen ion. The additional charge of +4/3 electrons is located on the Ti6c* ions, on each Ti6c* ion a charge of +2/3.

3.3.3 Polaron formation

TiO₂ is an ionic semiconductor. For ionic semiconductors the band gap increases with increasing degree of ionicity and vice versa. The oxygen (titanium) sites are charged with -2 electrons (+4 electrons), in short [O(-2);Ti(+4)]. The system can gain energy by localizing the excess electrons on two equivalent Ti ions: Localizing one electron on a Ti ion [O(-2);Ti(+3)] will locally lower the ionicity. This Ti ion is attracted less by its oxygen neighbors. Its bond lengths and the volume of the local octahedron centered on this Ti ion are increased. In addition, a lowering of the ionicity is equivalent to a lowering of the energy eigenstates.

In the ideal rutile lattice the two excess electrons can only populate the conduction band, because the valence band is completely occupied. The site projection of the ideal structure's lowest unoccupied state is shown in Figure 3.1. The electron localization is equivalent to a spatial symmetry breaking of this state, where this state is shared now by only two Ti ions. This electron localization accompanied by a local lattice distortion is termed a polaron.

The energetically most stable solution of the two polarons obtained by us is in agreement with earlier calculations [27, 51]. The polaron is in the subsurface layer below the Ti5c rows (see Figure 3.2). This configuration is called as 44-45 in the following discussion. Comparing Figs. 3.1 and 3.2 one clearly sees the spatial symmetry breaking. This explains why the polarons are located in the subsurface layer. The polaron state is a mixture of 84% d_{z^2} and 16% $d_{x^2-y^2}$ character within HSE06 and 80% d_{z^2} and 20% $d_{x^2-y^2}$ character within PBE+ U in the global coordinate frame.

Figure 3.3 shows the calculated density of states of the (110) surface with one oxygen vacancy. The vacancy is calculated to be accompanied by a polaron state 1.22 eV (1.50 eV with PBE+ U) below the conduction band edge. The band gap at the Γ -point is calculated to be 3.19 eV with HSE06 and 2.11 eV with PBE+ U .

Figure 3.4 shows the charge density of the polaron state. Both PBE+ U (right figure) and HSE06 (left figure) give more or less the same spatial distribution of the

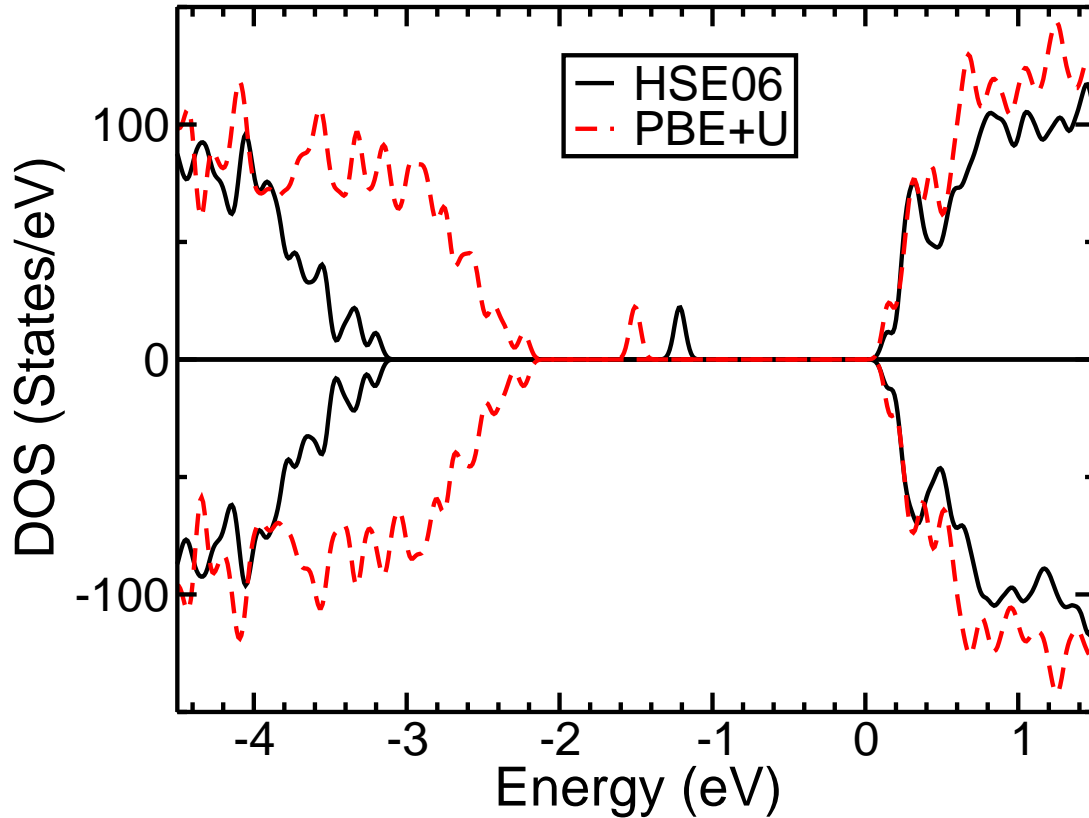


Figure 3.3 Density of states of the oxygen vacancy. Solid (Red dashed) line is for HSE06 (PBE+ U) results. The conduction band edges in these two methods have been aligned.

polarons. The polaron is 72 % located on the center Ti site and the remaining 28 % is spread out on its oxygen and mainly titanium neighbors as is shown in Figure 3.4. The polaron shape follows the symmetry of the on site d-orbital. It is thus more or less contained within the plane containing the four neighboring oxygen ions. In the direction of the Ti rows the polaron has a size of about 6 Å and in the direction perpendicular to the Ti row, it has a size of about 7 Å. This is in good agreement with recent electron transport measurements by Hendry *et al.* [64] where they fitted their results to the Feynman polaron model and obtained a polaron radius between 4 Å and 8 Å depending on their choice for the optical-phonon coupling constant.

The polaron formation gives rise to an increase in the bond length between the Ti ion and its O neighbors by ~ 0.1 Å per bond, but only for the bonds in the plane of the four oxygen ions around the polaron center ion. This anisotropy of the polaron geometry reflects the shape of the state with mixed $d_{x^2-y^2}/d_{z^2}$ character in the global coordinate frame (Figure 3.4) and explains the quasi planar shape of the

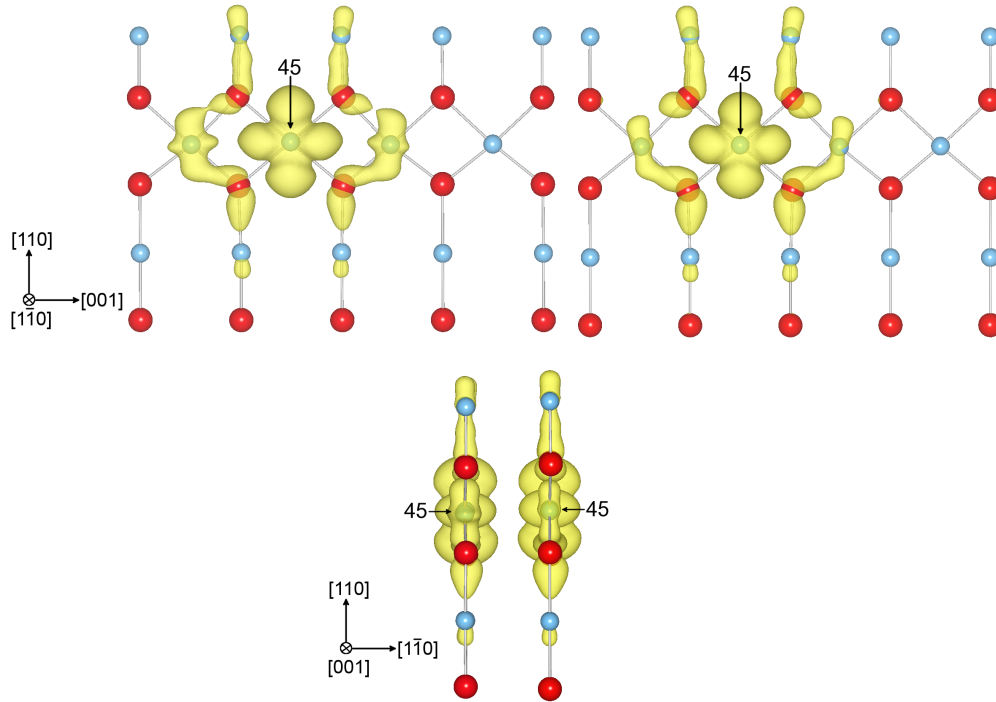


Figure 3.4 Charge density of the polaron state. Isosurface level is $0.0013 \text{ e}/\text{\AA}^3$. (top panel) side-view along $[001]$ direction. Left (right) panel HSE06 (PBE+ U). (bottom panel) side-view along $[1\bar{1}0]$ direction. Left (right) panel HSE06 (PBE+ U). Readers are referred to Figure 3.2 to identify the location of oxygen vacancy.

polaron. The bond length in the perpendicular direction is not altered compared to bulk. The volume of the octahedron connecting the nearest neighbors of the Ti center ion is increased by 11 % within HSE06 and by the same amount in PBE+ U calculations due to the polaron formation.

In order to investigate the difference between PBE+ U and HSE06, the charge density of the HSE06 polaron state minus the PBE+ U polaron state is shown in the bottom of Figure 3.5 (As the lattice relaxation is different between PBE+ U and HSE06, the charge density within PBE+ U was recalculated using the HSE06 relaxed lattice positions. The charge density obtained in this way looked identical to the right panel in Figure 3.4, i.e. no difference is seen in the charge density using the HSE06 or PBE+ U lattice positions.). Within PBE+ U the charge is calculated to be larger close to the center Ti ion (white) and smaller on the Ti neighbors (green). This indicates that PBE+ U overestimates the electron localization.

3.3.4 Polaron site

The final sites of the polarons are strongly dependent on the initial volume expansion. If the oxygen vacancy containing surface is calculated without initial local volume distortions, a solution with two polarons, one residing in the subsurface layer below the Ti6c* ion and one in the surface layer on Ti6c*, is found. In the following this configuration is denoted as 38-52 (see Figure 3.6). It is 0.9 eV higher in energy than the lowest energy configuration (see Table 3.2). (The polaron state centered on the Ti6c* ion is 0.5 eV below the conduction band compared to 1.2 eV for the subsurface polaron state.) In agreement with this calculation, Di Valentin *et al.* [22] did not vary the initial polaron positions and only found two polarons in the surface layer.

Providing an initial volume expansion (as referred to Scheme 2 above) around two arbitrary Ti ions still does not lead to the energetically lowest polaron configuration. Instead, both polarons are found in the subsurface layer, one below the Ti5c row and the other below the oxygen vacancy. In the following, this configuration is called 38-44 (see Figure 3.6). It is 270 meV higher in energy (see Table 3.2) and has two polaron peaks in the band gap. The spatial extension of the polaron is identical to the 44-45 configuration shown in Figure 3.4 with the exception of the orientation: The polaron lying below the oxygen vacancy has its charge distributed mainly in a plane perpendicular to the polaron shape of configuration 44-45. This polaron shape is mainly contained in a plane parallel to the surface, because the central Ti ion has its four oxygen neighbors in a plane parallel to the surface (see Figure 3.6). Since the state below the oxygen vacancy is not a part of the defect free unoccupied state (see Figure 3.1) the 38-44 configuration has to be higher in energy than 44-45 configuration. Also, it is found that a polaron in the third layer below the surface is unstable. Only when either initially replacing two Ti ions with V as proposed by Deskins *et al.* [27] (as referred to Scheme 1 above) or completely relaxing the oxygen vacancy before allowing for polaron formation (as referred to Scheme 3 above), the lowest polaron configuration 44-45 is found in agreement with Deskins *et al.* [27] and Kowalski *et al.* [51]. This indicates that the energy barrier of this 44-45 configuration is rather large. If the oxygen vacancy is not formed in advance, enlarging the oxygen cage around the polaron centers of configuration 44-45 does not lead to the 44-45 configuration but always go back to the 38-44

configuration.

Table 3.2 presents the relative energies of different polaron configurations calculated by different methods. One sees that the relative energy difference calculated by PBE+ U or HSE06 gives more or less identical results. Only for the second row, configuration 44-46, there is a difference between Deskins *et al.* [27] and PBE+ U results in this work whereas PBE+ U and HSE06 results are similar within this work.

Configuration 44-46 consists of both polarons within the same Ti row in the subsurface layer (see Figure 3.6). Both polarons are located below the same Ti5c row and are neighboring each other. This polaron state is a mixture of 77% d_{z^2} and 23% $d_{x^2-y^2}$ character within HSE06 and of 70% d_{z^2} and 30% $d_{x^2-y^2}$ character within PBE+ U in the global coordinate frame. We find this configuration to be 0.28 eV higher in energy, whereas Deskins *et al.* found it only 0.06 eV higher. This difference possibly caused by the following reasons:

In one inset (see Figure 3.2 in Ref. [27]) Deskins *et al.* showed the spin density of their polarons. As can be seen, one polaron has its extension in the plane of the four neighboring oxygens (blue color), but the other polaron has its extension in a plane perpendicular to the plane of the four oxygen neighbors. In the 44-46 configuration, the two polarons are neighbors, which implies that their charge density is slightly overlapping. (The polaron is mainly contained in the plane perpendicular to the Ti5c row and to the surface.) In present calculations, the two polarons in the 44-46 configuration consists of identical orbitals, whereas in the calculations of Deskins *et al.* [27], it seems that the two polarons consist of two orthogonal orbitals. Therefore the spatial overlap of the two polarons in configuration 44-46 will cost more in present calculation than in their calculation. The two polarons in configuration 44-46 having orthogonal states is in contradiction with both present calculations and the interpretation of the polaron formation. Therefore it is suspected that this difference might be related to the different basis set (Gaussian) in their calculation. This difference is important because if Deskins *et al.* are correct about the 44-46 configuration being energetically so close to the lowest 44-45 configuration, in experiment both configurations should be seen. If present calculations are correct, in experiment only configuration 44-45 should be seen. Further calculations and experiments have to shed light on this question.

A polaron containing two electrons on the same site is found to be unstable.

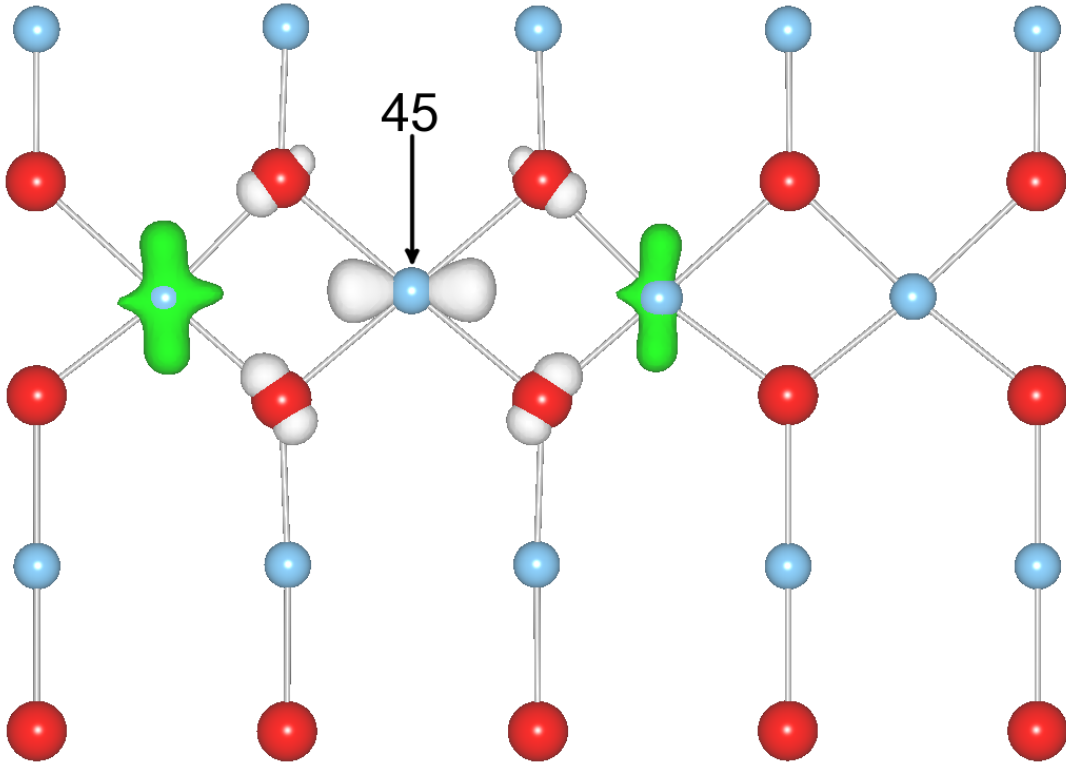


Figure 3.5 Polaron charge density difference: HSE06-PBE+ U . White indicates 'negative' and green indicates 'positive'. Isosurface level is $0.0013 \text{ e}/\text{\AA}^3$. Readers are referred to Figure 3.2 to identify the location of oxygen vacancy.

Table 3.2 Polaron energy in (eV) for different polaron sites.

	PBE+ U (Ref. [30])	DFT+ U (Ref. [27])	PBE+ U (Ref. [51])	PBE+ U (this work)	HSE06 (this work)
44-45	0	0	0	0	0
44-46	0	0.06	-	0.28	0.28
38-44	0	0.23	0.22	0.23	0.27
38-52	0.3	0.96	-	-	0.90

This is concluded from the fact that a solution with one ion being doubly occupied is unfavorable in a calculation with a (2×1) unit cell where only one ion initially was distorted. This indicates that the on site Coulomb repulsion between two d-electrons is larger than the energy difference between the singly occupied polaron state and the conduction band edge, i.e. larger than 1.2 eV.

Krüger *et al.* [65] used resonant photoelectron diffraction to probe defect states at

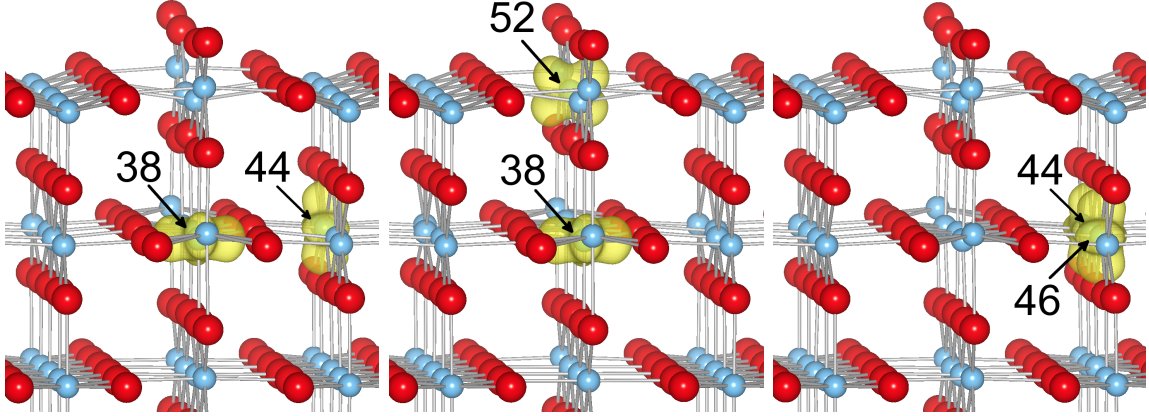


Figure 3.6 Charge density of the polaron state for three different polaron geometries as described in the text. Isosurface level is $0.015 \text{ e}/\text{\AA}^3$.

the rutile TiO_2 (110) surface. They conclude that a substantial part of the probed defect charge is located on subsurface layers, with a maximum on the subsurface Ti ion located below the Ti5c row. They find negligible charge of the subsurface Ti ion below the Ti6c row. The surface layer sites Ti6c* and Ti5c they find to carry a small, but non-negligible amount of charge. These experimental findings rule out Di Valentins [22] calculations but confirm our, Kowalskis [51], and Deskins [27] results, because they only find polarons on Ti ions located below the Ti5c row.

Yim *et al.* [45] employed STM and photoemission spectroscopy to investigate the origin of the band-gap state on the rutile TiO_2 (110) surface. They measure the band-gap state to be located at about 0.9 eV below the conduction band edge with a width on the order of about 0.5 eV and establish that the band-gap state originates from bridging oxygen vacancies and not, as has been proposed [15], by Ti interstitial defects. The location and width of the band-gap state is in agreement with this calculations (see Figure 3.3).

In present calculations, both parallel and antiparallel spin configurations are found out to be stable, whereas a nonmagnetic polaron configuration is unstable. Table 3.3 shows the calculated energy differences. Lowest in energy is the antiparallel spin configuration with a total moment of $0 \mu_B$. A parallel spin-configuration with a total moment of $2 \mu_B$ is found to be only 0.1 meV higher. The nonmagnetic solution, where the two excess electrons are in the conduction band, is calculated to be 1 eV higher than the lowest energy configuration. In contrast to Deskins *et al.* [27], the polaron states in this work have the same symmetry independent of

parallel or antiparallel spin configurations. The symmetry of the polaron state is found to be governed entirely by the orientation of the plane containing the polaron center and its four oxygen neighbors. This result is independent of using PBE+ U or HSE06.

Table 3.3 Energetics of magnetic structures in (eV).

	AFM	FM
44-45	0	10^{-4}
44-46	0.28	0.30
38-44	0.270	0.278

3.4 Summary

In this work, a systematic comparison between PBE+ U and HSE06 methods were carried out to study the polaron formation due to an oxygen vacancy at the rutile TiO₂ (110) surface. A polaron state was found in the band gap, 1 eV below the conduction band edge having an energy width of about 0.3 eV. The spatial extent of each polaron is about (6.5×7) Å along the basal plane of the Ti centered octahedron. The two polarons are in a singlet state, but the triplet state is only about 0.1 meV higher in energy. Comparing PBE+ U and HSE06, it was found that for the (4×2) cell size PBE+ U ($U = 4.2$ eV) and HSE06 give more or less identical relative energies. There is a difference in the relaxation pattern, but its contribution to the energy differences (relative energies) is negligible. The polaron geometry is identical for PBE+ U and HSE06. The occurrence of subsurface polarons is explained in terms of spatial symmetry breaking, where the defect free unoccupied lowest state becomes localized on only two subsurface Ti sites.

Chapter 4

Bipolaron formation near and far from the oxygen vacancy

4.1 Introduction

TiO₂ surfaces and interfaces have been widely studied for a wide variety of technological applications such as solar cells, [66] photocatalysts [67] or memristive devices. [68] A reduced TiO₂ (110) surface shows a Ti³⁺ state in the band gap about 1 eV below the conduction band edge. [69] This state is believed to have an important role in modifying the rich functionalities of TiO₂ surfaces. [70,71] Although it is under discussion, [15] a general belief is that the surface bridging oxygen vacancy (V_O) is one of the main causes for the occurrence of a Ti³⁺ state. [42] In addition, the V_O itself has a role in chemical reactions such as for example in water-splitting. [72] On the theoretical side it is now well established that density functional theory (DFT) employing the standard local density approximation or the generalized gradient approximation fails to predict the localized states of oxygen vacancies in transition metal oxides such as for example CeO₂, MoO₃ and V₂O₅. [19–21] On the other hand, Di Valentin *et al.* [22] have recently shown that B3LYP calculations are capable to describe an V_O . They calculate the two excess electrons induced by the oxygen vacancy to become localized and forming a polaron at two different Ti sites. Further, the formation of a polaron at a Ti site is equivalent to the creation of a Ti³⁺ state. Di Valentin's study stimulated research on the spatial relationship between the relative placement of an V_O and the location of the polarons. Recent hybrid functional and DFT + U calculations show that Ti³⁺ is more stable in the subsurface layer than in the surface. [27,30] Resonant photoelectron diffraction experiments by Krüger *et al.* support this subsurface location

of Ti^{3+} . [73] Even for other transition metal oxides such as for example CeO_2 the spatial distribution of excess electrons induced by oxygen vacancies is an important topic. [74] In summary, so far the energetics of polaronic positions close to the oxygen vacancy has been studied. In this chapter however, an attempt is made to give a complete picture of the spatial relationship between the polaronic sites and an V_{O} including the conditions for polaron formation. Specifically, this chapter gives answers to the following three questions:

1. Under which conditions are polarons formed?
2. Does an V_{O} trap a single polaron?
3. Does a bipolaron form in close proximity of an V_{O} ?

The answer to these questions becomes crucial, e.g., for the dissociative reaction of H_2O or O_2 at the bridging oxygen vacancy. [75] In that type of reaction, both the Ti^{3+} and the V_{O} play an important role. The understanding of such dissociative reactions thus requires the complete understanding of the spatial relationship between the polaronic sites and an V_{O} .

In order to answer these questions, first principles DFT calculations were performed using hybrid functionals. A bridging oxygen vacancy was calculated to induce the formation of a bipolaron, or Ti^{3+} - Ti^{3+} pair. The existence of a bipolaron has earlier been reported in connection with the metal-insulator transition of the Magnéli phase, Ti_4O_7 . [76–80]

Figure 4.1 shows the neutral (110) surface with a bridging oxygen vacancy and its schematic representation. The two polarons are present in the subsurface layer 5.80 Å away from the center of the oxygen vacancy and 7.15 Å apart from each other. In previous chapter it has been shown that the polarons are most stable in the subsurface layer close to the V_{O} . The schematic representation summarizes the particular characteristics of the V_{O} , which are the number of localized electrons and the calculated lattice distortion around the localized electron. In order to analyze the interactions among V_{O} and polarons, 10 configurations of the $p(4 \times 2)$ surface unit cell were calculated as shown in Figure 4.2. Each configuration is calculated within the supercell approximation. Total energy calculations of charged defects in finite-size supercells include an unwanted defect-defect interaction. [81,82] Many of the known correction schemes are either computationally too expensive for the here performed HSE06 calculations or not generally reliable to minimize the error. [81,82] On the other hand a cheap and reliable correction scheme is "potential

realignment”, [83] where the potential in the defect cell is aligned to that of bulk. The calculated formation energies were corrected with the ”potential realignment” scheme by comparing the potential at a point furthest away from the defect with the same point in a defect free supercell. The correction amounts to 34 meV. Both the method and available supercomputers restrict the size of the here used supercell to 192 atoms. In the following the remaining finite size errors are assumed to be negligible and use each configuration to discuss properties of isolated defects at the surface. The calculated configurations can be divided in 2 types; V_O surface (reconstructed surface with an oxygen vacancy) and ideal surface (reconstructed surface without an oxygen vacancy). The V_O (ideal) surface was used to discuss the stability of polarons close to (infinitely far away from) an V_O . The number of polarons was varied from 2 to 0 for both types of configurations by changing the total number of electrons in the overall neutral supercell.

The neutral V_O surface has two polarons (Figure 4.2a). When the V_O surface becomes +1 charged, it loses one of its polarons. It is emphasized that the loss of one polaron does not cause the formation of new bonds (Figure 4.2c). The +2 charged V_O surface has no polaron (Figure 4.2e). Similarly, the number of polarons on the ideal surface (Figure 4.2j) is varied. The -1 and -2 charged ideal surfaces have one (Figure 4.2h) and two (Figure 4.2f) polarons respectively. For all configurations the same lattice sites for the polarons were used. This lattice site has earlier been calculated to be most stable for both the neutral V_O surface [27] and for the -1 charged ideal [26] surface.

In order to estimate the energy contribution of the polaronic lattice distortion, 4 frozen configurations were calculated. A frozen configuration includes the polaronic lattice distortion but excludes the electron localized at that site as shown in Figure 4.2b,d,g,i. The frozen V_O surface with two (one) polaronic lattice distortions (Figure 4.2b, (d)) corresponds to the +2 charged V_O surface but with the geometry of the neutral (+1 charged) V_O surface. Similarly, the frozen ideal surface with two (one) polaronic lattice distortions (Figure 4.2g, (i)) corresponds to the charge neutral ideal surface but with the geometry of the -2 (-1) charged ideal surface.

The defect formation energies are defined as follows:

$$E_{\text{form}}^{\text{V}_O, q} = E_{\text{tot}}^{\text{V}_O, q} + \frac{1}{2}\mu_{\text{O}_2} + q(\varepsilon_v + E_F) - E_{\text{tot}}^{\text{ideal}}. \quad (4.1)$$

$$E_{\text{form}}^{\text{ideal}, q} = E_{\text{tot}}^{\text{ideal}, q} + q(\varepsilon_v + E_F) - E_{\text{tot}}^{\text{ideal}}. \quad (4.2)$$

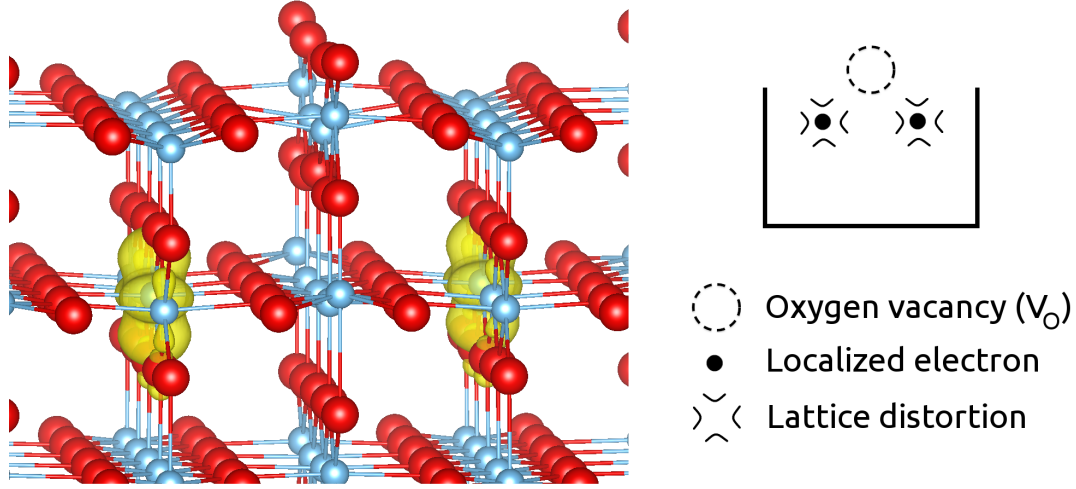


Figure 4.1 The calculated surface (left) and its schematic representation (right). Dark circle (red): O, light circle (blue): Ti. The charge density of the energetically lowest polaronic state is shown for the isosurface level = $0.005 \text{ e}/\text{\AA}^3$ (Yellow). The figure on the right depicts the picture of an oxygen vacancy and a bipolaron consisting of localized electrons and associated lattice distortions.

$E_{\text{form}}^{V_O, q}$ ($E_{\text{form}}^{\text{ideal}, q}$) is the formation energy of the $+q$ charged V_O (ideal) surface. In other words, $E_{\text{form}}^{\text{ideal}, q}$ is the polaron formation energy of $-q$ polarons forming under the ideal surface. $E_{\text{tot}}^{V_O, q}$ ($E_{\text{tot}}^{\text{ideal}, q}$) is the calculated total energy of the $+q$ charged V_O (ideal) surface. $E_{\text{tot}}^{\text{ideal}}$ is the calculated total energy of the neutral ideal surface. μ_{O_2} is the chemical potential of the oxygen reservoir. The value for the O-rich limit was obtained from the total energy calculation of the ground state spin triplet O_2 molecule. For the Ti-rich limit, the total energy of bulk TiO_2 minus the total energy of bulk hcp Ti was used. ε_v is the valence band maximum of the ideal surface at the Γ point. E_F is the Fermi energy which is set to zero at ε_v . The shift of the electrostatic potential [83] of an O deficient surface was corrected. The shift amounted to 34 meV.

4.2 Methods

The calculations were performed using a plane wave based pseudopotential code, VASP. [55,56] The exchange-correlation potential was approximated within the generalized gradient approximation (GGA) by the Perdew-Burke-Ernzerhof (PBE). [33] In order to overcome GGA's semilocal description, the screened hybrid functional

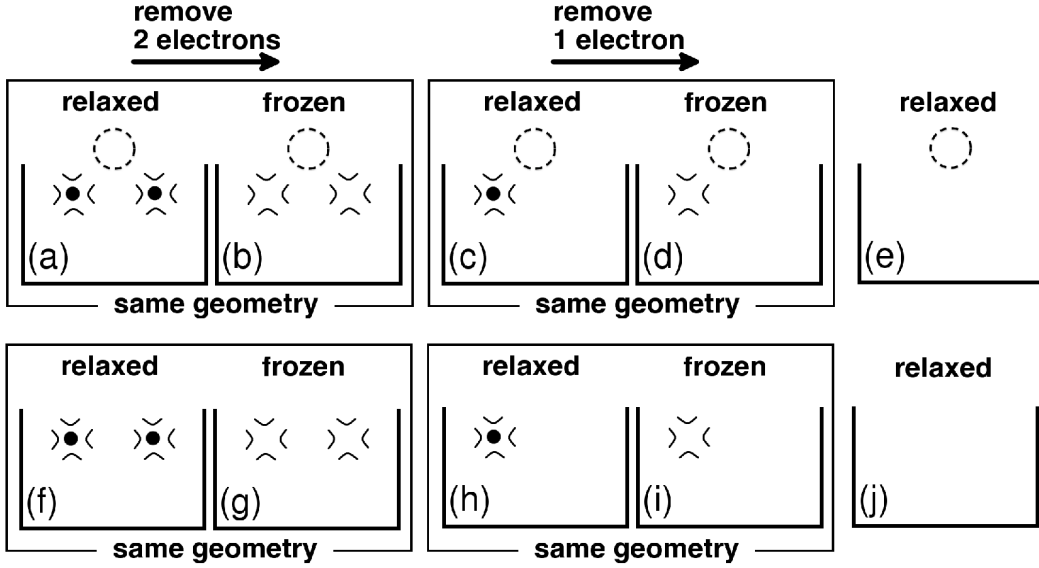


Figure 4.2 Schematic images of calculated 10 configurations. (a) neutral V_O surface with two polarons; (b) +2 charged V_O surface with a geometry taken from (a); (c) +1 charged V_O surface with one polaron; (d) +2 charged V_O surface with a geometry taken from (c); (e) +2 charged V_O surface with no polaron; (f) -2 charged ideal surface with two polarons; (g) neutral ideal surface with a geometry taken from (f); (h) -1 charged ideal surface with one polaron; (i) neutral ideal surface with a geometry taken from (h); (j) neutral ideal surface with no polaron.

of Heyd, Scuseria, and Ernzerhof (HSE06), [34, 35] where correlation is described in GGA (PBE) and the exchange is a mixture of 25% exact (HF) exchange and 75% PBE exchange, was employed. The HSE screening parameter was set to 0.2 \AA^{-1} . The HSE06 functional has been successfully applied for studying oxygen vacancies in bulk rutile TiO_2 by Janotti *et al.*, [54] where they found the HSE06 functional to improve the agreement between the calculated ground state properties and the experimental results. The surface was modeled by a $p(4 \times 2)$ geometry with a slab thickness of 4 layers separated by 10 \AA vacuum. This amounts to 128 O and 64 Ti ions. The bottom layer was fixed at bulk positions and terminated by pseudohydrogen [38] atoms. The (1×1) surface reconstruction of the (110) surface of TiO_2 , throughout this text termed ideal surface, was calculated to be lowest in energy. [43] The plane wave cut-off energy was 450 eV and the core-valence interaction was described by the projector augmented wave approach (PAW). The Brillouin zone was sampled by Γ point. It was checked that calculations with more k points yield similar results as the Γ point calculations. Lattice parameters of $a = 4.60 \text{ \AA}$ and

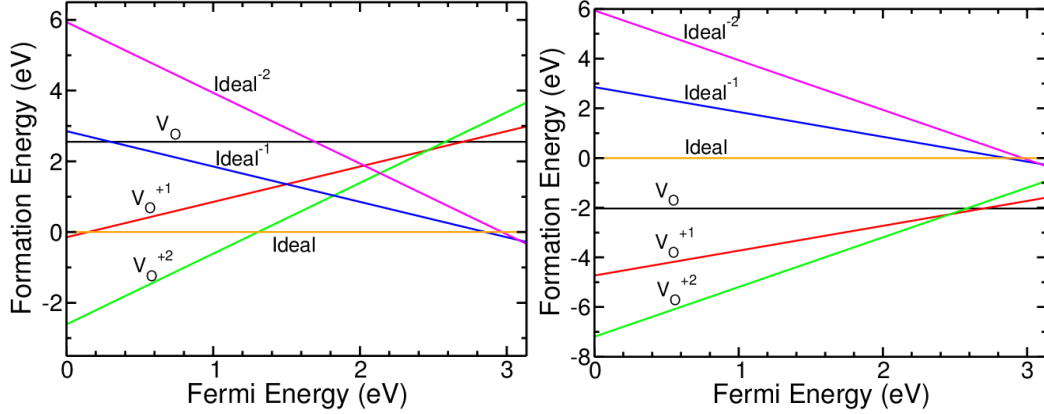


Figure 4.3 Formation energies of the oxygen vacancy (denoted as V_O) and the ideal surface (denoted as $Ideal$) for different charge states as a function of the electron chemical potential for O-rich (left) and Ti rich (right) conditions. The formation energies are shown with respect to the one for the neutral ideal surface. The electron chemical potential at the valence band edge is set to be zero.

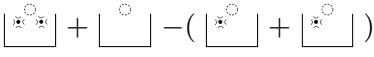
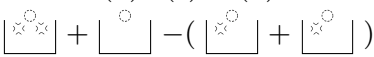
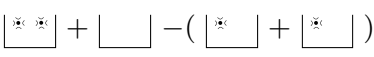
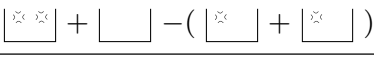
$c = 2.95 \text{ \AA}$ were determined by fitting the calculated energy-volume curve to the Birch-Murnaghan 3rd order equation of state. [84] Hellmann-Feynman forces were reduced below 0.02 eV/\AA .

4.3 Results

4.3.1 Formation energy

Figure 4.3 shows the defect formation energies as defined in Eqs. (4.1) and (4.2) for both O-rich conditions (left panel) and Ti-rich conditions (right panel). For O-rich conditions the +2 charged V_O surface (Figure 4.2e) is calculated to be lowest in energy for Fermi energies below 1.33 eV. For Fermi energies between 1.33 eV and 2.85 eV the ideal surface (Figure 4.2j) is calculated to be lowest in energy. For Fermi energies between 2.85 eV and 3.08 eV the -1 charged ideal surface (Figure 4.2h) is calculated to be lowest in energy. Finally, for Fermi energies larger than 3.08 eV the -2 charged ideal surface (Figure 4.2f) is calculated to be lowest in energy. On the other hand, for Ti-rich conditions, the V_O surface is always lower in energy than the ideal surface independent of Fermi energy or charge state. For Fermi energies below 2.46 eV the +2 charged V_O surface (Figure 4.2e) is calculated to be lowest in energy. In other words, if there are other defects in the sample that provide an

Table 4.1 Polaron-polaron interaction and its lattice contribution. Figure 4.2 is referred to denote the configurations in the table. The specific subsystems used to define each configuration exactly corresponds to the subfigures in Figure 4.2.

Notation	Energy (meV)	Configurations (See Figure 4.2)	Description
E_1	236	(a)+(e)-2(c) 	Polaron-polaron interaction energy close to V_O
E_1^{latt}	32	(b)+(e)-2(d) 	Lattice contribution on E_1
E_2	229	(f)+(j)-2(h) 	Polaron-polaron interaction energy infinitely far away from V_O
E_2^{latt}	45	(g)+(j)-2(i) 	Lattice contribution on E_2

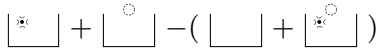
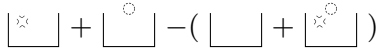
electron reservoir with a Fermi energy below 2.46 eV, no polaron will form close to an V_O . For Fermi energies between 2.46 eV and 2.70 eV the +1 charged V_O surface (Figure 4.2c) is calculated to be lowest in energy. Only for Ti-rich conditions and for Fermi energies larger than 2.70 eV the neutral V_O surface with two polarons (Figure 4.2a) is calculated to be lowest in energy.

From the above analysis, question 1 can be answered as following: Under O-rich conditions no polaron exists for Fermi energies below 2.85 eV. Only then a polaron becomes stable at the ideal surface. Under O-rich conditions an V_O surface is thus never accompanied by any polarons. On the other hand, under Ti-rich conditions no polaron exists for Fermi energies below 2.46 eV. For higher Fermi energies, an V_O surface will under Ti-rich conditions always be accompanied by a polaron.

4.3.2 Analysis of interactions

In this subsection, the interactions among an V_O and polarons are analyzed by comparing systems, which have the same number of electrons. The system consists of two or three subsystems chosen from 10 configurations shown in Figure 4.2. For polaron-polaron and V_O -polaron interactions, two subsystems are picked and they are considered as one system. Then another two subsystems are chosen and a different system is made so that it has the same number of electrons to have

Table 4.2 V_O -polaron interaction and its lattice contribution. The configurations are denoted by same convention as in Table 4.1.





Notation	Energy (meV)	Configurations (See Figure 4.2)	Description
E_3	427	(h) + (e) - ((j) + (c)) 	V_O -polaron interaction energy
E_3^{latt}	-15	(i) + (e) - ((j) + (d)) 	Lattice contribution on E_3

a direct comparison with the previous one. Table 4.1 shows the polaron-polaron interaction energy for positions close to V_O and infinitely far away from V_O . In E_1 two configurations are compared: (i) with V_O and two polarons (Figure 4.2a) where the polaron-polaron distance is 7 Å (ii) V_O and one polaron (Figure 4.2c) corresponding to an infinite separation between two polarons (for details, see Table 4.1). The energy difference is 236 meV. It means that polarons repel each other by this amount. It is natural to decompose the polaron-polaron interaction energy (E_1) into two parts, an electrostatic contribution and a lattice distortion contribution. The lattice distortion contribution, E_1^{latt} , is calculated in the same way as is done for E_1 , but the corresponding frozen configurations (Table 4.1) is used. For example, instead of using the configuration with two polarons close to an V_O (Figure 4.2(a)), the corresponding frozen configuration (Figure 4.2(b)), where no polarons are included but the lattice distortion due to the polaron formation is still present, is used. E_1^{latt} is calculated to be 32 meV (14% of E_1).

Correspondingly, the polaron-polaron interaction energy (E_2) is calculated for polarons being infinitely far away from an V_O . E_2 is calculated to be 229 meV, which is more or less identical to E_1 . The corresponding lattice distortion contribution E_2^{latt} is calculated to be 45 meV (20% of E_2). It is concluded that polarons are repulsive regardless whether they are close to an V_O or infinitely far away from it. The repulsive polaron-polaron interaction is more or less independent on the polaron- V_O distance and is about 230 meV. The lattice distortion contribution is less than one fifth of the total polaron-polaron interaction, suggesting that the main contribution comes from the electrostatic repulsion between the two localized electrons.

Next, the V_O -polaron interaction energy, E_3 , which is shown in Table 4.2 is

Table 4.3 V_O -two polaron interaction. Same convention as in Table 4.1 has been used to describe the configurations.

Notation	Relative energy (meV)	Configurations (See Figure 4.2)	Description
E_4	0	(a)+2(j) 	2 polarons near V_O
E_5	192	(c) + (h) + (j) 	1 polaron near V_O , 1 polaron far away
E_6	848	(e) + (f) + (j) 	2 polarons far away from V_O
E_7	619	(e)+2(h) 	2 polarons, infinitely separated and far away from V_O

discussed. On one hand, the configuration of one polaron sitting infinitely far away from an V_O is added with the configuration of a +2 charged V_O (no polarons). On the other hand, the configuration of the neutral ideal surface is added with the configuration of one polaron sitting close to an V_O (see Table 4.2). The difference between these two sums (E_3) measures the V_O -polaron interaction energy. Note, that the two sums again contain the same number of electrons. E_3 is calculated to be 427 meV, which implies that an V_O attracts a polaron. The rutile (110) TiO_2 surface gains 427 meV if the distance between a polaron and an V_O changes from infinity to 7 Å. Again the corresponding frozen configurations (see Figure 4.2) are used to calculate the lattice contribution E_3^{latt} of the V_O -polaron interaction energy. E_3^{latt} is calculated to be -15 meV (4% of E_3). The negative value implies that the lattice distortion around an V_O slightly prevents the polaronic lattice distortion.

In summary, from the above analysis of the polaron-polaron interaction and the V_O -polaron interaction, it is concluded that an V_O attracts a polaron by 427 meV and its main driving force is of electrostatic nature. The lattice contribution is negligible. Therefore it can be stated that an V_O traps a polaron, which provides the answer to question 2 posed above.

Finally, the three-body interaction of two polarons and an V_O is discussed. For this analysis the energy sums of three configurations as shown in Table 4.3 are compared. This guarantees that the configuration sums always contain one V_O and two polarons:

(i) The energy sum E_4 consists of the neutral V_O surface (Figure 4.2a) plus two neutral ideal surfaces (Figure 4.2j). Here both polarons are close to the V_O .




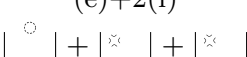
(ii) The energy sum E_5 consists of the +1 charged V_O surface (Figure 4.2c) plus the -1 charged ideal surface (Figure 4.2h) plus the ideal surface (Figure 4.2j). Here only one polaron is close to the V_O and the other polaron is infinitely far away from both the other polaron and the V_O .

(iii) The energy sum E_6 consists of the +2 charged V_O surface (Figure 4.2e) plus the -2 charged ideal surface (Figure 4.2f) plus the neutral ideal surface (Figure 4.2j). Here both polarons are infinitely far away from the V_O , but the two polarons are close together.

(iv) The energy sum E_7 consists of the +2 charged V_O surface (Figure 4.2e) plus two -1 charged ideal surfaces (Figure 4.2h). Here both polarons are infinitely far away from both the V_O and each other.

Table 4.3 gives the calculated energy sums relative to E_4 , which had the lowest value. The energy sums shown in Table 4.3 clearly reflect the fact that two polarons repel each other and the V_O attracts polarons. Several conclusions can be made. (a) If one polaron moves from infinitely far away close to an V_O (going from E_7 to E_5), the system gains an energy of 427 meV. This implies that an V_O attracts a polaron with an energy of 427 meV. (b) If one polaron moves from infinitely far away close to another polaron, but still both of them being infinitely far away from an V_O , (going from E_7 to E_6), it costs 229 meV. This implies that the two polarons repel each other with an energy of 229 meV, which is identical to the earlier analysis of the polaron-polaron interaction (see Table 4.1). (c) If one polaron from being close to the other polaron moves to become close to an V_O instead, (going from E_6 to E_5), the system gains 656 meV. This energy gain consists of on one hand the V_O -polaron attraction energy of 427 meV and on the other hand the loss of the polaron-polaron repulsion energy of 229 meV ($427 + 229 = 656$). (d) If one polaron from being infinitely far away from both polaron and V_O moves close to both a polaron and an V_O , (going from E_5 to E_4), the system gains 192 meV. This implies that an V_O with one close polaron still attracts another polaron with an energy of 192 meV. Again this energy gain can be analyzed in the following way: The V_O attracts the second polaron with an energy of 427 meV (even if there already is a close first polaron) but the close first polaron repels the second polaron with an energy of 236 meV ($427 - 236 = 191$). (e) If two close polarons infinitely far away

Table 4.4 Lattice distortion contribution to V_O -two polaron interaction. Same convention as in Table 4.1 has been used to describe the configurations.

Notation	Relative energy (meV)	Configurations (See Figure 4.2)	Description
E_4^{latt}	0	(b)+ 2(j) 	2 polaronic distortions near V_O
E_5^{latt}	-47	(d)+ (i)+(j) 	1 polaronic distortion near V_O , 1 polaronic distortion far away
E_6^{latt}	-17	(e)+ (g)+(j) 	2 polaronic distortions far away from V_O
E_7^{latt}	-62	(e)+2(i) 	2 polaronic distortions, infinitely separated and far away from V_O

from an V_O both move close to the V_O , (going from E_6 to E_4), the system gains 848 meV. This implies that an V_O attracts a pair of polarons, a bipolaron, with an energy of 848 meV.

Table 4.4 shows the lattice distortion contribution. All are negative meaning that the lattice distortion around V_O is the least favorable. In terms of lattice distortion, polaron prefers to be apart from both V_O and another polaron. However, the contribution of lattice distortion is much smaller compared to the values presented in Table 4.3, indicating that the electrostatic contribution plays the major role. It is concluded that the positively charged oxygen vacancy attracts the two polarons. Therefore, an oxygen vacancy on the TiO_2 (110) rutile surface is expected to be accompanied by two polarons, i.e. a bipolaron. The bipolaron solution is about 190 meV lower than having only a single polaron close to the vacancy and a second polaron far away from the vacancy. Therefore, it can be concluded that the oxygen vacancy is dressed by a bipolaron.

4.3.3 The stability of a negatively charged V_O

In the following the question if an V_O traps more than two polarons is addressed. Although the configuration of an V_O surrounded by more than two polarons was not calculated, an attempt is made to estimate the stability of a negatively charged V_O . There are four symmetry equivalent positions for the energetically most stable polaron below an V_O (see Figure 4.4). Therefore one can naturally extend the

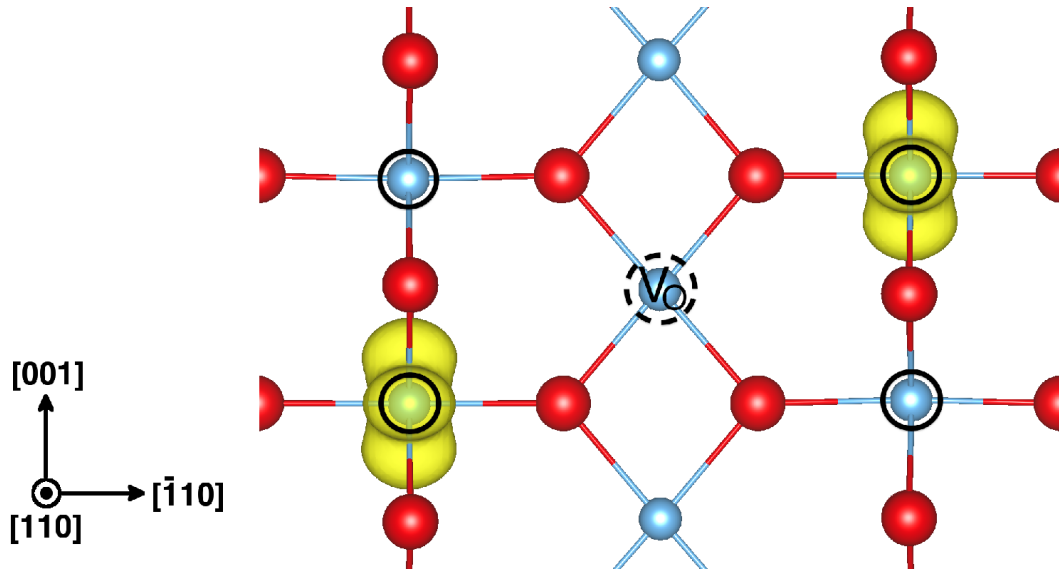


Figure 4.4 Top-view of neutral V_O surface. Here, only 2nd layer is shown. Stable position of polarons and its symmetrically equivalent position are indicated by solid black circle. Two of them are already occupied by polaronic states (yellow). Isosurface level = $0.01 e/\text{\AA}^3$. The dotted black circle shows the location of V_O .

discussion in the previous subsection to the -1 and -2 charged V_O . The four symmetry equivalent positions form a rectangle. Two of them are diagonally occupied under neutral V_O as shown in Figure 4.4.

First, the case of a -1 charged V_O , which has three polarons, is considered. Let us consider the configuration in which the three polarons are both infinitely far away from an V_O and from each other, which is presented in Figure 4.5(i). This is the lowest-energy configuration while avoiding polaron formation close to a V_O , because polarons simply repel each other when they come close. One can gain energy of about 430 meV by moving one polaron close to an V_O (Figure 4.5 (i) to (ii)). In the same way, one can gain 430 meV by moving a second polaron close to the V_O , but this time the system has to pay about 230 meV due to the polaron-polaron repulsion. Therefore the net energy gain is about 200 meV (Figure 4.5 (ii) to (iii)). On moving a third polaron close to the V_O the system gains once again 430 meV. However, since there are already two polarons around the V_O , the system has to pay about 460 meV. It makes the configuration of three polarons close to an V_O less favorable than the configuration with only two polarons at an V_O by 30 meV (Figure 4.5 (iii) to (iv)). As shown in previous chapter, the polaron-polaron repulsion becomes higher by few hundreds meV for two polarons sitting close along

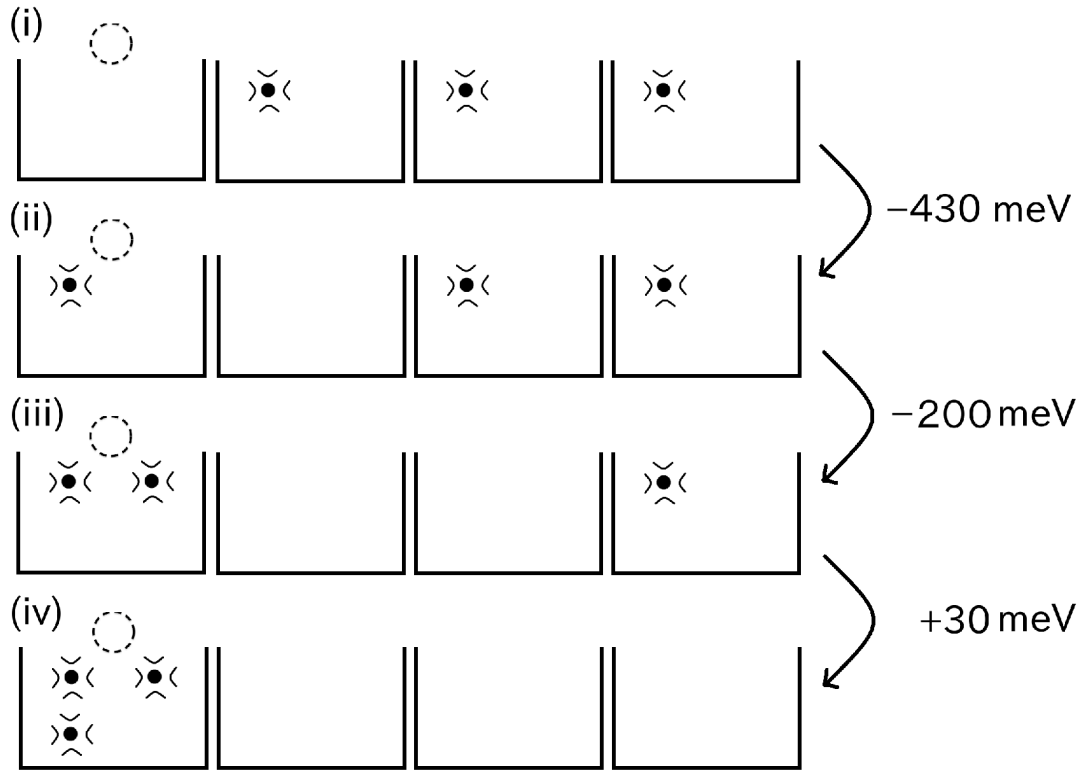


Figure 4.5 The conceptual image of a formation of three-polaron under V_O . (i) Three polarons are infinitely far away from V_O . (ii) One polaron is under V_O , two are infinitely far away. (iii) Two polarons are under V_O , one is infinitely far away. (iv) Three polarons are under V_O . For a definition of the schematic images, see Figure 4.1 and Figure 4.2.

the [001] direction (see Figure 4.4). Choosing more than three positions out of four rectangular corners leads to a formation of this high-energy configuration. Indeed, the additional PBE+ U ($U = 4.2 \text{ eV}$) calculation confirms that the three polaron structure has an energy loss of 304 meV (Figure 4.5 (iii) to (iv)). It is an order of magnitude greater than the estimated value of 30 meV.

Second, the case of a -2 charged V_O , is considered. The -2 charged V_O is created by adding one more polaron to the -1 charged V_O configuration. The repulsion between polarons amounts to about 230 meV for a polaron-polaron distance as shown in Figure 4.4. This addition of a polaron helps to gain 430 meV (V_O - polaron attraction) but also costs about 690 meV (three times polaron - polaron repulsion), leading to a net energy cost of at least 260 meV. Therefore, it is concluded that a negatively charged V_O is not favorable, making a bipolaron the most stable polaron structure close to an V_O residing at the surface of rutile (110) TiO_2 . Hence, as an

answer to question 3, it is stated that a bipolaron forms in close proximity of an V_O .

4.4 Summary

The density functional theory was employed in conjunction with a screened hybrid functional to study some important aspects of the polaron formation in the presence of an oxygen vacancy at the rutile $TiO_2(110)$ surface. From the detailed calculations it was concluded that a bipolaron is stable only in close proximity of an oxygen vacancy. The energy contribution of lattice deformations is negligible compared to the electrostatic interaction. The calculated formation energies reveal that under O-rich conditions a bipolaron is unstable and single polarons start to form "spontaneously" at the ideal surface for Fermi energies above 2.85 eV. For Ti-rich conditions a bipolaron becomes stable for Fermi energies above 2.7 eV.

Chapter 5

Comparison with the filled state STM

5.1 Introduction

Rutile TiO_2 (110) is researched as a prototypical surface of catalytically and photo-electrochemically active metal oxides. The surface consists of alternating five-fold coordinated Ti (Ti_{5c}) rows and bridging oxygen rows having six-fold coordinated Ti (Ti_{6c}) rows beneath them. To study the role of surface defects for surface reactivity, reduced surfaces are intensively studied. The reduced surface is produced by cycles of ion sputtering and vacuum annealing, which create surface bridging oxygen vacancies (V_O) and Ti interstitials. Surface reactivity is usually associated to V_O as well as Ti $3d$ states in band gap. The gap states are observed about 1 eV below the Fermi level in electron energy loss spectroscopies (EELS) and photoelectron spectroscopies (PES). [10, 85–87] However, sources of these gap states and a spatial distribution including a degree of localization are not fully understood. While V_O is considered as a main source of these states [45, 86, 88, 89] supporting the so-called “oxygen-vacancy model” proposed by Henrich *et al.*, [10] there are reports in which subsurface Ti interstitials are claimed to be responsible for the gap states. [15–18] Regarding the spatial distribution of Ti $3d$ states, Henderson *et al.* proposed that those states are delocalized to some extent at the surface to explain a saturation coverage of chemisorbed O_2 , assuming that a V_O is charge neutral. [86] The delocalized view was also adopted to account for the occurrence of a dissociation of a O_2 molecule at Ti_{5c} row, [90] as well as STM image [2]. On the other hand, recently it has been recognized that localized Ti $3d$ states are responsible for the gap states [22], and their spatial distribution is mainly in subsurface. [27, 30] This

view is supported by recent resonant photoelectron diffraction experiment. [73]

Filled state STM is a promising tool to resolve these questions. By applying negative bias voltage, gap states are directly imaged. There are several atomic-scale images available in literatures, [2, 24, 25] bias voltage varying from -2 to -1 V, following earlier attempts. [12, 13] However, in contrast to empty state image which has an established interpretation, [11] there is no agreement in the interpretation of the filled state STM image. While Minato *et al.* reported that V_O -induced Ti 3d states are delocalized on the first layer, [2] Papageorgiou *et al.* concluded that they are delocalized at first to third layer and only -2 charged V_O can reproduce STM image. [24] On top of that, very recently Setvin *et al.* interpreted them as a weighted average of Ti 3d states localized at 1st and 2nd layer. [25]

Their interpretations are based on the density functional theory (DFT) calculation, and these discrepancies reflect the differences in their calculation results. Although Ti 3d states appear by either introducing donor defects such as oxygen vacancies or adding extra electrons to a defect-free structure, treating them properly is not so straight-forward. Depending on exchange-correlation functional, initial structure in lattice relaxation and surface cell size, a calculation gives a different result. Consequently, a proper way was not known until very recently. To properly describe gap states within DFT, a self-interaction error in exchange-correlation functional should be corrected. This was first recognized in 2006 by adopting hybrid functional [22] and then by DFT+ U . [23] A Ti 3d state localized at a Ti site expands Ti-O bonds around forming a Ti^{3+} , or a polaron. There are many local minima in lattice structures associated with a Ti^{3+} . In other words, depending on the initial structure, Ti^{3+} can be stabilized at almost any Ti sites in the surface. This was first thoroughly investigated in 2011 by systematic DFT+ U study. [27, 30] These studies showed that among all sites, 2nd-layer below Ti_{5c} row (Ti_{5c-2nd}) is the most stable site. [27] Each Ti^{3+} has a finite density at neighboring Ti sites. In the case of the most stable structure, Ti^{3+} at Ti_{5c-2nd} site, a Ti^{3+} covers three Ti_{5c-2nd} sites, 70 % at the center and 15 % at neighbors as shown in Chapter 3. They behave almost independently unless they overlap, which result in an increase in total energy as shown in Chapter 3. This becomes important especially when one deals with multiple Ti^{3+} in one cell.

In this section, all these findings are incorporated into the interpretation of filled state STM, and demonstrate that reported STM images can be consistently in-

terpreted by careful DFT calculations with screened hybrid functionals as well as sufficiently large calculation cells. First, a typical image taken at 78 K [2] is reproduced and explained. A key feature is a bright blob in Ti_{5c} row which is interpreted as a Ti^{3+} at Ti_{5c-2nd} site. Then, from total energy comparisons between localized and delocalized states in a defect-free surface, it is suggested that having an effectively occupied Ti_{5c-2nd} sites is a prerequisite for Fermi energy being at conduction band edge. Based on these understandings, images of a more reduced surface at 78 K [25] and 5 K [24] are interpreted and explained. Finally, the temperature dependency of V_O reactivity is proposed to be behind a seemingly contradicting reports about an O_2 saturation coverage. [16, 18, 86, 91]

5.2 Computational details

The calculations were performed using a DFT code, VASP. [55, 56] The exchange-correlation potential was approximated within the generalized gradient approximation (GGA) by the Perdew-Burke-Ernzerhof (PBE). [33] In order to overcome GGA's semilocal description, screened hybrid functional (HSE06), [34, 35] where correlation is described in GGA (PBE) and the exchange is a mixture of 25 % exact (HF) exchange and 75 % PBE exchange was employed. The HSE screening parameter was set to 0.2 \AA^{-1} . The surface was modeled by a $p(6 \times 2)$ geometry with a slab thickness of 4 layers separated by 10 \AA vacuum. This amounts to 192 O and 96 Ti ions. When needed, 4-layer $p(4 \times 2)$ or 5-layer $p(3 \times 2)$ surface were also used. The bottom layer was fixed at bulk positions and terminated by pseudohydrogen [38] atoms. Positions of Ti^{3+} were controlled by initial structure of the relaxation as described in previous section. The charge state of V_O was controlled by varying number of total valence electrons in the system. Charge was compensated by a neutralizing uniform background charge. The plane wave cut-off energy was 450 eV and the core-valence interaction was described by the projector augmented wave approach (PAW). The Brillouin zone was sampled by Γ point. Lattice parameters of $a = 4.60 \text{ \AA}$ and $c = 2.95 \text{ \AA}$ were used. During relaxation, Hellmann-Feynman forces were reduced below 0.02 eV/\AA . STM images are drawn by Hamann-Tersoff approach. [92, 93]

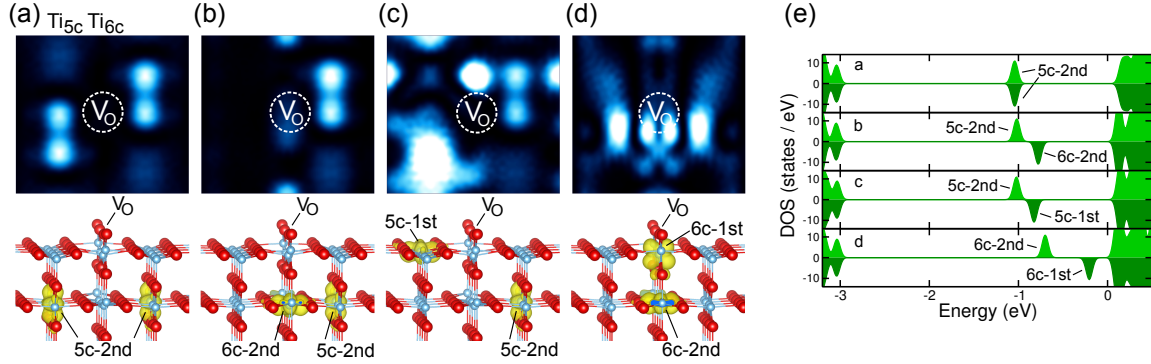


Figure 5.1 (a)-(d) Charge density (top) and corresponding filled state STM (bottom). Neutral V_O with (a) two Ti_{5c-2nd} (b) Ti_{6c-2nd} and Ti_{5c-2nd} (c) Ti_{5c-1st} and Ti_{5c-2nd} (d) Ti_{6c-1st} and Ti_{6c-2nd} . Isosurface level = $0.005 \text{ e}/\text{\AA}^3$. Only gap-states are imaged in STM. A tip distance is about 3 \AA from the surface. (e) corresponding density of states. Total energies of each configurations are found at Table. 5.1 Visualisations were made using VESTA. [3]

Table 5.1 Ti^{3+} positions in neutral V_O $p(4 \times 2)$ 4-layer cell and its total energy.

Position of Ti^{3+}	Energy (eV)
$Ti_{5c-2nd} - Ti_{5c-2nd}$	0
$Ti_{5c-2nd} - Ti_{6c-2nd}$	0.25
$Ti_{5c-1st} - Ti_{5c-2nd}$	0.25
$Ti_{6c-1st} - Ti_{6c-2nd}$	1.05

5.3 Results and discussion

5.3.1 Ti^{3+} defects at Ti_{5c-2nd}

Ti $3d$ state can localize at almost any Ti sites in the surface. In this section, it is shown that Ti $3d$ state at Ti_{5c-2nd} site can only explain the common features of filled state STM. To do that, the positions of Ti^{3+} defects in the slab was varied and STM images for each configurations are produced. Due to a computational cost, a 4-layer $p(4 \times 2)$ surface slab with one neutral V_O was adopted. Four stable Ti sites in the cell, Ti_{5c-1st} , Ti_{5c-2nd} , Ti_{6c-1st} and Ti_{6c-2nd} were chosen for the localization sites. Since a Ti $3d$ state is localized one and a $p(4 \times 2)$ surface is big enough to avoid significant overlap with Ti^{3+} itself, the conclusion made here is valid even in a larger cell. Ti_{5c-1st} and Ti_{6c-1st} indicate a five-fold coordinated Ti and six-fold coordinated Ti at 1st layer respectively. Ti_{5c-2nd} and Ti_{6c-2nd} denote Ti site below

Ti_{5c-1st} and Ti_{6c-2nd} , respectively. Out of that, four possible configurations of Ti^{3+} localization as show in Figure 5.1a-d were calculated. On top panel the STM image of corresponding charge density is shown. Interestingly, configurations other than Figure 5.1a ($\text{Ti}_{5c-2nd} - \text{Ti}_{5c-2nd}$) has bright feature on Ti_{6c} row which does not agree with experiments.

Calculated electronic density of states are shown in Figure 5.1e. It is seen that Ti^{3+} at different positions lead to gap state with different positions in DOS. In other words, they can be distinguished from each other by peak positions in DOS. This can be hold in the binding energy of this state, which is observed in XPS, UPS and EELS. In those experiments the gap state has a binding energy of about 1 eV. This corresponds to 5c-2nd which is the furthest away from conduction band edge, being about 1 eV below.

In Table 5.1, the relative total energy of these systems is shown. It is clear that two 5c-2nd is the most stable configuration. Based on the STM, DOS and the stability of the Ti^{3+} above, it is concluded that Ti^{3+} defects only at Ti_{5c-2nd} are responsible for the filled state STM image.

5.3.2 A typical STM image at 78 K

A filled state image taken at 78 K with a bias voltage of -1.1 V was reported by Minato *et al.* [2] as presented in Figure 5.2(a). In the image, Ti_{5c} row appear bright and Ti_{6c} row appear dark. This is in fact a common feature shared by all recent filled state images. [2, 24, 25] They reported a four-blob structure around a V_O as a typical structure. Four bright blobs are diagonally located on Ti_{5c} row adjacent to V_O forming a rectangle centered at V_O . Each blob has an extension to (001) direction having the brightest feature on second and third nearest Ti sites to V_O in the row. The V_O coverage was estimated to be about 6 %ML (monolayer) from their empty state image, where 1 ML is defined as the density of (1×1) unit cells, $5.2 \times 10^{14} \text{ cm}^{-2}$. The features are reproduced very well by the calculation as shown in Figure 5.2(b). An -2 charged V_O in $p(6 \times 2)$ surface cell was calculated. One V_O in $p(6 \times 2)$ cell corresponds to a V_O coverage of 8.3 %ML, which is close enough to the experiment. Since one V_O introduces two excess electrons, this system has four excess electrons per V_O in total. These electrons are localized at Ti_{5c-2nd} sites appearing as band gap states 1 eV below the conduction band edge (CB-edge) in density of states (DOS) as shown in Figure 5.3(a). They form four polaronic Ti 3d

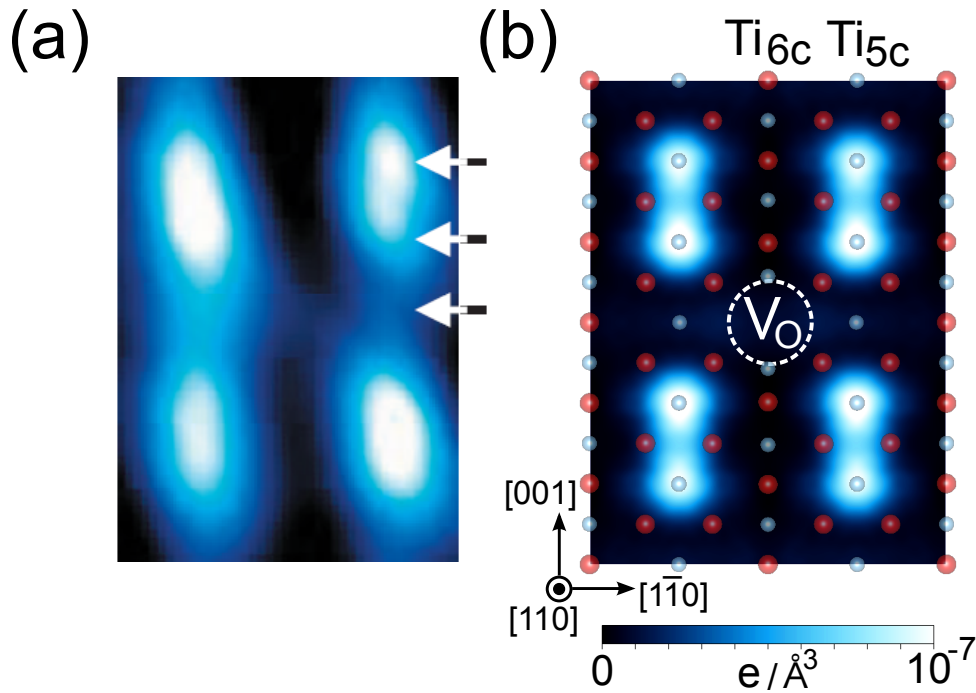


Figure 5.2 Filled state STM images of reduced TiO_2 (110). (a) Image reported by Minato *et al.* [2] Arrows indicate a position of Ti_{5c} species. (b) This work. In the calculation, band gap states appeared at about 1 eV below CB-edge in the density of states (Figure 5.3(a)) are imaged, and a tip-sample distance is about 3 Å. Red sphere: Ti, blue sphere: O. Visualisations were made using VESTA. [3] (a) Reprinted with permission from ref 2. Copyright 2009, AIP Publishing LLC.

states as can be seen in the charge density of these states shown in Figure 5.3(b). In Figure 5.3(c), a side-view of the charge density of one Ti_{5c} row is shown. From this figure it is evident that two tails of each Ti^{3+} contribute to one blob in the STM image. In Figure 5.3(d) a top-view of the charge density with 2nd-layer atoms is shown. It is clear that each Ti^{3+} occupy three Ti_{5c-2nd} sites and the sites are effectively fully occupied in this configuration. A possibility of having Ti^{3+} at different Ti sites were excluded in separate calculations with a 4-layer $p(4 \times 2)$ cell as shown in previous section. When Ti^{3+} is at Ti sites in 1st or 2nd layer other than Ti_{5c-2nd} , it produces bright features in Ti_{6c} row which is not observed in experiments. Also, the total energy of those configurations is at least 0.25 eV higher than the most stable case. This is in accord with previous works. [27,30]

Up to this point, it has been shown that a bright blob around a V_O can be interpreted by a Ti^{3+} at Ti_{5c-2nd} . Ti^{3+} are not expected to hop to Ti sites other than Ti_{5c-2nd} at low temperature due to rather high total energy differences as discussed

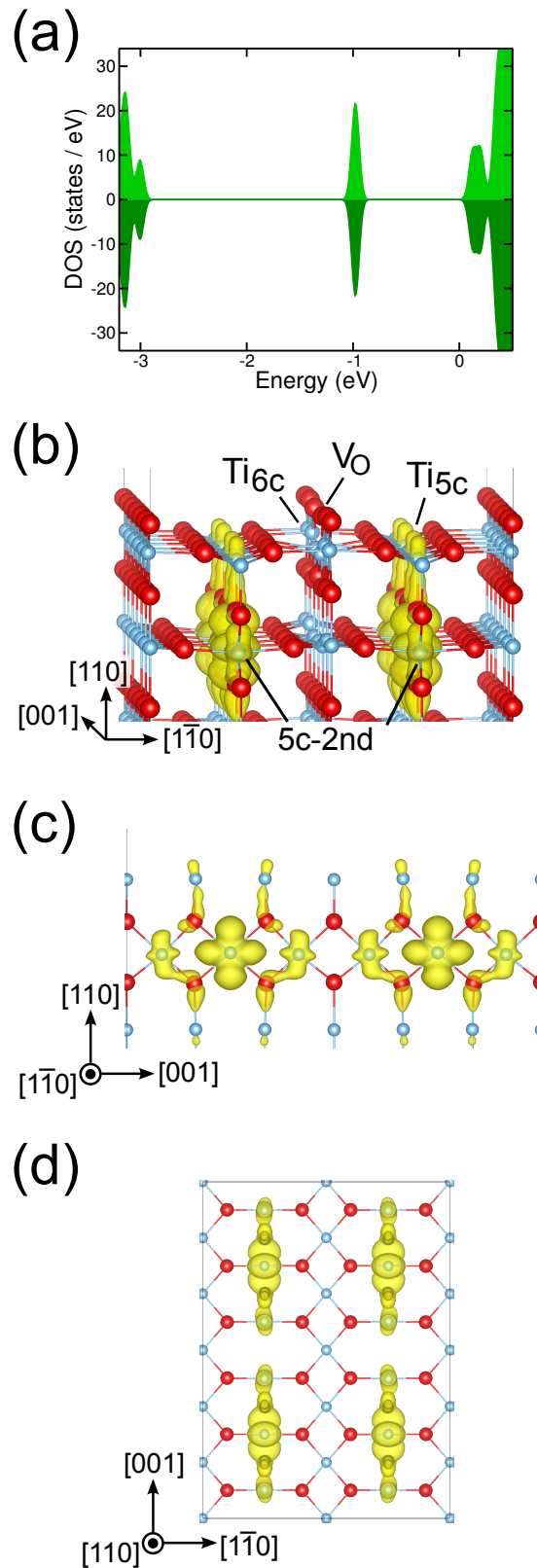


Figure 5.3 Electronic structure of -2 charged V_O in a 4-layer $p(6 \times 2)$ surface. (a) density of states and (b) charge density of band gap states. (c) Side-view of a one Ti_{5c} row and (d) top-view of 2nd-layer of the charge density. Only the gap states about 1 eV below CB-edge are imaged. Fermi level is aligned at conduction band edge. Red sphere: Ti, blue sphere: O. Isosurface level = $0.0014 \text{ e}/\text{\AA}^3$.

Table 5.2 Ti^{3+} positions in Ti_{5c-2nd} in neutral V_O $p(4 \times 2)$ 4-layer cell and its total energy. Another Ti^{3+} is localized at position 2 in another Ti_{5c} row

Position of Ti^{3+} in Ti_{5c-2nd}	distance from V_O (\AA)	distance from another Ti^{3+} (\AA)	Energy (meV)
1	7.2	7.1	3
2	5.9	6.5	10
3	5.9	7.1	6
4	7.2	8.8	0

above. However, whether the image is a weighted average of moving polarons along a Ti_{5c-2nd} row or immobile polarons at Ti_{5c-2nd} sites remains unclear. In former case a probability of finding a Ti^{3+} at a certain Ti_{5c-2nd} site within a scanning time, which is reported to be about 100 nm/s [94], is high due to a particular potential structure, and in the latter case a Ti^{3+} does not hop to other Ti_{5c-2nd} sites within the scanning time for some reasons.

The former case is excluded by a set of calculations of 4-layer $p(4 \times 2)$ surface with a neutral V_O in which the position of a Ti^{3+} is varied within Ti_{5c-2nd} row. This surface is adopted because $p(4 \times 2)$ surface has eight Ti_{5c-2nd} sites which is sufficiently large to accommodate two Ti^{3+} arose from a V_O while avoiding a self-overlap of a Ti^{3+} which results in an unnecessary energy increase. The charge density of band gap states and its top-view of the 2nd-layer are shown in Figure 5.4(a) and 5.4(b), respectively. Calculated sites for Ti^{3+} localization in a Ti_{5c-2nd} row are presented in Figure 5.4, numbered from 1 to 4. They are all different sites having various distance from V_O or another Ti^{3+} localized at another Ti_{5c-2nd} row as shown in Table 5.2. The relative total energy of these configurations is shown in the table. Clearly, they are almost the same in energy. Although energy barriers were not calculated in this work, the hopping is reported to be easy in (001) direction in first principles MD. [25, 51] These results suggest that there is no particular potential structure around a V_O in Ti_{5c-2nd} row which traps Ti^{3+} at a certain position. Thus, it is concluded that the latter is the case; Ti^{3+} are immobile at 78 K for some reasons. Probably, it is because the Ti_{5c-2nd} row is effectively fully occupied by Ti^{3+} and they are hard to move. As discussed below, this “effectively fully occupied Ti_{5c-2nd} sites” can be a prerequisite to form shallow donor states.

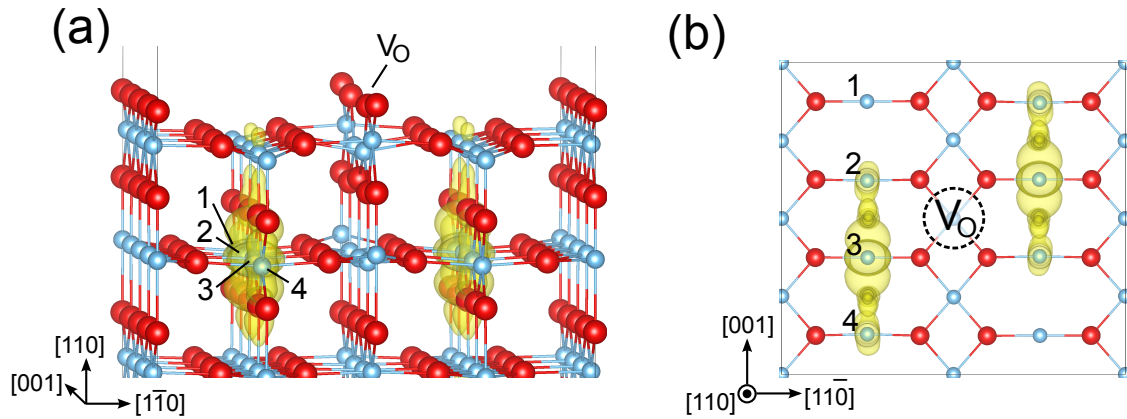


Figure 5.4 Charge density of the Ti^{3+} at $\text{Ti}_{5\text{c-}2\text{nd}}$ sites in a 4-layer $p(4 \times 2)$ surface with a neutral V_O . (a) whole view and (b) top-view of the 2nd-layer. Numbers denote localization sites of Ti^{3+} studied. Site dependence of relative total energies is found in Table 5.2. Isosurface level = $0.0014 \text{ e}/\text{\AA}^3$.

5.3.3 Formation of shallow donor states

Reduced rutile TiO_2 has both shallow donor states just below CB-edge and band gap states about 1 eV below CB-edge observed in PES [10] and transport properties studies, [95] and this fact is a basis of STM interpretations. [2, 11, 25] Those states are formed by excess electrons introduced by oxygen deficiency. In calculations, the effect of excess electrons can be incorporated by either introducing donor defects such as oxygen vacancies and Ti interstitials from, or adding extra electrons to a defect-free structure. [26, 31]. In hybrid DFT, however, excess electrons are trapped by localized gap states which are more stable, and a condition under which shallow donor states are formed is not known in general. There is an attempt by Janotti *et al.* to account for the coexistence of the localized gap states and the delocalized shallow donor states in hybrid DFT calculations. [31] By studying a 216-atom bulk supercell with one extra electron, they showed that both states can be stabilized, the gap states being lower in energy. It was also shown that there is an energy barrier between those states which prevents electrons in shallow donor states fall into the gap states which are more stable at low temperature. The energy barrier was determined by a set of self-consistent total energy calculations of various lattice configurations which are interpolated between the localized and delocalized electron structure. Inspired by their work, the same approach is taken to obtain a crude understanding of the nature of excess electrons, under which conditions the

coexistence of localized and delocalized states becomes possible, in a surface region. A stability of the localized gap states and delocalized states of an extra electron is studied in a 5-layer $p(3 \times 2)$ defect-free surface. The role of the “effectively fully occupied Ti_{5c-2nd} sites” in this respect is of a particular interest since this might be observed in the typical STM image as discussed above. To investigate that, two systems are studied. One is a neutral surface with an extra electron, and the other is a surface with three extra electrons, two of them being localized at Ti_{5c-2nd} sites which corresponds to the case of the “effectively fully occupied Ti_{5c-2nd} sites”.

For the one-extra-electron case, the extra electron localized at Ti_{5c-2nd} site corresponds to the localized case as shown in Figure 5.5(a). The delocalized structure was obtained by adding an electron to a defect-free relaxed surface while keeping the lattice structure, which is presented in Figure 5.5(b). For the three-extra-electron case, the localized structure has Ti_{5c-2nd} sites effectively fully occupied by two electrons and another electron is localized at a Ti_{5c-4th} site as shown in Figure 5.6(a). In the previous section, it was shown that the lowest unoccupied state of the defect-free surface has a main contribution from Ti_{5c-2nd} sites and this was the reason for Ti_{5c-2nd} being the most stable position for the localization. In fact, the lowest unoccupied state had the second biggest contribution from Ti_{5c-4th} sites in the study. This is the reason why the Ti_{5c-4th} site is selected as the third localization site. The delocalized structure is shown in Figure 5.6(b). It was determined through the following procedure. First, two electrons are added to a defect-free surface and stabilized at Ti_{5c-2nd} sites. Then, another electron was added while keeping the lattice structure. Finally, the system was relaxed. It is worth noting that the last procedure could not be applied to the one-extra-electron case because the system prefers to have localized structure when relaxed, which indicates the instability of the delocalized structure in the one-extra-electron system.

The self-consistent total energy of the linearly interpolated structure between the localized (Figure 5.5(a)) and the delocalized (Figure 5.5(b)) states for the one-extra-electron system is presented in Figure 5.5(c). It is clear that there is no barrier between the two states and the energy difference is about 300 meV. This suggests that excess electrons favor to form localized states rather than shallow donor states if Ti_{5c-2nd} sites are empty. For the three-extra-electron case, the self-consistent total energy of the interpolated structure between the two states is presented in Figure 5.6(c). In contrast to the one-extra-electron case, there is a barrier between

two states and the energy difference is about 50 meV. This suggests that under this condition excess electrons conducted in the form of delocalized states can remain in those states at low temperature, thus the coexistence of localized and delocalized states is possible. The DOS of two states for the three-extra-electron case is shown in Figure 5.6(d). It is clearly seen that in delocalized configuration, there is a shallow donor state just below CB-edge.

From the argument above, it is concluded that when Ti_{5c-2nd} sites are effectively fully occupied the coexistence of gap states and shallow donor states is possible. Most probably this condition is met in the typical STM image, which leads to immobile polarons at Ti_{5c-2nd} sites appear as blobs rather than lines. Given that one V_O introduces two excess electrons into Ti_{5c-2nd} sites, under the V_O coverage of 6 %ML, more than two excess electrons per V_O should be provided from other donor defects in order to effectively fully occupy the Ti_{5c-2nd} sites. The donor defects will be Ti interstitials as discussed below.

5.3.4 78 K image under high-reduced condition

There is another filled state image taken at 78 K with a bias voltage of -1.4 V by Setvin *et al.* [25] From their image the V_O coverage was estimated to be about 15 %ML. It is further denoted as the high-reduced surface to compare with Minato *et al.*'s low-reduced one, following experimental notations. [18] Even though this surface contains apparently more V_O than low-reduced one, both STM images look quite similar. It is natural to interpret each blob as a Ti^{3+} at a Ti_{5c-2nd} site. Only the difference is positions of blobs relative to V_O . In the high-reduced case some blobs occupy nearest-neighbor Ti site to V_O . This can be understood by a high V_O coverage in this surface. There are so many V_O that each V_O competes to form a typical "rectangle", which results in a compromised structure. As discussed above and shown in Figure 5.4 and Table 5.2, Ti^{3+} has almost the same energy at any Ti_{5c-2nd} sites. So having such a compromised structure is expected not to cost much energy.

An important observation is that both in low-reduced and high-reduced surface Ti_{5c-2nd} sites are effectively fully occupied by Ti^{3+} at 78 K. This is probably due to the ionization of subsurface Ti interstitials. Yagi *et al.* reported that they are ionized at about 4 K in their transport properties study. [95] Thus, it is inferred that regardless of V_O coverage, Ti_{5c-2nd} sites are effectively fully occupied by excess

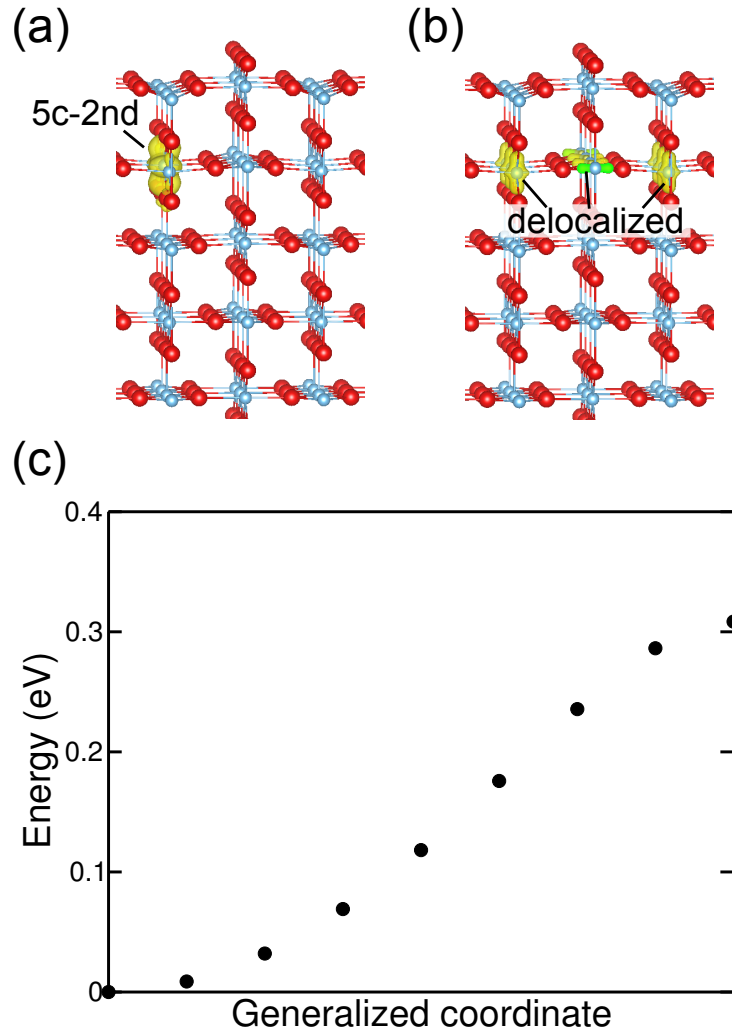


Figure 5.5 One extra electron added to a defect-free 5-layer $p(3 \times 2)$ surface. (a) Charge density of the extra electron localized at Ti_{5c-2nd} and (b) in delocalized form. (c) Self-consistent total energies of various configurations which are interpolated between localized (left) and delocalized (right) configuration. Isosurface level = $0.005 \text{ e}/\text{\AA}^3$.

electrons supplied by both V_O and Ti interstitials at this temperature. Note that there is an upper limit in the V_O coverage, which is 16.7 %ML. At this coverage, Ti_{5c-2nd} sites are effectively fully occupied only by excess electrons associated to V_O . Beyond that, the system has to accommodate excess electrons introduced by V_O at different sites, which costs more energy. This mechanism seems to be behind the fact that maximum V_O coverage reported in the literatures are found around 15 %ML which is close to 16.7 %ML.

In addition to the -1.4 V image, Setvin *et al.* reported a -0.6 V image in which a

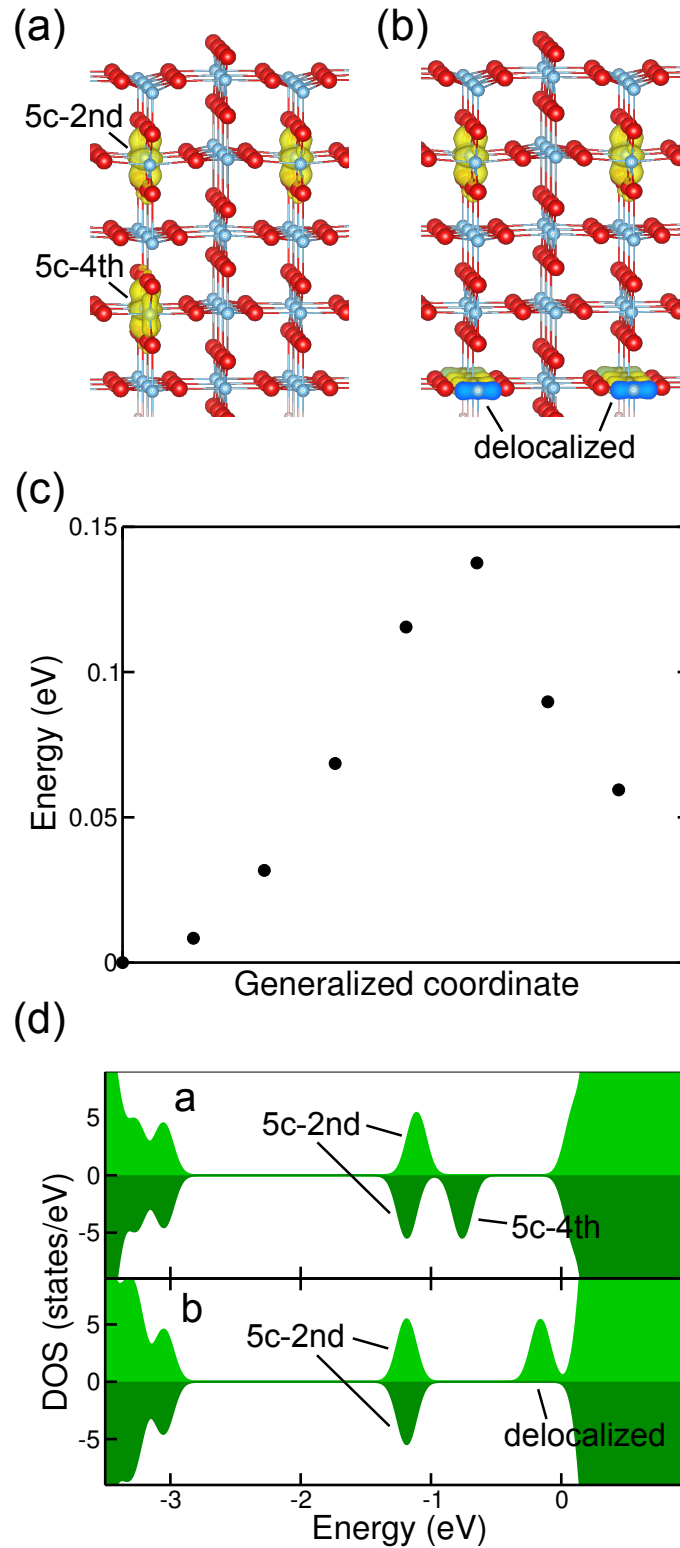


Figure 5.6 Three extra electron added to a defect-free 5-layer $p(3 \times 2)$ surface. (a) Charge density of the extra electrons localized at Ti_{5c-2nd} and Ti_{5c-4th} sites. (b) Charge density of extra electrons, two of them being localized at Ti_{5c-2nd} sites and one in delocalized form. (c) Self-consistent total energies of various configurations which are interpolated between localized (left) and delocalized (right) configuration. (d) Density of states of the localized (top-panel) and delocalized (bottom-panel) configuration. Isosurface level = $0.005 \text{ e}/\text{\AA}^3$.

bright spot is seen on each Ti_{5c} site. This is substantially different from the -1.4 V image. It might be because the gap states cannot be observed at -0.6 V. They reported that the tip-sample distance is 0.3 Å closer than the one used in -1.4 V image. It is speculated that they observed the delocalized shallow donor states which are located in the subsurface region such as shown in Figure 5.6(b).

5.3.5 5 K image

A filled state STM image taken at 5 K with a bias voltage of -2 V is reported by Papageorgiou *et al.* [24] From their image the V_O coverage was estimated to be about 10 %ML. Note that their image includes a small number of surface bridging OH defects. Two surface OH defects were counted as one V_O , since an OH defect is known to introduce one excess electron. [22, 26] The image consists of very bright blobs as well as broad and vague lines on Ti_{5c} row, which is different from 78 K images. Setvin *et al.* observed a complete absence of electric conductivity at temperature below 20 K. Yagi *et al.* reported that a small polaron model should be taken into account at temperature above 50 K. [95] As discussed above, they also reported the ionization of Ti interstitials take place at temperature above about 4 K. From these facts, it was assumed that polarons are frozen at Ti_{5c-2nd} sites and no excess electrons are provided to Ti_{5c-2nd} sites from Ti interstitials at this temperature. In other words, V_O is expected to be charge neutral. Based on this view, a calculation of a $p(6 \times 2)$ surface with a neutral V_O was conducted. The features were successfully reproduced as shown in Figure 5.7(a). In order to reproduce the vague line, the contrast was adjusted. The corresponding charge density of the gap states and the DOS are presented in Figure 5.7(b) and 5.7(c), respectively. It is evident from Figure 5.7(b) that the bright blob corresponds to a Ti^{3+} at a Ti_{5c-2nd} site. This is important because it allows one to count the number of excess electrons at the surface. By comparing that number with the number of surface donor defects one can check whether the assumption, V_O is charge neutral, was correct or not. The charge state of V_O was estimated to be almost neutral, being consistent with the assumption. Thus, it is inferred that at this temperature, excess electrons from Ti interstitials are not activated and consequently V_O are neutral.

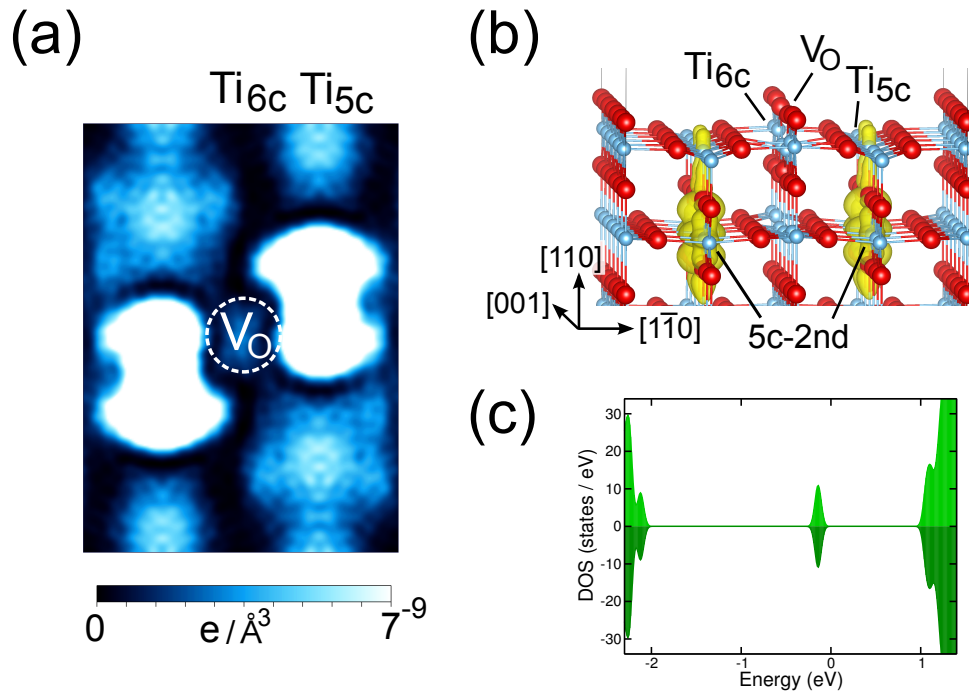


Figure 5.7 Electronic structure of a 4-layer $p(6 \times 2)$ surface with a neutral V_O . (a) Filled state STM image and (b) corresponding charge density of band gap states about 1 eV below CB-edge. (c) Density of states. A tip-sample distance is about 3 Å. Isosurface level = $0.0014 e/\text{\AA}^3$.

5.3.6 Temperature dependency of V_O reactivity behind experimental complications

As reviewed by Pang *et al.*, [96] despite previous works, oxygen chemisorption on this surface at low temperature is still complicated. This is clearly seen in recent discussion on a saturation coverage of O_2 molecules. While Kimmel and Petrik conclude that the saturation coverage of O_2 depends almost linearly on V_O coverage, [91] Lira *et al.* report that it highly depends on the sample preparation history. [16] The former view supports the oxygen-vacancy model in which the reactivity of reduced surfaces is determined only by V_O and their accompanying electrons, whereas the latter propose the view in which Ti interstitials dominate the surface reactivity. [96] In addition, the reported saturation coverage of O_2 differ widely under the typical V_O coverage of 8 %ML. While Henderson *et al.* suggest that three O_2 molecules adsorb per one V_O , [86] Kimmel and Petrik conclude about two O_2 molecules per V_O , [91] and Lira *et al.* report that five O_2 molecules are adsorbed per V_O in one sample. [16]

A key to understand these discrepancies lies in an adsorption temperature (T_{ad}) of O_2 molecules. While Kimmel and Petrik conducted O_2 exposure at 25 K, Henderson *et al.* and Lira *et al.* did it at 120-130 K. It was shown that at 5 K the number of excess electrons around V_O is kept constant at two up to the V_O coverage of 16.7 %ML. This explains the linear behaviour of the O_2 saturation coverage reported by Kimmel and Petrik under $T_{ad} = 25$ K. It should be noted that probably a part of Ti interstitials are ionized even at this temperature as suggested by Yagi *et al.* [95] This is in fact seen in the subtle non-linear behaviour of their result in which the saturation coverage of O_2 decreases from 2.35 to 2.07 as V_O coverage grows from 8 %ML to 14.5 %ML. V_O seem to compete limited number of excess electrons supplied from partially ionized Ti interstitials. Although they carefully increased V_O coverage by an electron-irradiation instead of the sputter-and-anneal cycles in order not to increase Ti interstitials in subsurface region, it is inferred that the effect of Ti interstitials formed before the electron-irradiation is not negligible even at this temperature.

In contrast, it was shown that Ti_{5c-2nd} sites are effectively fully occupied independent of V_O coverage at 78 K, probably because subsurface Ti interstitials provide excess electrons to Ti_{5c-2nd} sites at this temperature. After Ti_{5c-2nd} sites are effectively fully occupied, those excess electrons presumably form Ti^{3+} in deeper layer such as at Ti_{5c-4th} shown in Figure 5.6(b). They form band gap states as seen in Figure 5.6(d) which can be observed as Ti 3d states in PES and EELS. When the Ti_{5c-2nd} sites become empty, those subsurface Ti^{3+} probably diffuse to the Ti_{5c-2nd} sites since they are lower in energy. This means that the number of excess electrons depends on the density of Ti interstitials near surface region, which is determined by the preparation history. [16] Although $T_{ad} = 125$ K is slightly higher than 78 K, this mechanism can explain the preparation history dependence of the O_2 saturation coverage reported by Lira *et al.* , and consequently accounts for the big difference between Lira *et al.* and Henderson *et al.*

In short, the oxygen-vacancy model seems to be valid at very low temperature. However, from the discussion above, it can be said that the model needs to be modified at temperature above at least 78 K. Above that temperature, V_O reactivity depends on the density of Ti interstitials in subsurface region which is determined by the sample preparation history. The exact temperatures at which the excess electrons belong to Ti interstitials become active, and whether this interpretation

is valid even at room temperature remains unclear. It would be illuminating to take filled state STM images at various temperatures, especially from about 5 K to 130 K as well as at room temperature.

5.4 Summary

Filled state STM images taken at 5 K and 78 K were reproduced by calculations based on density functional theory and screened hybrid functionals. Total energy comparisons between localized and delocalized states in a defect-free surface suggested that having an effectively occupied $\text{Ti}_{5\text{c}-2\text{nd}}$ sites is a prerequisite for a formation of shallow donor states. It was concluded that $\text{Ti}_{5\text{c}-2\text{nd}}$ sites are effectively fully occupied independent of V_{O} coverage up to a saturation coverage of 16.7 %ML at 78 K. This can be explained by a supply of excess electrons to $\text{Ti}_{5\text{c}-2\text{nd}}$ sites from Ti interstitials in subsurface region. In contrast, $\text{Ti}_{5\text{c}-2\text{nd}}$ sites are filled only by excess electrons of V_{O} at 5 K. This mechanism can explain a seemingly contradicting reports on O_2 saturation coverage at low temperature. Finally, it was proposed that the oxygen-vacancy model needs to be modified at temperature above 78 K. Above that temperature, excess electrons belong to subsurface Ti interstitials are expected to take part in the surface reaction via $\text{Ti}_{5\text{c}-2\text{nd}}$ sites.

Chapter 6

Conclusion

In order to broaden the atomic-scale understanding of the surface chemistry of TiO_2 , DFT calculations on reduced rutile TiO_2 (110) surface were carried out. The primary interest of this study was in the nature of excess electrons around the bridging oxygen vacancy (V_{O}), which play important roles in surface reactions. To properly describe the localizing nature of excess electrons in DFT, a method called hybrid functional (HSE06) was adopted.

A systematic comparison between DFT+U and HSE06 methods reveal following. One V_{O} introduces two excess electrons. Each excess electron localizes at a Ti site forming a Ti^{3+} state, or a polaron state in the band gap, 1 eV below the conduction band edge. The spatial extent of each polaron is about (6.5×7) Å along the basal plane of the Ti centered octahedron. The total energy of the system depends on the position of polarons. The polaron is the most stable at 2nd layer below $\text{Ti}_{5\text{c}}$ ($\text{Ti}_{5\text{c}-2\text{nd}}$). It is explained in terms of spatial symmetry breaking, where the defect free unoccupied lowest state becomes localized on only two subsurface Ti sites. In the (4×2) cell, DFT+U ($U=4.2$ eV) and HSE06 give more or less identical results except that latter describes the band gap much better.

From the total energy analysis, it is concluded that a bipolaron is stable only in close proximity of an oxygen vacancy. The energy contribution of lattice deformations is negligible compared to the electrostatic interaction.

Based on these understandings, filled state STM images taken at 5 K and 78 K were reproduced. Bright blobs were shown to be excess electrons localized at $\text{Ti}_{5\text{c}-2\text{nd}}$ sites. Total energy comparisons between localized and delocalized states in a defect-free surface suggested that having an effectively occupied $\text{Ti}_{5\text{c}-2\text{nd}}$ sites is a prerequisite for a formation of shallow donor states. It was concluded that $\text{Ti}_{5\text{c}-2\text{nd}}$ sites are effectively fully occupied independent of V_{O} coverage up to a saturation coverage of

16.7 %ML at 78 K. This can be explained by a supply of excess electrons to $\text{Ti}_{5\text{c}-2\text{nd}}$ sites from Ti interstitials in subsurface region. In contrast, $\text{Ti}_{5\text{c}-2\text{nd}}$ sites are filled only by excess electrons of V_{O} at 5 K. This mechanism can explain a seemingly contradicting reports on O_2 saturation coverage at low temperature. Finally, it was proposed that the oxygen-vacancy model needs to be modified at temperature above 78 K. Above that temperature, excess electrons belong to subsurface Ti interstitials are expected to take part in the surface reaction via $\text{Ti}_{5\text{c}-2\text{nd}}$ sites.

From another perspective, this work opens a new way of surface chemistry in which both DFT and STM are utilized to directly observe reactive defects such as Ti^{3+} states, which play crucial roles in charge transfer to adsorbed molecules thus directly affect the efficiency of photocatalysis, on the surface of metal oxides.

Future perspectives

The results presented in this work provides a firm starting point for the recent issues on O_2 chemisorption such as the chemical state of O_2 , dissociation channel or saturation coverage. In particular, a study on the relative stability of Ti^{3+} which is introduced by a Ti interstitail deeper in the surface will be interesting. From experimental side, it would be illuminating to take filled state STM images at various temperatures, especially from about 5 K to 130 K as well as at room temperature. The view presented in this work can be extended to the discussion of the role of oxygen vacancy on other reactions such as the low temperature CO oxidation on Au nanoparticle-loaded TiO_2 .

Since the capability of STM and DFT of describing a spacial distribution of Ti^{3+} species are verified in the thesis, properties of metal oxides can be understood by using this information. The difference in photocatalytic performance between rutile and anatase should be revisited in this respect. Also, the difference in the behaviour of active species at sufrace can help understand the functionality of interfaces between different surfaces or even different materials. Since this TiO_2 is d^0 configuration, the result of this thesis is expected to be valid especially for other d^0 and f^0 system such as V_2O_5 , MoO_3 , or CeO_2 .

References

- [1] Wikipedia, “Titanium dioxide — Wikipedia, The Free Encyclopedia,” 2015. [Online; accessed 27-June-2015].
- [2] T. Minato, Y. Sainoo, Y. Kim, H. S. Kato, K.-i. Aika, M. Kawai, J. Zhao, H. Petek, T. Huang, W. He, B. Wang, Z. Wang, Y. Zhao, J. Yang, and J. G. Hou, “The electronic structure of oxygen atom vacancy and hydroxyl impurity defects on titanium dioxide (110) surface,” *The Journal of Chemical Physics*, vol. 130, no. 12, p. 124502, 2009.
- [3] K. Momma and F. Izumi, “VESTA 3 for three-dimensional visualization of crystal, volumetric and morphology data,” *Journal of Applied Crystallography*, vol. 44, no. 6, p. 1272, 2011.
- [4] A. Fujishima, K. Honda, and S. Kikuchi, “Photosensitized electrolytic oxidation on semiconducting n-type TiO₂ electrode (in Japanese),” *Journal of Chemical Society of Japan (Kogyo Kagaku Zasshi)*, no. 72, p. 108, 1969.
- [5] D. B. Strukov, G. S. Snider, D. R. Stewart, and R. S. Williams, “The missing memristor found,” *Nature*, vol. 453, no. 7191, pp. 80–83, 2008.
- [6] G. Binnig, H. Rohrer, C. Gerber, and E. Weibel, “Surface studies by scanning tunneling microscopy,” *Physical Review Letters*, vol. 49, no. 1, p. 57, 1982.
- [7] V. Fock *Z. Physik*, vol. 61, p. 126, 1930.
- [8] P. Hohenberg and W. Kohn, “Inhomogeneous electron gas,” *Physical Review*, vol. 136, no. 3B, p. B864, 1964.
- [9] W. Kohn and L. J. Sham, “Self-consistent equations including exchange and correlation effects,” *Physical Review*, vol. 140, no. 4A, p. A1133, 1965.
- [10] V. E. Henrich, G. Dresselhaus, and H. Zeiger, “Observation of two-dimensional phases associated with defect states on the surface of TiO₂,” *Physical Review Letters*, vol. 36, no. 22, p. 1335, 1976.
- [11] U. Diebold, J. F. Anderson, K.-O. Ng, and D. Vanderbilt, “Evidence for the tunneling site on transition-metal oxides: TiO₂ (110),” *Physical Review Letters*,

- vol. 77, no. 7, p. 1322, 1996.
- [12] Y. Sakai and S. Ehara, "Scanning tunneling microscopy/spectroscopy study of point defects on TiO_2 (110)-(1 \times 1) surface," *Japanese Journal of Applied Physics*, vol. 40, no. 7B, p. L773, 2001.
- [13] M. Batzill, K. Katsiev, D. J. Gaspar, and U. Diebold, "Variations of the local electronic surface properties of TiO_2 (110) induced by intrinsic and extrinsic defects," *Physical Review B*, vol. 66, no. 23, p. 235401, 2002.
- [14] M. A. Henderson, "A surface perspective on self-diffusion in rutile TiO_2 ," *Surface Science*, vol. 419, no. 2, pp. 174–187, 1999.
- [15] S. Wendt, P. T. Sprunger, E. Lira, G. K. Madsen, Z. Li, J. Ø. Hansen, J. Matthiesen, A. Blekinge-Rasmussen, E. Lægsgaard, B. Hammer, and F. Besenbacher, "The role of interstitial sites in the $\text{Ti}3d$ defect state in the band gap of titania," *Science*, vol. 320, no. 5884, p. 1755, 2008.
- [16] E. Lira, J. Ø. Hansen, P. Huo, R. Bechstein, P. Galliker, E. Lægsgaard, B. Hammer, S. Wendt, and F. Besenbacher, "Dissociative and molecular oxygen chemisorption channels on reduced rutile TiO_2 (110): an STM and TPD study," *Surface Science*, vol. 604, no. 21, p. 1945, 2010.
- [17] E. Lira, S. Wendt, P. Huo, J. Ø. Hansen, R. Streber, S. Porsgaard, Y. Wei, R. Bechstein, E. Lægsgaard, and F. Besenbacher, "The importance of bulk Ti^{3+} defects in the oxygen chemistry on titania surfaces," *Journal of the American Chemical Society*, vol. 133, no. 17, p. 6529, 2011.
- [18] E. Lira, P. Huo, J. Ø. Hansen, F. Rieboldt, R. Bechstein, Y. Wei, R. Streber, S. Porsgaard, Z. Li, E. Lægsgaard, S. Wendt, and F. Besenbacher, "Effects of the crystal reduction state on the interaction of oxygen with rutile TiO_2 (110)," *Catalysis Today*, vol. 182, no. 1, p. 25, 2012.
- [19] M. Nolan, S. Grigoleit, D. C. Sayle, S. C. Parker, and G. W. Watson, "Density functional theory studies of the structure and electronic structure of pure and defective low index surfaces of ceria," *Surface Science*, vol. 576, no. 1-3, p. 217, 2005.
- [20] D. O. Scanlon, A. Walsh, B. J. Morgan, and G. W. Watson, "An ab initio study of reduction of V_2O_5 through the formation of oxygen vacancies and Li intercalation," *Journal of Physical Chemistry C*, vol. 112, p. 9903, 2008.
- [21] R. Coquet and D. J. Willock, "The (010) surface of $\alpha\text{-MoO}_3$, a DFT+ U study," *Physical Chemistry Chemical Physics*, no. 7, p. 3819, 2005.

-
- [22] C. Di Valentin, G. Pacchioni, and A. Selloni, “Electronic structure of defect states in hydroxylated and reduced rutile TiO_2 (110) surfaces,” *Physical Review Letters*, vol. 97, no. 16, p. 166803, 2006.
- [23] B. J. Morgan and G. W. Watson, “A DFT+ U description of oxygen vacancies at the TiO_2 rutile (110) surface,” *Surface Science*, vol. 601, no. 21, p. 5034, 2007.
- [24] A. C. Papageorgiou, N. S. Beglitis, C. L. Pang, G. Teobaldi, G. Cabailh, Q. Chen, A. J. Fisher, W. A. Hofer, and G. Thornton, “Electron traps and their effect on the surface chemistry of TiO_2 (110),” *Proceedings of the National Academy of Sciences*, vol. 107, no. 6, p. 2391, 2010.
- [25] M. Setvin, C. Franchini, X. Hao, M. Schmid, A. Janotti, M. Kaltak, C. G. Van de Walle, G. Kresse, and U. Diebold, “Direct view at excess electrons in TiO_2 rutile and anatase,” *Physical Review Letters*, vol. 113, no. 8, p. 086402, 2014.
- [26] N. A. Deskins, R. Rousseau, and M. Dupuis, “Localized electronic states from surface hydroxyls and polarons in TiO_2 (110),” *The Journal of Physical Chemistry C*, vol. 113, no. 33, p. 14583, 2009.
- [27] N. A. Deskins, R. Rousseau, and M. Dupuis, “Distribution of Ti^{3+} surface sites in reduced TiO_2 ,” *The Journal of Physical Chemistry C*, vol. 115, no. 15, p. 7562, 2011.
- [28] E. Finazzi, C. Di Valentin, and G. Pacchioni, “Nature of ti interstitials in reduced bulk anatase and rutile tio_2 ,” *The Journal of Physical Chemistry C*, vol. 113, no. 9, pp. 3382–3385, 2009.
- [29] H.-Y. Lee, S. J. Clark, and J. Robertson, “Calculation of point defects in rutile tio_2 by the screened-exchange hybrid functional,” *Physical Review B*, vol. 86, no. 7, p. 075209, 2012.
- [30] S. Chrétien and H. Metiu, “Electronic structure of partially reduced rutile TiO_2 (110) surface: where are the unpaired electrons located?,” *The Journal of Physical Chemistry C*, vol. 115, no. 11, p. 4696, 2011.
- [31] A. Janotti, C. Franchini, J. Varley, G. Kresse, and C. Van de Walle, “Dual behavior of excess electrons in rutile TiO_2 ,” *Physica Status Solidi (RRL)*, vol. 7, no. 3, p. 199, 2013.
- [32] J. P. Perdew and Y. Wang, “Accurate and simple analytic representation of the electron-gas correlation energy,” *Physical Review B*, vol. 45, no. 23, p. 13244,

- 1992.
- [33] J. Perdew, K. Burke, and M. Ernzerhof, "Generalized gradient approximation made simple," *Physical Review Letters*, vol. 77, no. 18, p. 3865, 1996.
- [34] J. Heyd, G. E. Scuseria, and M. Ernzerhof, "Hybrid functionals based on a screened Coulomb potential," *The Journal of Chemical Physics*, vol. 118, no. 18, p. 8207, 2003.
- [35] A. V. Krukau, O. a. Vydrov, A. F. Izmaylov, and G. E. Scuseria, "Influence of the exchange screening parameter on the performance of screened hybrid functionals," *The Journal of Chemical Physics*, vol. 125, no. 22, p. 224106, 2006.
- [36] P. E. Blöchl, "Projector augmented-wave method," *Physical Review B*, vol. 50, no. 24, p. 17953, 1994.
- [37] G. Kresse and D. Joubert, "From ultrasoft pseudopotentials to the projector augmented-wave method," *Physical Review B*, vol. 59, no. 3, p. 1758, 1999.
- [38] K. Shiraishi, "A new slab model approach for electronic structure calculation of polar semiconductor surface," *Journal of The Physical Society of Japan*, vol. 59, p. 3455, 1990.
- [39] X. Chen and S. S. Mao, "Titanium dioxide nanomaterials: synthesis, properties, modifications, and applications," *Chemical Reviews*, vol. 107, no. 7, p. 2891, 2007.
- [40] A. Kudo and Y. Miseki, "Heterogeneous photocatalyst materials for water splitting," *Chemical Society Reviews*, vol. 38, no. 1, p. 253, 2009.
- [41] F. Labat, P. Baranek, and C. Adamo, "Structural and electronic properties of selected rutile and anatase TiO_2 surfaces: an ab initio investigation," *Journal of Chemical Theory and Computation*, vol. 4, no. 2, p. 341, 2008.
- [42] U. Diebold, "The surface science of titanium dioxide," *Surface Science Reports*, vol. 48, no. 5, p. 53, 2003.
- [43] G. Cabailh, X. Torrelles, R. Lindsay, O. Bikondoa, I. Joumard, J. Zegenhagen, and G. Thornton, "Geometric structure of TiO_2 (110)(1 \times 1): Achieving experimental consensus," *Physical Review B*, vol. 75, no. 24, p. 241403, 2007.
- [44] M. V. Ganduglia-Pirovano, A. Hofmann, and J. Sauer, "Oxygen vacancies in transition metal and rare earth oxides: Current state of understanding and remaining challenges," *Surface Science Reports*, vol. 62, no. 6, p. 219, 2007.
- [45] C. Yim, C. Pang, and G. Thornton, "Oxygen vacancy origin of the sur-

-
- face band-gap state of TiO_2 (110),” *Physical Review Letters*, vol. 104, no. 3, p. 036806, 2010.
- [46] S. Wendt, R. Bechstein, S. Porsgaard, E. Lira, J. O. Hansen, P. Huo, Z. Li, B. Hammer, and F. Besenbacher, “Comment on “Oxygen vacancy origin of the surface band-gap state of TiO_2 (110)”,” *Physical Review Letters*, vol. 104, p. 259703, Jun 2010.
- [47] C. M. Yim, C. L. Pang, and G. Thornton, “Yim, Pang, and Thornton reply:,” *Physical Review Letters*, vol. 104, p. 259704, Jun 2010.
- [48] C. L. Pang, R. Lindsay, and G. Thornton, “Chemical reactions on rutile TiO_2 (110),” *Chemical Society Reviews*, vol. 37, no. 10, p. 2328, 2008.
- [49] J.-M. Pan, B. Maschhoff, U. Diebold, and T. Madey, “Interaction of water, oxygen, and hydrogen with TiO_2 (110) surfaces having different defect densities,” *Journal of Vacuum Science & Technology A*, vol. 10, no. 4, p. 2470, 1992.
- [50] B. Kappes, W. Maddox, D. Acharya, P. Sutter, and C. Ciobanu, “Interactions of same-row oxygen vacancies on rutile TiO_2 (110),” *Physical Review B*, vol. 84, no. 16, p. 161402, 2011.
- [51] P. M. Kowalski, M. F. Camellone, N. N. Nair, B. Meyer, and D. Marx, “Charge localization dynamics induced by oxygen vacancies on the TiO_2 (110) surface,” *Physical Review Letters*, vol. 105, no. 14, p. 146405, 2010.
- [52] J. Hafner, “Ab-initio simulations of materials using VASP: Density-functional theory and beyond,” *Journal of Computational Chemistry*, vol. 29, no. 13, p. 2044, 2008.
- [53] P. Deák, B. Aradi, and T. Frauenheim, “Polaronic effects in TiO_2 calculated by the hse06 hybrid functional: Dopant passivation by carrier self-trapping,” *Physical Review B*, vol. 83, no. 15, p. 155207, 2011.
- [54] A. Janotti, J. Varley, P. Rinke, N. Umezawa, G. Kresse, and C. Van de Walle, “Hybrid functional studies of the oxygen vacancy in TiO_2 ,” *Physical Review B*, vol. 81, no. 8, p. 085212, 2010.
- [55] G. Kresse and J. Hafner, “Ab initio molecular dynamics for liquid metals,” *Physical Review B*, vol. 47, no. 1, p. 558, 1993.
- [56] G. Kresse and J. Furthmüller, “Efficient iterative schemes for ab initio total-energy calculations using a plane-wave basis set,” *Physical Review B*, vol. 54, no. 16, p. 11169, 1996.

- [57] M. Marsman, J. Paier, A. Stroppa, and G. Kresse, “Hybrid functionals applied to extended systems,” *Journal of Physics: Condensed Matter*, vol. 20, no. 6, p. 064201, 2008.
- [58] R. Brydson, H. Sauer, W. Engel, J. Thomass, E. Zeitler, N. Kosugi, and H. Kuroda, “Electron energy loss and X-ray absorption spectroscopy of rutile and anatase: a test of structural sensitivity,” *Journal of Physics: Condensed Matter*, vol. 1, no. 4, p. 797, 1989.
- [59] W. A. Harrison, “Theory of polar semiconductor surfaces,” *Journal of Vacuum Science and Technology*, vol. 16, no. 5, p. 1492, 1979.
- [60] M. Pashley, “Electron counting model and its application to island structures on molecular-beam epitaxy grown GaAs (001) and ZnSe (001),” *Physical Review B*, vol. 40, no. 15, p. 10481, 1989.
- [61] A. Kiejna, T. Pabisiak, and S. Gao, “The energetics and structure of rutile TiO_2 (110),” *Journal of Physics: Condensed Matter*, vol. 18, no. 17, p. 4207, 2006.
- [62] G. Charlton, P. Howes, C. Nicklin, P. Steadman, J. Taylor, C. Muryn, S. Harte, J. Mercer, R. McGrath, D. Norman, *et al.*, “Relaxation of TiO_2 (110)-(1 \times 1) using surface X-ray diffraction,” *Physical Review Letters*, vol. 78, no. 3, p. 495, 1997.
- [63] R. Lindsay, A. Wander, A. Ernst, B. Montanari, G. Thornton, and N. Harrison, “Revisiting the surface structure of TiO_2 (110): a quantitative low-energy electron diffraction study,” *Physical Review Letters*, vol. 94, no. 24, p. 246102, 2005.
- [64] E. Hendry, F. Wang, J. Shan, T. Heinz, and M. Bonn, “Electron transport in TiO_2 probed by THz time-domain spectroscopy,” *Physical Review B*, vol. 69, no. 8, pp. 081101–R, 2004.
- [65] P. Krüger, S. Bourgeois, B. Domenichini, H. Magnan, D. Chandesris, P. Le Fevre, A. Flank, J. Jupille, L. Floreano, A. Cossaro, *et al.*, “Defect states at the TiO_2 (110) surface probed by resonant photoelectron diffraction,” *Physical Review Letters*, vol. 100, no. 5, p. 055501, 2008.
- [66] A. Hagfeldt, G. Boschloo, L. Sun, L. Kloo, and H. Pettersson, “Dye-sensitized solar cells,” *Chemical Reviews*, vol. 110, no. 11, p. 6595, 2010.
- [67] S. G. Kumar and L. G. Devi, “Review on modified TiO_2 photocatalysis under UV/visible light: selected results and related mechanisms on interfacial charge

- carrier transfer dynamics,” *The Journal of Physical Chemistry A*, vol. 115, no. 46, p. 13211, 2011.
- [68] K. Szot, M. Rogala, W. Speier, Z. Klusek, A. Besmehn, and R. Waser, “TiO₂—a prototypical memristive material,” *Nanotechnology*, vol. 22, p. 254001, 2011.
- [69] E. Bertel, R. Stockbauer, and T. E. Madey, “Resonant electron emission in Ti and TiO₂,” *Physical Review B*, vol. 27, no. 3, p. 1939, 1983.
- [70] F. Zuo, L. Wang, T. Wu, Z. Zhang, D. Borchardt, and P. Feng, “Self-doped Ti³⁺ enhanced photocatalyst for hydrogen production under visible light,” *Journal of the American Chemical Society*, vol. 132, no. 34, p. 11856, 2010.
- [71] G. Lu, A. Linsebigler, and J. T. Yates, “Ti³⁺ defect sites on TiO₂ (110): Production and chemical detection of active sites,” *Journal of Chemistry*, vol. 98, p. 11733, 1994.
- [72] R. Schaub, P. Thostrup, N. Lopez, E. Lægsgaard, I. Stensgaard, J. Nørskov, and F. Besenbacher, “Oxygen vacancies as active sites for water dissociation on rutile TiO₂(110),” *Physical Review Letters*, vol. 87, no. 26, p. 266104, 2001.
- [73] P. Krüger, J. Jupille, S. Bourgeois, B. Domenichini, A. Verdini, L. Floreano, and A. Morgante, “Intrinsic nature of the excess electron distribution at the TiO₂ (110) surface,” *Physical Review Letters*, vol. 108, no. 12, p. 126803, 2012.
- [74] E. Shoko, M. F. Smith, and R. H. McKenzie, “Charge distribution near bulk oxygen vacancies in cerium oxides,” *Journal of Physics. Condensed Matter*, vol. 22, no. 22, p. 223201, 2010.
- [75] Z. Zhang, K. Cao, and J. T. Yates, “Defect-electron spreading on the TiO₂ (110) semiconductor surface by water adsorption,” *The Journal of Physical Chemistry Letters*, vol. 4, p. 674, 2013.
- [76] I. Leonov, a. N. Yaresko, V. N. Antonov, U. Schwingenschlögl, V. Eyert, and V. I. Anisimov, “Charge order and spin-singlet pair formation in Ti₄O₇,” *Journal of Physics: Condensed Matter*, vol. 18, no. 48, p. 10955, 2006.
- [77] M. Watanabe and W. Ueno, “Raman study of order-disorder transition of bipolarons in Ti₄O₇,” *Physica Status Solidi (C)*, vol. 3, no. 10, p. 3456, 2006.
- [78] V. Eyert, U. Schwingenschlögl, and U. Eckern, “Charge order, orbital order, and electron localization in the Magnéli phase Ti₄O₇,” *Chemical Physics Letters*, vol. 390, no. 1-3, p. 151, 2004.
- [79] M. Watanabe, W. Ueno, and T. Hayashi, “Optical study of metal-insulator transitions in Ti₄O₇ single crystals,” *Journal of Luminescence*, vol. 122-123,

- p. 393, 2007.
- [80] L. Liborio, G. Mallia, and N. Harrison, “Electronic structure of the Ti_4O_7 Magnéli phase,” *Physical Review B*, vol. 79, no. 24, p. 245133, 2009.
- [81] C. W. Castleton, A. Höglund, and S. Mirbt, “Managing the supercell approximation for charged defects in semiconductors: Finite-size scaling, charge correction factors, the band-gap problem, and the ab initio dielectric constant,” *Physical Review B*, vol. 73, no. 3, p. 035215, 2006.
- [82] H.-P. Komsa, T. T. Rantala, and A. Pasquarello, “Finite-size supercell correction schemes for charged defect calculations,” *Physical Review B*, vol. 86, no. 4, p. 045112, 2012.
- [83] C. G. Van de Walle and J. Neugebauer, “First-principles calculations for defects and impurities: applications to III-nitrides,” *Journal of Applied Physics*, vol. 95, no. 8, p. 3851, 2004.
- [84] F. Birch, “Finite elastic strain of cubic crystals,” *Physical Review*, vol. 71, p. 809, 1947.
- [85] R. L. Kurtz, R. Stock-Bauer, T. E. Msdey, E. Román, and J. De Segovia, “Synchrotron radiation studies of H_2O adsorption on $\text{TiO}_2(110)$,” *Surface Science*, vol. 218, no. 1, p. 178, 1989.
- [86] M. A. Henderson, W. S. Epling, C. L. Perkins, C. H. Peden, and U. Diebold, “Interaction of molecular oxygen with the vacuum-annealed $\text{TiO}_2(110)$ surface: molecular and dissociative channels,” *The Journal of Physical Chemistry B*, vol. 103, no. 25, p. 5328, 1999.
- [87] M. A. Henderson, W. S. Epling, C. H. Peden, and C. L. Perkins, “Insights into photoexcited electron scavenging processes on TiO_2 obtained from studies of the reaction of O_2 with OH groups adsorbed at electronic defects on $\text{TiO}_2(110)$,” *The Journal of Physical Chemistry B*, vol. 107, no. 2, p. 534, 2003.
- [88] W. S. Epling, C. H. Peden, M. A. Henderson, and U. Diebold, “Evidence for oxygen adatoms on $\text{TiO}_2(110)$ resulting from O_2 dissociation at vacancy sites,” *Surface Science*, vol. 412, p. 333, 1998.
- [89] N. G. Petrik, Z. Zhang, Y. Du, Z. Dohnálek, I. Lyubinetsky, and G. A. Kimmel, “Chemical reactivity of reduced $\text{TiO}_2(110)$: the dominant role of surface defects in oxygen chemisorption,” *The Journal of Physical Chemistry C*, vol. 113, no. 28, p. 12407, 2009.
- [90] Y. Du, N. A. Deskins, Z. Zhang, Z. Dohnalek, M. Dupuis, and I. Lyubinetsky,

-
- “Formation of o adatom pairs and charge transfer upon O_2 dissociation on reduced TiO_2 (110),” *Physical Chemistry Chemical Physics*, vol. 12, no. 24, p. 6337, 2010.
- [91] G. A. Kimmel and N. G. Petrik, “Tetraoxygen on reduced TiO_2 (110): oxygen adsorption and reactions with bridging oxygen vacancies,” *Physical Review Letters*, vol. 100, no. 19, p. 196102, 2008.
- [92] J. Tersoff and D. Hamann, “Theory and application for the scanning tunneling microscope,” *Physical Review Letters*, vol. 50, no. 25, p. 1998, 1983.
- [93] J. Tersoff and D. R. Hamann, “Theory of the scanning tunneling microscope,” *Physical Review B*, vol. 31, p. 805, Jan 1985.
- [94] S. Tan, Y. Ji, Y. Zhao, A. Zhao, B. Wang, J. Yang, and J. Hou, “Molecular oxygen adsorption behaviors on the rutile TiO_2 (110)- 1×1 surface: an in situ study with low-temperature scanning tunneling microscopy,” *Journal of the American Chemical Society*, vol. 133, no. 6, p. 2002, 2011.
- [95] E. Yagi, R. R. Hasiguti, and M. Aono, “Electronic conduction above 4 k of slightly reduced oxygen-deficient rutile TiO_{2-x} ,” *Physical Review B*, vol. 54, no. 11, p. 7945, 1996.
- [96] C. L. Pang, R. Lindsay, and G. Thornton, “Structure of clean and adsorbate-covered single-crystal rutile TiO_2 surfaces,” *Chemical Reviews*, vol. 113, no. 6, p. 3887, 2013.